96 pages

EXPERIMENTAL ANALYSES OF TRAILING EDGE FLOWS

S.L. Petrie
D.S. Emmer
Department of Aeronautical and Astronautical Engineering
The Ohio State University
Columbus, Ohio

Final Technical Report
to
NASA Ames Research Center

NASA Grant NSG - 2298

June, 1984

EXPERIMENTAL ANALYSES OF TRAILING EDGE FLOWS

S.L. Petrie
D.S. Emmer
Department of Aeronautical and Astronautical Engineering
The Ohio State University
Columbus, Ohio

Final Technical Report
to
NASA Ames Research Center

NASA Grant NSG - 2298

June, 1984

FOREWORD

This final technical report was prepared by S.L. Petrie and D.S. Emmer of the Aeronautical and Astronautical Research Laboratory (AARL) for The Ohio State University Research Foundation. The research reported here was performed under NASA Grant NSG-2298, RF project number 711001, and covers work undertaken over the period 1 February, 1978 to 1 January, 1981 at the AARL.

The work was conducted as part of the requirements leading to the PhD degree for D.S. Emmer, which were completed in June, 1984.

The program was under the direction of J.G. Marvin of the National Aeronautics and Space Administration, Ames Research Center, Moffett Field, California.

ABSTRACT

An experimental study of several of the trailing edge and wake turbulence properties for a NACA 64A010 airfoil section was completed. The experiment was conducted at The Ohio State University Aeronautical and Astronautical Research Laboratory in the 6 inch X 22 inch transonic wind tunnel facility. The data were obtained at a free stream Mach number of 0.80 and a flow Reynolds number (based on chord length) of 5 million. The principle diagnostic tool was a dual-component laser Doppler velocimeter.

The experimental data included surface static pressures, chordwise and vertical mean velocities, RMS turbulence intensities, local flow angles, and a determination of turbulence kinetic energy in the wake.

Two angles of attack (0 and 2 degrees) were investigated. At these incidence angles, four flow field surveys were obtained ranging in position from the surface of the airfoil, between the transonic shock and the trailing edge, to the far-wake. At both angles of attack, the turbulence intensities and turbulence kinetic energy were observed to decay in the streamwise direction. In the far wake, for the non-lifting case, the turbulence intensities were nearly isotropic. For the two degree case, the horizontal component of the turbulence intensity was observed to be substantially higher than the vertical component.

TABLE OF CONTENTS

LIST OF TABLES

LIST OF FIGURES

I. INTRODUCTION

There is general agreement among investigators that the fluctuations in the fluid properties of a turbulent flow are random in nature and that this randomness is, in fact, an intrinsic feature of turbulence. In theory, turbulence can be computed by predicting these fluctuations through formal mathematical analyses. In practice, while it is possible to program the time-dependent form of the Navier-Stokes equations for digital computation, application of the analysis to flow fields which include boundary-layer separation makes full solution of the equations currently impractical. Solution on a scale sufficient to resolve the smallest turbulent eddies requires such excessive memory size and long run times that solutions cannot be obtained with existing computers (Ref. 2) Therefore, time-averaged equations are employed and closure of the system requires modeling of the turbulence terms.

At present, turbulence modeling can be developed only with heavy reliance on experimental data. However, as modeling proceeds from simple algebraic eddy viscosity models to higher order closure schemes, more demands are placed on the experimental programs if they are to produce results that can guide the modeling. For example, surface pressure measurements allow an overall assessment of the accuracy of a specific turbulence model but do not provide sufficient detail to allow improvement to the model.

Ideally, both time-averaged and fluctuating fluid properties should be measured in a single experiment. Frequently, emphasis is placed on either the time-averaged or the fluctuating properties and complete documentation of the overall flow field or the extent of separation are not included. The various requirements for increased detail in the experimental measurements as higher order modeling techniques have been outlined by Marvin (Ref. 3).

Numerous studies have been conducted which provide data for both airfoils and axisymmetric geometries. Results of some of the more recent studies are summarized in References 4 - 6. There is, however, a paucity of data for trailing edge flows both with trailing edge and shock-induced separation. This is especially true at transonic Mach numbers.

The purpose of this research effort was to determine some of the fundamental turbulence properties associated with trailing edge flows. Obtaining data pertinent to the development and verification of turbulence modeling techniques was of primary

interest. Emphasis was placed on obtaining mean and fluctuating (RMS) velocity measurements in the near and far wake regions of a two-dimensional airfoil. Both normal and parallel components of velocity were investigated. A two-component laser Doppler anemometer operating in the forward scatter mode was employed for the measurements.

Comparisons of the experimental data with the results of certain theoretical analyses were made. The theoretical methods include, for example, the method of Garabedian and Korn (Ref. 7) for the external pressure distributions. For the velocity and flow angle data, further comparisons with the theory and experimental data from other test facilities were included wherever possible.

The experimental data and comparisons with the theoretical results should provide data for transonic flows with shock-induced and trailing edge separation useful in extending the turbulence models currently in use.

II. EXPERIMENTAL APPARATUS AND PROCEDURES

A. Wind Tunnel Configuration and Evaluation

The experiments were conducted in the 6 inch x 22 inch transonic wind tunnel facility at The Ohio State University Aeronautical and Astronautical Research Laboratory (AARL). The facility is illustrated in Figures 1 and 2. It is an unique, isolated-plenum, blow down wind tunnel especially suited for testing two-dimensional airfoils. The test section dimensions are 6 inches wide x 22 inches high x 44 inches long. The test section side walls are parallel and are constructed of 1-inch thick solid aluminum plate. The upper and lower walls are 10% open perforated aluminum plate overlying individual plenums. Each plenum is aspirated into a mixing zone upstream of the diffuser. The isolated plenum configuration permits the plenum cavities to respond individually to pressure changes caused by the model, leading to very low interference over a wide range of operating conditions and model attitudes.

The wind tunnel nozzle consists of two solid aluminum blocks machined to coordinates specifying continuous first and second derivatives vanishing at the nozzle exit. A pressure drop device and a two-stage bellmouth within the screened settling chamber are employed to maximize flow uniformity.

Test section Mach number is fixed by a choke consisting of an array of bars across the flow downstream from the induction section. The Mach number can be varied by changing the number and/or the diameter of the bars. The Reynolds number can also be controlled by changing the total pressure in the stagnation chamber. The capability of independently varying the Mach number and the Reynolds number is an essential feature in the study of Mach number and Reynolds number effects on two-dimensional airfoils. The overall operating envelope for this facility is shown in Figure 3.

The wind tunnel is regulated by presetting the control valve (Figure 1) to achieve the desired reservoir pressure. When the plug valve is opened, the circuit pressurizes within several seconds. Thereafter, the pressure drops in proportion to the mass flow from the storage tanks. The storage system provides 1500 cubic feet of air at pressures up to 2600 psia. Conventional air driers and filters are used to maintain gas purity. For the present series of tests, stagnation pressures were held at 30 psia.

Figure 4 shows a typical pressure history for this facility. Data were taken immediately after the pressure peak when a period

of nearly constant pressure was available. For the conditions shown in Figure 4, tunnel shutdown was delayed for the purpose of evaluating the response of the overall system. Good uniformity of pressure ratio is evident for the model taps until tunnel shutdown.

Prior to the experimental turbulence investigations, extensive testing was conducted to examine the flow quality, interference effects, and the degree of unsteadiness in the 6 x 22 tunnel. The detailed procedural techniques and results of these tests (not including the unsteady effects) were reported by Lee and Gregorek (Ref. 8). In summary, the results indicated excellent streamwise uniformity, a high degree of two-dimensionality, and negligible interference from the confining walls (the perforated plates) over the range of Mach numbers available (0.30 to 1.10). The lack of interference was attributed to the separation of the upper and lower surface plenums.

Inasmuch as this experimental investigation was directed,in part, toward the measurement of turbulent flow properties, a knowledge of the unsteady characteristics of the wind tunnel facility was of vital importance. Useful data for these quantities can be obtained from a wind tunnel only if the free stream dynamic environment is quiet enough or if the characteristics of the fluctuations are known such that corrections can be made. Significant free stream unsteadiness can have serious effects on the onset of flow oscillations, as reviewed in References 4, 4, and 9. The failure of the Kutta condition associated with flow oscillations, as discussed in Reference 8, may also be coupled to the degree of unsteadiness.

The source of pressure oscillations depends strongly on the specific wind tunnel configuration and flow Mach number. Oscillations may be due to combinations of fluctuations accompanying turbulent boundary layers on the tunnel walls, traveling waves from the tunnel control valves, free stream turbulence, acoustical harmonics from wall perforations, or resonance in the plenums.

Recent tests made by Davis (Ref. 10), in the OSU 6 x 22 transonic facility, employed high-response pressure transducers (Kulites) mounted in the surface of an oscillating NACA 64A010 airfoil section. In addition to the analysis of the unsteady flow field in the vicinity of the airfoil, the tests were directed toward establishing the degree of flow unsteadiness present throughout the tunnel over its entire operating range. High-response transducers mounted in the tunnel walls, in pitot and static pressure probes, and in the surface of a 10 degree sharp cone were also employed. Although the cone is a poor configuration for testing in a two-dimensional airfoil tunnel, data were

available for comparisons from more than eighteen wind tunnels in the United States and Europe (Ref. 11).

The tunnel-empty data for the OSU tunnel are compared with results from several other wind tunnels in Figure 5. The tunnel noise below Mach 0.50 was judged to be excessive and could cloud interpretation of certain time-resolved measurements. The wind tunnel configuration has since been altered to reduce the pressure fluctuations by installing extensive honeycomb and flow straightening devices in the tunnel reservoir region. This has resulted in a significant reduction in the magnitude of the pressure oscillations in the test section. However, the present data were obtained prior to these modifications

The present investigations were conducted at a test section Mach number of 0.80, where serious complications due to noise-generated unsteadiness were avoided.

B. Model Configuration

A NACA 64A010 airfoil section was selected for use in the present study because of its simple geometry and the availability of a large data base. Hence, comparisons of results with theoretical predictions and other experimental data were facilitated.

The model had a 6-inch chord length and was fabricated from solid brass on a computer-controlled milling machine using a minimum of 600 coordinate sets. A total of 36 pressure taps were incorporated into the upper and lower surfaces by "blind drilling". This assured that the exterior of the model was not marred by inlaying tubes. The terminal tubes were epoxied into the side of the model. This overall arrangement permitted easy changes in angle of attack, efficient coupling and de-coupling of the pressure-sensing apparatus, and positive optical access for LDV measurements.

The model, shown in Figure 6, was held between two, flush-mounted, 9-inch diameter, polished plexiglass windows. The circular window geometry permitted accurate positioning of incidence angle. The 1-inch thick, optical-quality plexiglass provided the necessary structural support, a sufficiently high transparency to the laser beam radiation, and good optical access to regions near the airfoil surface and trailing edge. Due to the orientation of the receiving optics, however, laser flare from the model surface presented difficulties at several data points near the model surface.

C. LDV Optical Assembly

The principle diagnostic tool was a dual beam, two component, real-fringe LDV operating in the forward scatter mode. Incident radiation was provided by a Spectra Physics model 164/09, 5 watt, Argon-ion laser. Chordwise (u) and vertical (v) velocities were measured using the 514.5 nm and the 488.0 nm lines, respectively. The 488.0 nm line was Bragg-cell shifted to eliminate directional ambiguity in the velocity.

The transmitting optical arrangement is illustrated schematically in Figure 7. The output beam was initially passed through a polarization rotator that rotated the normally vertical polarization vector into the horizontal plane. This rotation was necessary to minimize power losses associated with the horizontal dispersion of the component wavelengths by the prism.

Prior to dispersion, the laser beam was collimated to reduce the effects of beam divergence and assure that the beam crossing point and the waist of the focused laser beams were coincident. Collimating the beam also increased the fringe contrast and signal-to-noise ratio of the overall system. The collimated beam was separated into its individual wavelengths where all but the 514.5 nm and the 488.0 nm lines were masked out of the system. Each beam was then reflected off of a series of steering mirrors and was passed through a 15 mm diameter, 1/2 waveplate before split into the individual wavelengths.

The capability of frequency shifting with Bragg cells was designed into both the 514.5 nm and 488.0 nm lines. However, it was necessary to shift only in the blue (488.0) since this was the only component in which flow reversals were expected. The 40 Mhz carrier frequency of the Bragg cell electronics was electronically downmixed to an effective value of 10 Mhz, which proved to be most suitable for processing data in the speed range of these studies.

Final focusing of the four beams was accomplished with an achromatic doublet with a minimum clear aperture diameter of 152 mm and a focal length of 1524 mm (60 inches).

In order to minimize movement and realignment of the entire transmitting optical assembly, a system of four motorized, computer-controlled mirrors was employed to position the probe volume. With this arrangement, positioning was attainable to within a tolerance of + or - .004 inches in both the chordwise and vertical directions.

The overall positioning range of the probe volume was limited to + or - 1.00 inch from the initial test point in both scanning directions. Therefore, for a given optical location,

data could be obtained at any point within a 2 inch square data window. Data points desired outside these limits required the repositioning of the optical assembly in order to establish a new data window. The assembled LDV transmitting optical package is pictured in Figure 8.

The receiving optics package is shown schematically in Figure 9. In an effort to reduce the effects of extraneous noise sources that might influence the data and to separate the two velocity components, the individual light wavelengths were filtered before being directed into the photomultipliers.

EMI 9812B photomultiplier tubes were selected for use in both channels of the LDV system. The tubes had a diameter of 51 mm and were fast linear focused, end-window types with S-11 spectral response.

The receiving optics were designed to provide maximum adjustability. Each assembly had several degrees of freedom and could be independently positioned vertically, horizontally, and in rotation.

The receiving optics package is pictured in Figure 10. The counter weights and pulley assemblies on either side of the support table were installed to prevent electrical overload in the positioning motors.

D. Seeding Technique

Due to inadequate numbers of naturally occurring scattering centers in the flow field, a series of tests was conducted to determine a suitable seeding material and a method of introducing the material into the flow.

Since the primary function of the seed particles was to provide a source of Doppler-shifted scattered light characteristic of the flow velocity, it was essential that the seed particles meet the following requirements: (1) the particles must follow the flow; (2) the particle diameter and refractive index must be large enough to scatter sufficient quantities of light to provide useful LDV signals; and (3) the concentration of the seed particles in the flow field must be high enough to yield an acceptable data rate.

Requirements (1) and (2) are contradictory. That is, in general, a particle's ability to scatter light decreases with decreasing diameter but small particles follow the flow more reliably than large ones. It was therefore necessary to select a

seeding material that was a compromise between particle response to flow oscillations and light-scattering characteristics.

Polystyrene latex (PSL), with an index of refraction of 1.62 and a nominal diameter of 0.5 microns was selected as the seeding material. An electron micrograph of the particles (Ref. 12), shown at a magnification of 25,000 is given in Figure 11. Note that the particles are well formed with a high degree of dimensional uniformity.

To ensure good, overall distribution and uniformity in the flow field, the PSL was injected directly into the high pressure wind tunnel supply line upstream of the reservoir. The injection system was computer-controlled and was set to open or close a high pressure solenoid valve at preselected times during a wind tunnel run. A schematic of the injection system is shown in Figure 12.

Prior to injection, the PSL was mixed with methanol in a ratio of 1:20,000 by volume. This was the equivalent of placing three drops of polystyrene into two liters of methanol. Higher concentrations of polystyrene had a tendency to coat the flow-straightening screens in the wind tunnel reservoir.

The PSL-methanol mixture was placed in a high pressure, stainless steel bottle and the bottle was pressurized to 500 pounds per square inch with dry Nitrogen. After injection, the methanol carrier evaporated before reaching the test section thus leaving only the PSL particles. The concentration of PSL particles in the flow field was controlled by manually opening or closing the needle valve shown in Figure 12. The particle injection system is pictured in Figure 13.

To minimize the health hazard to operating personnel and to keep airborne polystyrene particles from contaminating the outside environment, the wind tunnel discharge was passed through a high pressure water bath which removed the particles as a precipitate.

E. Data Acquisition System

The light-sensing electronic subsystem included high gain, wideband amplifiers for the 488.0 nm and 514.5 nm wavelength light signals and a computer controlled signal multiplexer. Each amplifier operated within a frequency range of 0-400 Mhz at a rated fixed gain of 40 and were powered at a regulated +12VDC.

Only one LDV signal processor was available for these studies. Hence, the outputs from both photomultipliers were

connected to a multiplexer, which allowed selection of the particular signal sent to the processor. The multiplexer was controlled by the data acquisition computer program.

Limits on velocity data acquisition for a given point were established by preselecting both a maximum time on station and a specified number of data samples per point. When either 2000 samples were collected or the maximum time on station was exceeded for a given velocity component at a particular location in the flow field, the signal multiplexer was commanded to select the remaining velocity component and the process was repeated.

If the time-on-station limit was reached before 2000 samples were acquired, the wind tunnel run was generally terminated by the operator to conserve the air supply. Since the number of repeated data acquisition sequences per station was also a preselected variable, the multiplexer provided the capability of obtaining multiple data points in a given wind tunnel run.

The pressure-sensing subsystem included a Statham pressure transducer with a full scale range of 50 pounds per square inch in combination with two cut-off valves and a Scanivalve for measuring both facility and model static pressures. During the data acquisition phase of a tunnel run, the cut-off valves retained the static pressure values for each pressure tap. During the data reduction phase, the Scanivalve rotated and sampled the pressures in each port of the cut-off. Prior to evaluation of pressure coefficient, the raw pressure data were corrected for the small but finite volume of air trapped in the cavities of the Scanivalve. This correction typically ranged over values from 0.2% to 0.4% of the initial raw pressure readings. A compressibility correction employing the conventional Prandtl-Glauert rule was also applied to the data for reference purposes. Both of the latter corrections were incorporated into the computer software and were included as part of the final data reduction.

F. Statistical Analysis and Data Reduction

Statistical analysis and signal processing were performed on a maximum of 2000 realizations per test point. Data reduction for the u velocity component was accomplished using the weighted-reciprocal technique recommended by McLaughlin and Tiedermann (Ref. 13). This method corrects for velocity biasing which occurs due to the passage of particles through the probe volume which have velocities different from the average value. For example, the probability of measuring a faster-than-average particle is greater since a larger number of these particles can pass through the probe volume during the measuring period. Since the fringes were not rotated relative to the free stream flow and since the

particle residence time in the probe volume for the Bragg-shifted v-component measurement was clearly dominated by the u-component velocity, no fringe biasing corrections were applied to the v-component.

Data analysis for each velocity component consisted of calculating the mean velocity, the root-mean-square turbulence intensity, turbulence kinetic energy (TKE), and the local flow angle. Velocity histograms were also included to aid in the interpretation of the data.

The turbulence kinetic energy per unit mass was determined by assuming that $\langle v' \rangle = \langle w' \rangle$.

The experimental raw data were edited to remove wild points. The method of editing involved the truncation of all raw data more than three standard deviations above and below the calculated mean value. Once the editing was applied, new values for mean velocity and turbulence intensity were re-computed from the remaining data.

In general, this process had a negligible effect on the mean values. However, if there were several numerically very large or very low velocities included in the original data set outside the 3-sigma boundaries, the editing procedure had a dramatic effect on the turbulence intensity value. In using the editing technique, data that otherwise would have had to have been excluded from the surveys could be retained.

G. Processor and Frequency-Shifting Criteria

The signal processor was a single-particle burst counter type and required a minimum of thirteen cycles per Doppler burst before validating data. Once an unattenuated, 50 mv threshold signal level was reached (after high-pass filtering), validation was based on a preselected 5 percent cycle time comparison between five and eight output pulses of the Schmitt trigger, where each pulse corresponded to a zero crossing of the filtered signal. If the data were accepted, a "data ready" signal was passed to the on-line computer for data reduction and storage in memory. If the data were rejected, the processor was automatically reset and the procedure was repeated. Accepted data were first stored in a disc file for on-line data analysis and were then written to magnetic tape for subsequent off-line data reduction and archival storage.

A high limit (low-pass) filter and a low limit (high-pass) filter network, incorporated into the processor circuitry, served

to simultaneously eliminate extraneous high-frequency noise and the low-frequency pedestal from both the u and v signals.

For the u-component, the fringes were not Bragg shifted since flow reversals were not expected. Estimating the mean velocity at 244 m/sec (800 ft/sec) with a fringe spacing of 16 microns gave an expected, unshifted Doppler frequency of 15.2 Mhz. Based on this frequency, the low-pass filter setting was set at 30Mhz. The high-pass filter was set at 1 Mhz to remove the pedestal voltage.

In the case of the v-component, where flow reversals were likely to occur, similar consideration was given regarding optimum filter adjustments. Moreover, when the turbulence levels were low, frequency shifting was required to provide an adequate number of Doppler cycles for the processor to operate. Since the shift frequency and the u-component Doppler frequency were arranged to be of comparable magnitudes, the low-pass and high-pass filters on the processor were set at the same values for both u and v velocity measurements. This arrangement of filter settings allowed multiplexing of the signals from the two data channels into the signal processor as described above.

H. LDV Operating Characteristics

Several of the principle operating characteristics of the LDV used in this study are given in Table 1. In addition, evaluations of the signal-to-noise ratio, SNR, and the light scattering qualities of the system were conducted employing the LDV simulation code developed by Meyers (Ref. 14).

Laser Power	= 0.8 Watts
Bandwidth	= 30 Mhz
Scattered Light Coef	= 25
Laser Wavelength	= 500 nm
Mie Scattering Parameter	= 4.58
Collecting Lens Diameter	= 80 mm
Probe Volume Image Distance	= 300 mm
Transmitting lens Focal Length	= 1524 mm
Laser Beam Diameter	= 1.25 mm
Visibility	= 0.90
Particle Diameter	= 0.75 micron

Table 1. LDV Operating Characteristics

The output from the simulation code, in the form of variations in the values of signal-to-noise ratio over the surface of the collecting lens, is shown in Figure 14. Note that the lowest value calculated for the signal to noise was approximately 33. In

addition, predictions from the code for the raw signal and band-pass filtered signal are given in Figures 15 and 16. These indicate that the magnitude of the signals were more than adequate to satisfy the processor requirements.

The effective signal-to-noise ratio of the final operating system did not exhibit the high predicted values. The discrepancy was attributed to the large quantities of scattered light which were generated by the laser penetration of the access windows. While the d.c. components of these signals were removed by the high-pass filters in the LDV processor, the corresponding "shot noise" generated by the high d.c. light levels appeared as a source of high frequency white noise. This abnormally high shot noise was responsible for the observed reduction in the signal-to-noise ratio. Despite this, however, the signal-to-noise ratio was still of a level sufficient to provide good data rates and reliable velocity information. During tunnel operation, for example, typical signal levels at the processor were of the order of one-half volt, peak to peak, with corresponding signal-to-noise ratios on the order of 14.

III. EXPERIMENTAL RESULTS AND DISCUSSIONS

A. Surface Pressures

The pressure distributions for model angles of attack of 0, 2, and 4 degrees are shown in Figures 17, 18 and 19. At the 0 and 2 degree angles, the data agree well with the theoretical predictions of the Garabedian and Korn code. The transonic shock is quite weak at 0 angle of attack and its position on the airfoil is well predicted by the theory. The theoretical results at the trailing edge predict a greater pressure recovery than is observed in the experiment. This behavior near the trailing edge is typical of the results obtained from the Garabedian and Korn code.

For the 2 degree case of Figure 18, the theoretical pressures agree well with the data except very near the shock wave. The theory predicts the correct values for the pressures but places the shock wave too far forward on the airfoil. This is probably due to the fact that the theory does not include the effects of the surface boundary layer and its modification of the effective airfoil contour.

The pressure data at 4 degrees angle of attack shown in Figure 19 indicate that the airfoil stalls at this condition. However, since the angle of attack is relatively low, the degradation in performance at this condition is likely due to a breakdown in the wind tunnel flow field. To substantiate this and to evaluate the overall performance of the model-wind tunnel system, a series of tests employing oil flow visualization was conducted. Typical photographs for the three angle of attack cases are shown in Figures 20- 22.

For the non-lifting case of Figure 20, the transonic shock is sufficiently weak that it is not evident in the oil flow pattern. Instead, the location of transition of the boundary layer is clearly evident near the 20% chord location. Transition bursts initiated at the pressure orifices can also be observed in the photograph.

For the 2 degree angle of attack case of Figure 21, the shock wave is clearly evident in the oil pattern. The location of the shock wave agrees well with that obtained from the pressure distributions. The flow over the surface of the model is observed to be two-dimensional at these flow conditions.

The reasons for the discrepancies between the predicted and measured pressures at the 4 degree angle of attack condition are clearly evident in Figure 22. In this case, the transonic shock

wave on the model surface is of sufficient strength that it interacts with the tunnel side wall boundary layer, causing local separation on the side wall. This significantly disturbs the model flow field, causing massive separation over the latter half of the model. Hence, no additional data for the 4 degree angle of attack case is available.

B. Mean Velocity Data

Chordwise and normal velocity data were obtained at the locations shown in Figure 23. In addition to the near and far-field wake surveys, an examination of the flow field between the upper surface transonic shock and the trailing edge was conducted.

The vertical reference for data upstream of the trailing edge is taken to be the surface of the airfoil. For data in the wake at 0 degrees angle of attack, the reference is taken to be the trailing edge location. For data in the wake at angles of attack, the reference is taken to be the trailing edge location measured horizontally (parallel to the free stream). For easy comparisons, corrections to the trailing edge location measured in the airfoil coordinate system (coincident with the chord line) are indicated by an asterisk (*) on the individual data plots.

The upper surface mean velocity distributions for both the zero and 2 degree cases are shown in Figures 24-27. The u-component distribution at zero angle of attack shows negligible effects due to the presence of the shock wave, no separation, and a normal velocity profile within the boundary layer. This is consistent with a weak shock wave and a small adverse pressure gradient.

In Figure 24, the distribution is shown compared to the 1/7 power law given by:

$$u/U = (y/)^{1/7} \qquad (1)$$

The velocity profile for the 2 degree angle of attack shown in Figure 25 is almost identical to that for the non-lifting case, except for the data point at y/c of 0.02. The angle of attack case displays a slightly higher velocity at this location. However, the differences in the two profiles are slight, so that little difference in the boundary layer is observed for these two flow conditions.

The v velocity distributions for the surface boundary layer profiles are shown in Figures 26 and 27. For the zero angle of attack case, the vertical velocities are nearly constant throughout the extent of the flow field investigated. However, for the 2 degree case of Figure 27, the vertical velocity increases in magnitude as the surface of the airfoil is approached. In addition, the velocity displays a more negative value, consistent with the angle of attack of the model.

It should be noted that the velocity data points at different vertical stations in the flow field were obtained from separate wind tunnel runs. occasionally, repeat data at a given vertical station were also obtained from different runs. Hence, the data indicate a high degree of repeatability in the data acquisition/reduction procedures.

Data obtained at a location 0.23 inch (x/c = 1.04) downstream of the trailing edge are shown in Figures 28 and 29. The velocity profile for the zero angle of attack case of Figure 28 is nearly identical to that obtained on the airfoil surface, except on the wake centerline. Note that data on the airfoil surface could not be obtained closer than y/c = .01. At y locations greater than this value, the near-wake and surface u velocity profiles are identical. This indicates that the wake is dominated by the boundary layer properties just downstream of the trailing edge.

The velocity profile data are compared with the results of Johnson and Bachalo (Ref. 15) and with the results from numerical analysis employing turbulence modelling reported in Ref. 15. The two experimental profiles agree well except very near the wake centerline where the data of Ref. 15 give a much lower centerline velocity. However, the data of Ref. 15 were obtained slightly closer to the trailing edge where it would be expected that the centerline value would be lower. The numerical results of Ref. 15 do not give accurate predictions for the velocity profile, except near the wake centerline.

For the 2 degree data of Figure 29, the wake shows a significant increase in thickness over that of the zero angle of attack case. While the surface velocity profiles are nearly identical, the near-wake definitely shows the effects of the higher angle of attack and stronger shock wave.

Mean velocity data from the wake survey taken at a position 1 inch downstream of the trailing edge are given in Figures 30 - 33. In comparing the data of Figure 30 with those of Figure 28, it can be seen that the central portion of the wake is wider at the downstream station, while the velocity at the trailing edge location is slightly higher, indicating a gradual trend toward equilibrium. In Figure 31, the v-component velocity distribution

clearly indicates a sign change just below the trailing edge, representative of an upward flow component from the lower surface of the airfoil. It can be noted that the flow velocity does not quite pass through zero at the trailing edge. This may be due to a minor error in the true angle of attack. Overall, however, the velocity distribution shows good symmetry, indicative of a converging near-wake flow for an uncambered, non-lifting airfoil.

In Figure 32, the asymmetry and an upward shift in the wake is apparent with the minimum velocity point situated slightly above the trailing edge location. In the case of the u-component, this upward displacement of the wake was also observed by Johnson and Bachalo (Ref. 15) although, in their work, the angle of attack was higher and the upper surface flow field was highly separated. The v-component velocities of Figure 33 show the tendency for the velocity distribution to be displaced with the point of minimum velocity matching that of the u-component.

It can be noted in Figure 33 that at angle of attack, the v velocity is negative throughout the region of the flow field investigated. This is consistent with a positive angle of attack and indicates that the flow leaves the trailing edge smoothly, with no significant separation being evident.

The far-wake mean velocity data are shown in Figures 34 - 37. For the non-lifting case, Figure 34 demonstrates that the wake nearly totally recovers from the influences of the model, although the maximum value of the velocity is only 90% of the free stream value. This is may be due to the fact that the wake diverges to such an extent that none of the data points are outside the wake boundaries. In addition, at this downstream location, the flow variables likely were different from those in the model free stream due to minor variations in the tunnel flow characteristics.

Although there is some scatter in the data, when compared to the data in Figure 31, the trend in Figure 35 shows that the v-component velocities experience a complete reversal in direction (but not magnitude) at the trailing edge location. Data points above the trailing edge exhibit a positive, upward component while those points below the trailing edge location indicate negative, downward velocities. Similar to the previous data, the sign change is observed to occur very close to the trailing edge location. The velocity fluctuations in the data taken above the trailing edge were higher than those obtained below the trailing edge, possibly due to tunnel unsteadiness.

For the 2 degree case, Figure 36 indicates a downward wake displacement with the minimum velocity point corresponding to the trailing edge location in the airfoil coordinate system. For this angle of attack, the previous data of Figure 39 show an opposite,

upward displacement. This is likely due to the moderate adverse pressure gradient existing on the upper surface, resulting from the transonic shock. The velocity on the upper, aft portion of the airfoil is retarded relative to the flow on the lower surface with the resulting velocity difference extending into the near-wake. In the far-wake, however, the wake has sufficient time to reach equilibrium.

To display the development of the mean velocity flow field from the trailing edge to the far wake locations, the u and v velocity components are shown sequentially in Figures 38 - 41.

C. Local Flow Angles

Using the corresponding u and v values at each station, the local flow angles were calculated. The results for the non-lifting case are shown in Figures 42 - 44. In Figure 42, the flow angles are observed to be nearly constant over the vertical range of the survey and can be seen to conform uniformly to the negative slope of the upper surface. As can be seen in Figure 43, downstream of the trailing edge, the flow angle is reduced by almost 50% compared to value on the airfoil surface. The effect of the airfoil's lower surface flow can be seen by the change in the sign of the flow angle at the trailing edge location.

In the far wake, as seen in Figure 44, the flow angle reverses. While the flow angle in the region of the trailing edge is nearly zero, the wake diverges at a total included angle of approximately 5 degrees. Furthermore, the scatter in the data at this station is greater than that observed at the other stations. This appears to be a direct result of the flow field instabilities discussed above.

The corresponding flow angle surveys for the 2 degree case are shown in Figures 45 - 47. Figure 45 illustrates a considerable inconsistency in flow angles about the value of the surface slope, although both very near and far from the surface, the flow angle approaches the surface slope and shows good, overall repeatability. Slightly above the surface, the flow angles appear to respond to the straightening effects of the transonic shock wave.

In contrast to the zero angle of attack data, the data of Figure 46 show that the velocity from the lower surface of the airfoil has a negative, downward direction. With the exception of the trailing edge location, the overall flow direction in the wake is nearly constant with no evidence of convergence.

The far-wake data, shown in Figure 47, indicate an asymmetric divergence with the flow angles above the trailing edge displaying nearly constant values. Below the trailing edge, the flow angles increase continuously toward larger, negative values and appear to approach the -5 degree value of the near-wake data.

A cross plot of the flow angle data was constructed to observe the behavior of the local flow angle as a function of streamwise location. The results are shown in Figures 48 and 49 for the 0 and 2 degree angle of attack cases, respectively.

For the non-lifting case of Figure 48, the present data are compared to the Johnson and Bachalo data of Ref 15 obtained in the Ames 2 foot x 2 foot transonic facility. It can be seen that, with the exception of data taken at the trailing edge locations, all of the flow angle data of this study vary little from an approximate value of one degree. Compared to the data of Reference 15, the trend of the current data is the same, although the present data show consistently higher flow angles.

The disagreements between the data sets can be attributed to several distinctive differences. The Ames data were obtained at a lower Reynolds number, boundary layer trips were employed, and the data were obtained at a vertical station further from the model. The much wider variations in the Ames data at the 83% chord location for the 2 degree case are likely due the stronger shock-wave/boundary-layer interaction accompanying the upper surface shock wave.

The changes in the flow angles for both the lifting and non-lifting cases are summarized in Figures 50 and 51. In both sets of data, the convergence of the near wake at the trailing edge is followed by a divergence of approximately 6 degrees at the far wake location.

D. Velocity Histograms

Histograms were obtained for every velocity measurement. Representative plots are given in Figures 52 -54.

Although histograms generally provide limited numerical information concerning the turbulence flow properties, they often offer considerable insight into the character of the raw data. For example, a highly peaked, narrow-banded histogram, such as that of Figure 52, normally indicates that the velocity data were obtained over a narrow range of velocities with little turbulence. A broad or highly skewed histogram, such as that of Figure 54, however, indicates the presence of high turbulence levels.

E. Turbulence Intensities

The turbulence intensity profiles at each streamwise station in both the chordwise and vertical directions are shown for the non-lifting case in Figures 55 - 57. At the upper surface location of Figure 55, the u- velocity fluctuations are greatest near the wall with values of about 13% of the free stream steady state velocity. Data are not available for points nearer to the surface, but would be expected to decrease dramatically in this region, as indicated by the dotted lines. The vertical fluctuations, although consistently smaller in magnitude than the horizontal fluctuations, reflect a similar trend and are observed to decay rapidly to values of approximately 1% at the maximum vertical distance above the wall.

The near-wake data is given in Figure 56 where it can be seen that both the chordwise and vertical fluctuations have maximum values in the wake at about the same vertical location and that the fluctuations decrease in magnitude near the wake centerline. At the trailing edge location, the fluctuations are nearly isotropic with a value of about 2% of the free stream steady state value.

In the far-wake data of Figure 57, the fluctuations decrease in magnitude throughout the region surveyed, with the maximum fluctuations occurring in the central portion of the wake. Additionally, the difference between the maximum and minimum turbulence intensity levels is seen to be only 2% so that, while the profiles have been displayed separately for easier comparison, the chordwise and vertical fluctuations were nearly isotropic and could be well represented by a single curve.

The turbulence intensities for the 2 degree case are shown in Figures 58 - 60. The chordwise and vertical fluctuation levels at all streamwise stations are greater than the corresponding values at zero angle of attack. For the upper surface data shown in Figure 58, the y/c value for the point of maximum chordwise fluctuation was nearly 40% greater than the corresponding value for the zero degree angle of attack case.

Greater differences between the chordwise and vertical fluctuations are observed in the lifting configuration, with the maximum fluctuations in both directions occurring slightly further from the wall than they do in the zero angle of attack case. At its maximum, for example, the data in Figure 58 show that the chordwise fluctuation level is twice the value of the normal component. Near the wall, the fluctuations appear to approach zero, while at the maximum distance above the surface, the u and v velocity fluctuations have nearly the same value. However, they are larger than they are in the non-lifting case.

In the near-wake for the angle of attack case shown in Figure 59, the turbulence intensity profiles display a high degree of asymmetry about the trailing edge location. Above the trailing edge for example, the differences in the fluctuation levels are nearly three times greater at the peak maximums than they are below the trailing edge.

The data for the maximum downstream location shown in Figure 60 display smaller differences between the chordwise and vertical fluctuations across the trailing edge location than is observed in the near-wake data. Compared to the far-wake data at zero angle of attack (Figure 57), the fluctuations are not observed to be isotropic, although the vertical fluctuation levels are nearly unchanged by the angle of attack. Furthermore, the point of maximum chordwise fluctuation occurs at the trailing edge location and has a value of approximately 4% of the free stream velocity, which is 1.5 times larger than that for the non-lifting case.

Summary plots of the turbulence intensities for the 0 and 2 degree angle of attack surveys are shown in Figures 61 and 62.

F. Turbulence Kinetic Energy

The turbulence kinetic energy (TKE) was evaluated in the streamwise direction at all the vertical stations. The results, shown in Figure 63, represent the peak values obtained at each chordwise station for each angle of attack. In each case, the turbulence kinetic energy is observed to decay in the streamwise direction. In addition, the rates of decay for both cases are nearly the same from the surface location to the first station in the wake. However, the relative magnitudes of the TKE are consistently greater, by almost a factor of 2, for the angle of attack case.

In comparing the data obtained from the near and far-wake locations, the decay rate is nearly twice as great for the lifting case. The turbulence kinetic energies at the far-wake locations, however, were almost the same for both angles of attack.

IV. CONCLUSION

Experimental and theoretical studies of several of the trailing edge and wake turbulence properties for a NACA 64A010 airfoil section were conducted. The data were obtained at a transonic Mach number employing a state-of-the-art dual-component laser Doppler velocimeter as the primary diagnostic tool. Particular emphasis was placed on obtaining measurements of mean velocity, turbulence intensity, and local flow angle. In each instance, values for the longitudinal and transverse components were obtained for a lifting and a non-lifting case.

In view of the unavailability of experimental data of this kind, perhaps the most significant results of this investigation are the data presented for the near and far-wake regions of the flow field. It has been shown by Escudier (Ref. 16), for example,that the mixing length close to the outer edge of the boundary-layer is nearly constant. This model has been previously demonstrated to be reasonably accurate in the vicinity of the trailing edge. In the near-wake, however, the mixing length, scaled to boundary-layer thickness was observed to increase (Ref. 16). For the present data, the continued divergence of the wake at the far-field locations suggests a further increase in mixing length for both the 0 and 2 degree angle of attack cases.

For both angles of attack, the turbulence intensities and turbulence kinetic energies were observed to decay in the streamwise direction. In the far-wake, while the fluctuating components were seen to be nearly isotropic for the non-lifting case, the horizontal fluctuations above the trailing edge location for the 2 degree case were substantially higher than the transverse component. The turbulence kinetic energy, on the other hand, was nearly the same for both angles of attack at the maximum downstream location.

REFERENCES

1. Emmer, D. S., "Experimental Studies of Transonic Airfoil Trailing Edge and Wake Flowfield Properties", Ph.D Dissertation, The Ohio State University (1984)

2. Rubesin, M. W., Crisalli, A. J.,Horstman, C. C., and Acharya, M., "A Critique of Some Recent Second Order Closure Models for Compressible Boundary Layers", AIAA Paper No. 77-128, Los Angeles,California (1977).

3. Marvin, J. G., "Turbulence Modeling for Compressible Flows", NASA TM X-73, 188 (1977).

4. Seegmiller, H. L., Marvin, J.G., and Levy, L. L., "Steady and Unsteady Transonic Flow", AIAA Paper No. 78-160, Huntsville, Alabama (1978).

5. McDevitt, J. B., Levy, L. L., Deiwert, G. S., "Transonic Flow About a Thick Circular-Arc Airfoil", AIAA J., Vol. 14, No. 5, pp. 600-613 (1976).

6. Orloff, K. L., and Olson, L., "High-Resolution LDA Measurements of Reynolds Stresses in Boundary Layers and Wakes", 11th AIAA Aerodynamic Testing Conference, Colorado Springs, Colorado (1980).

7. Bauer, F., Garabedian, P., and Korn, D., "Supercritical Wing Sections", Lecture Notes in Economic and Mathematical Systems, No. 66, Springer- Verlag, New York (1972).

8. Lee, J. D., Gregorek, G. M., and Korkan, K. D.,"Testing Techniques and Interference Evaluation in the OSU Transonic Airfoil Facility", AIAA Paper No. 78-1118,Seattle, Washington (1978).

9. Satyanarayana, B., and Davis, S., "Experimental Studies of Trailing Edge Conditions on an Oscillating Airfoil at Frequency Parameters of Up to One", AIAA Paper No. 77-450, San Diego, California (1977).

10. Davis, J. A., "Transonic Interference Effects in Testing of Oscillating Airfoils", Ph.D Dissertation, The Ohio State University (1982).

11. Pate, S. R., "Measurements and Correlations of Transition Reynolds Numbers on Sharp Cones at High Speeds", AEDC-TR-69-172 (1969).

12. Heiser, E. J., and Shand, A., "Lightweight Polymeric Pigment", Presented at TAPPI Coating Conference, San Francisco, California (1972).

13. McLaughlin, D. K., and Tiederman, W. G., "Biasing Correction for Individual Realization of Laser Anemometer Measurements in Turbulent Flows", Physics of Fluids, Vol. 16, No. 12, pp. 2082-2088 (1973).

14. Meyers, J. F., and Walsh, M. J., "Computer Simulation of a Fringe Type Laser Velocimeter",Proceedings of 2nd International Workshop on Laser Velocimetry, Purdue University, pp. 471-510 (1974).

15. Johnson, D. A., and Bachalo, W. D., "Transonic Flow Past a Symmetrical Airfoil -- Inviscid and Turbulent Flow Properties", AIAA Journal, Vol. 18, No. 1 pp. 16-24 (1978).

16. Escudier, M. P., "The Distribution of Mixing Length in Turbulent Flows Near Walls", Imperial College, London, Rept. TWF/TN/1 (1965).

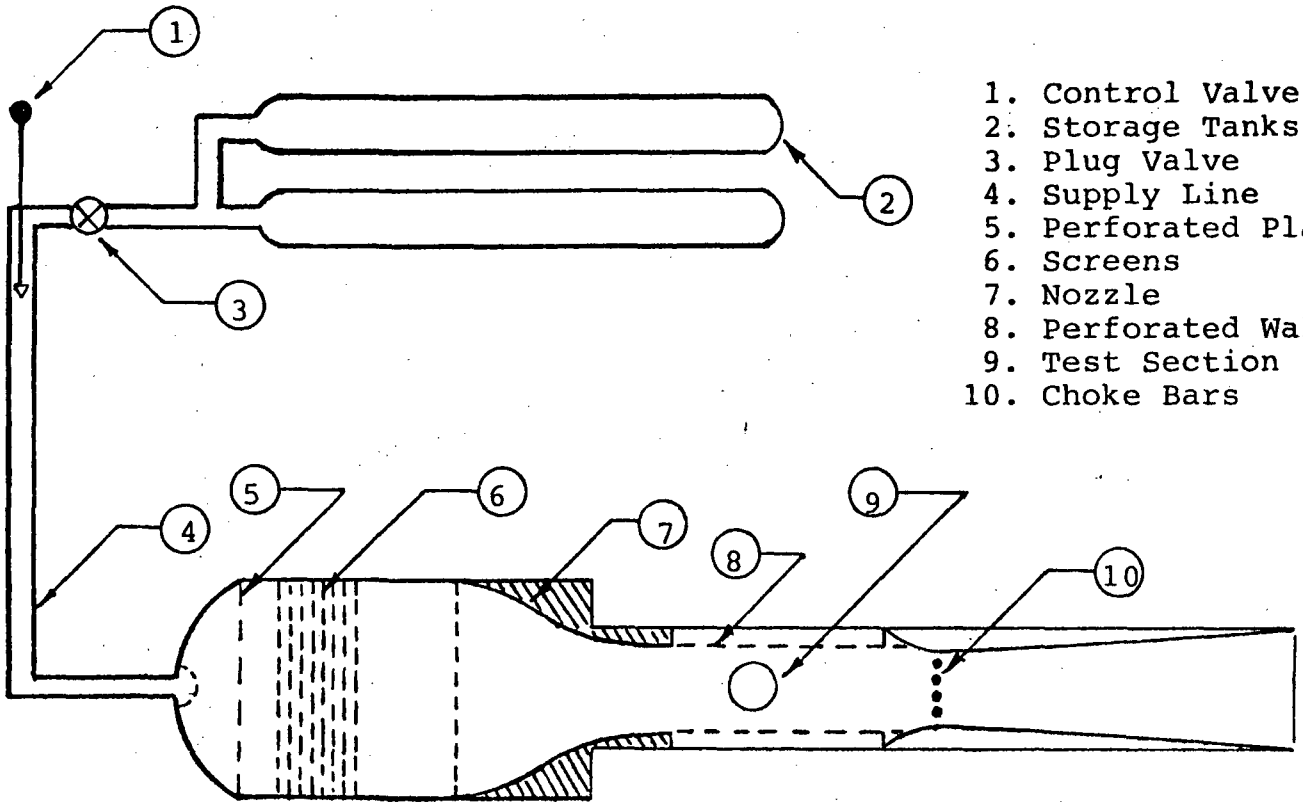

Figure 1. - Schematic of 6 x 22 Transonic Airfoil Tunnel

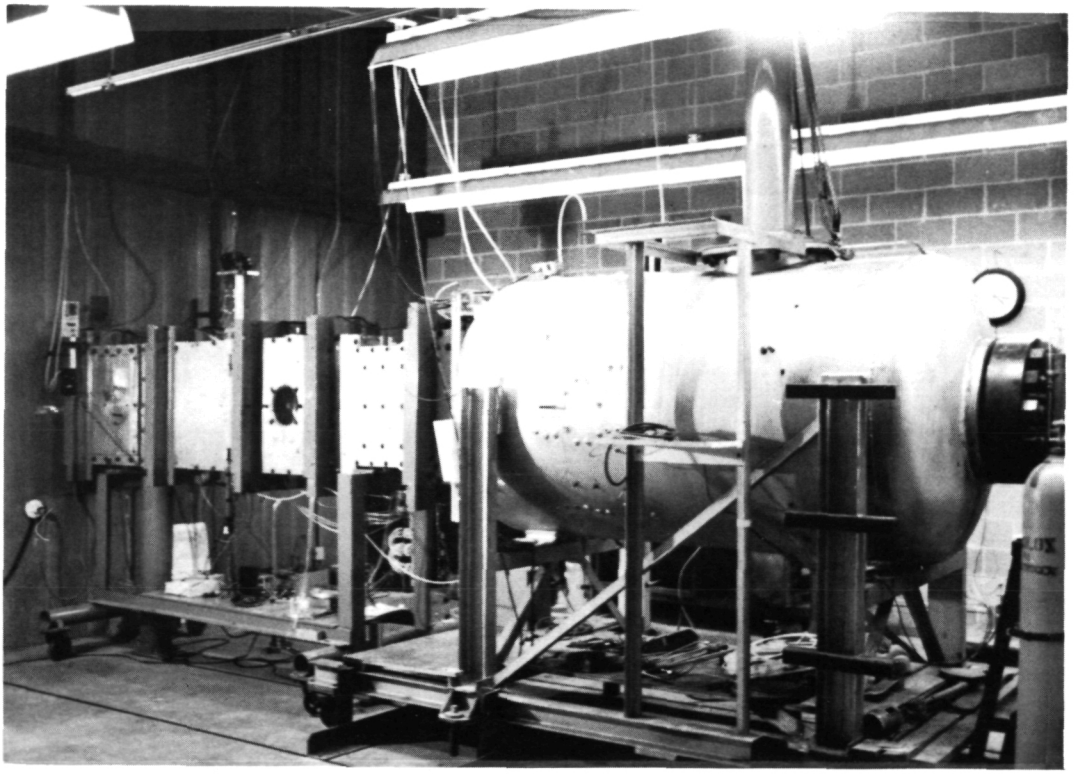

Figure 2. - The OSU Transonic Airfoil Wind Tunnel

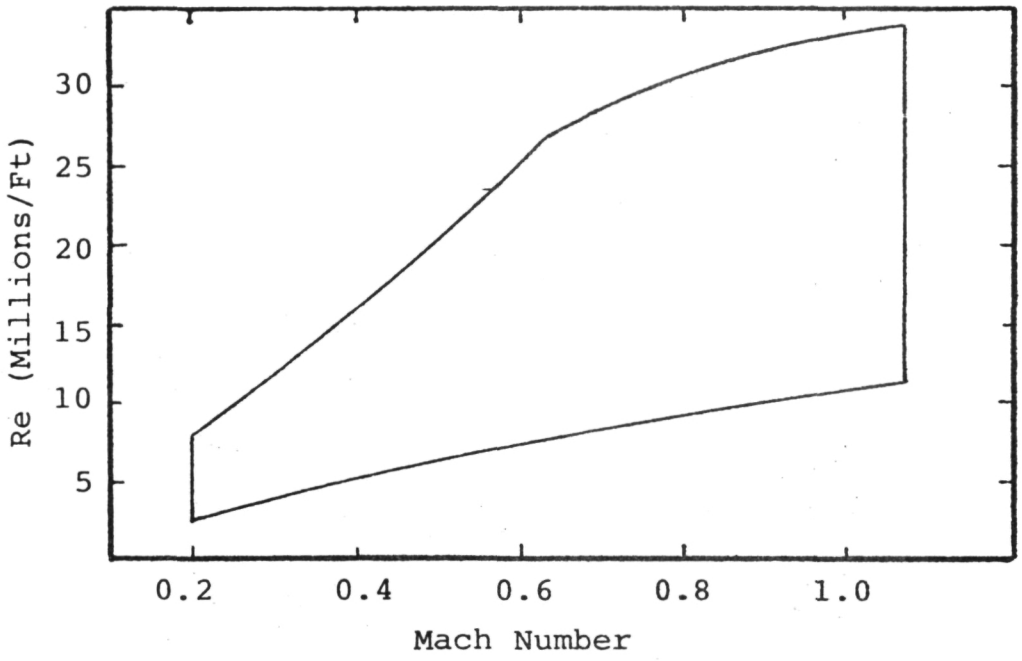

Figure 3. - Wind Tunnel Operating Envelope

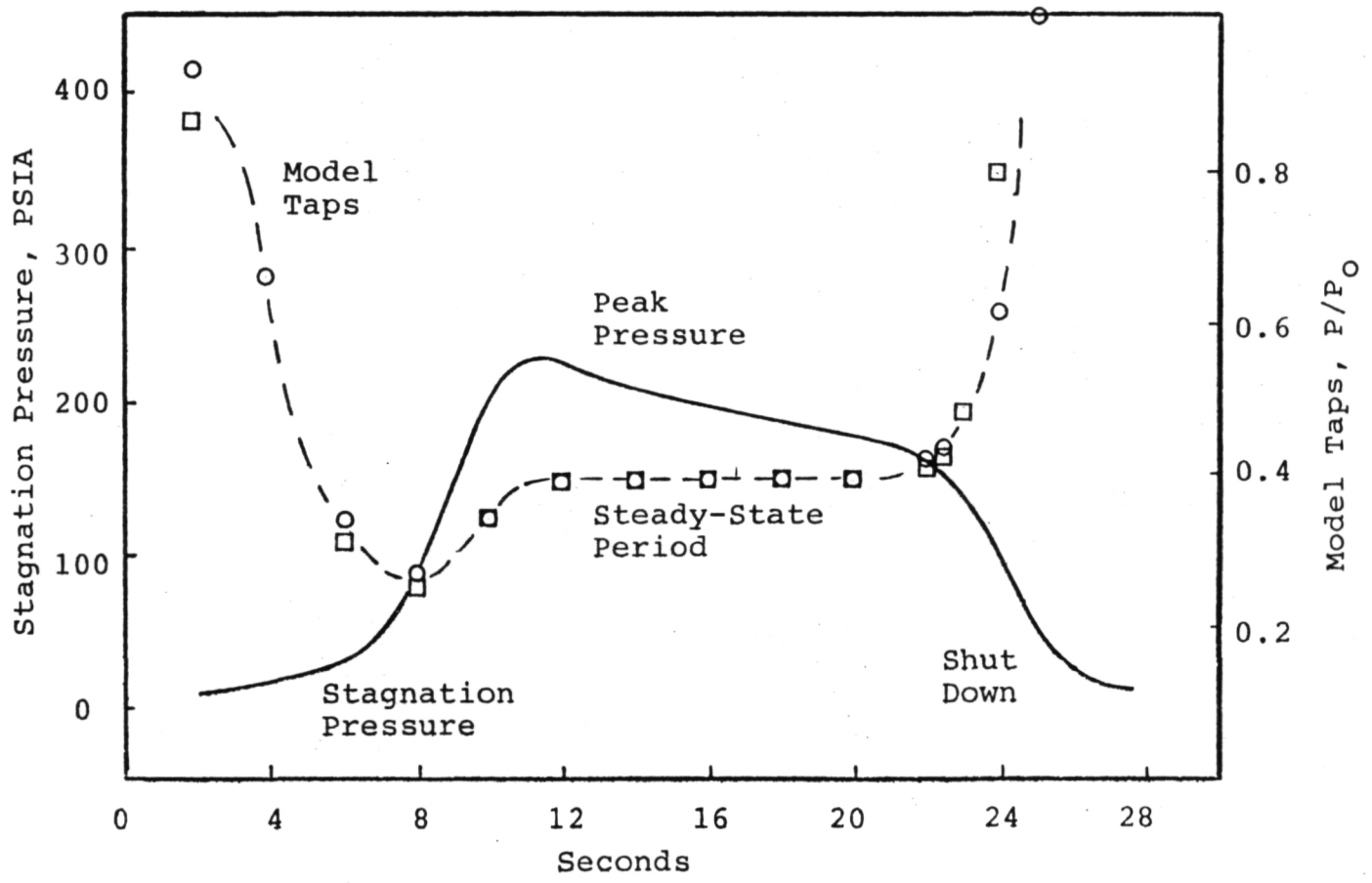

Figure 4. - Typical Tunnel Operating History

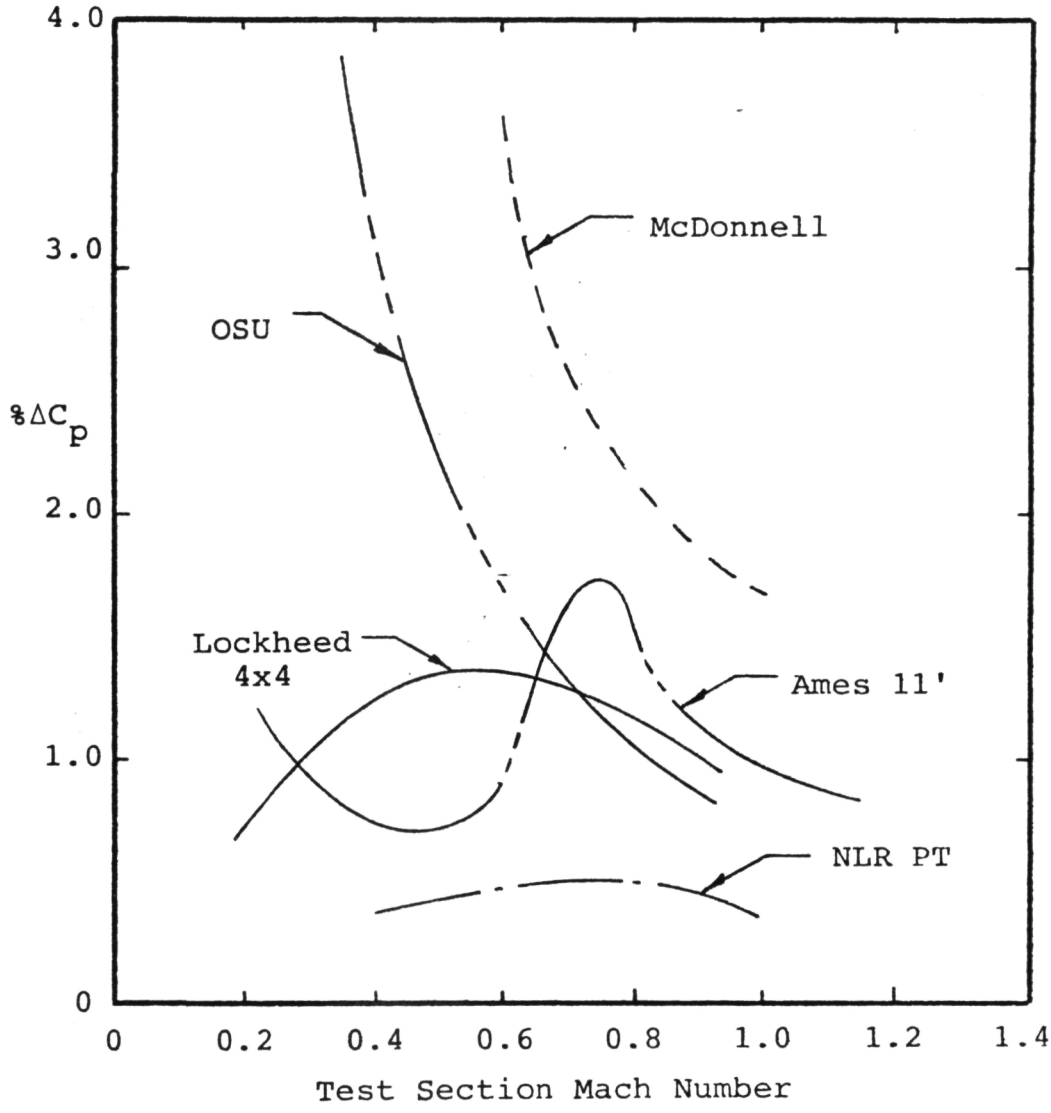

Figure 5. - Comparisons of Noise Levels in Various Wind Tunnels

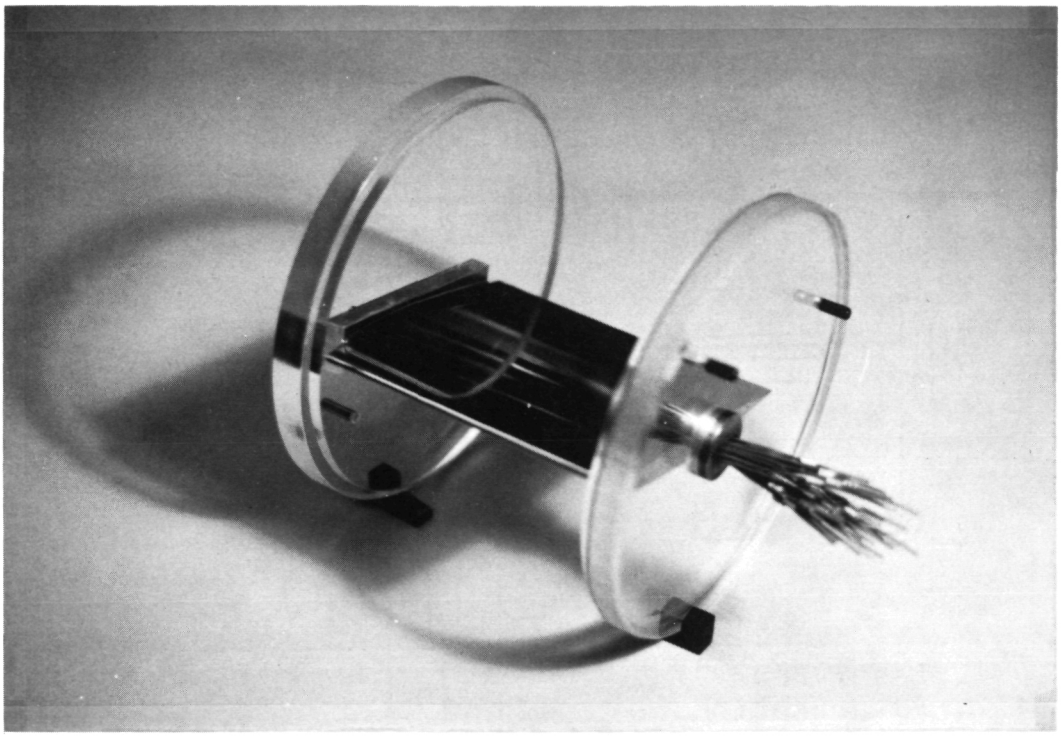

Figure 6. - NACA 64A010 Wind Tunnel Model

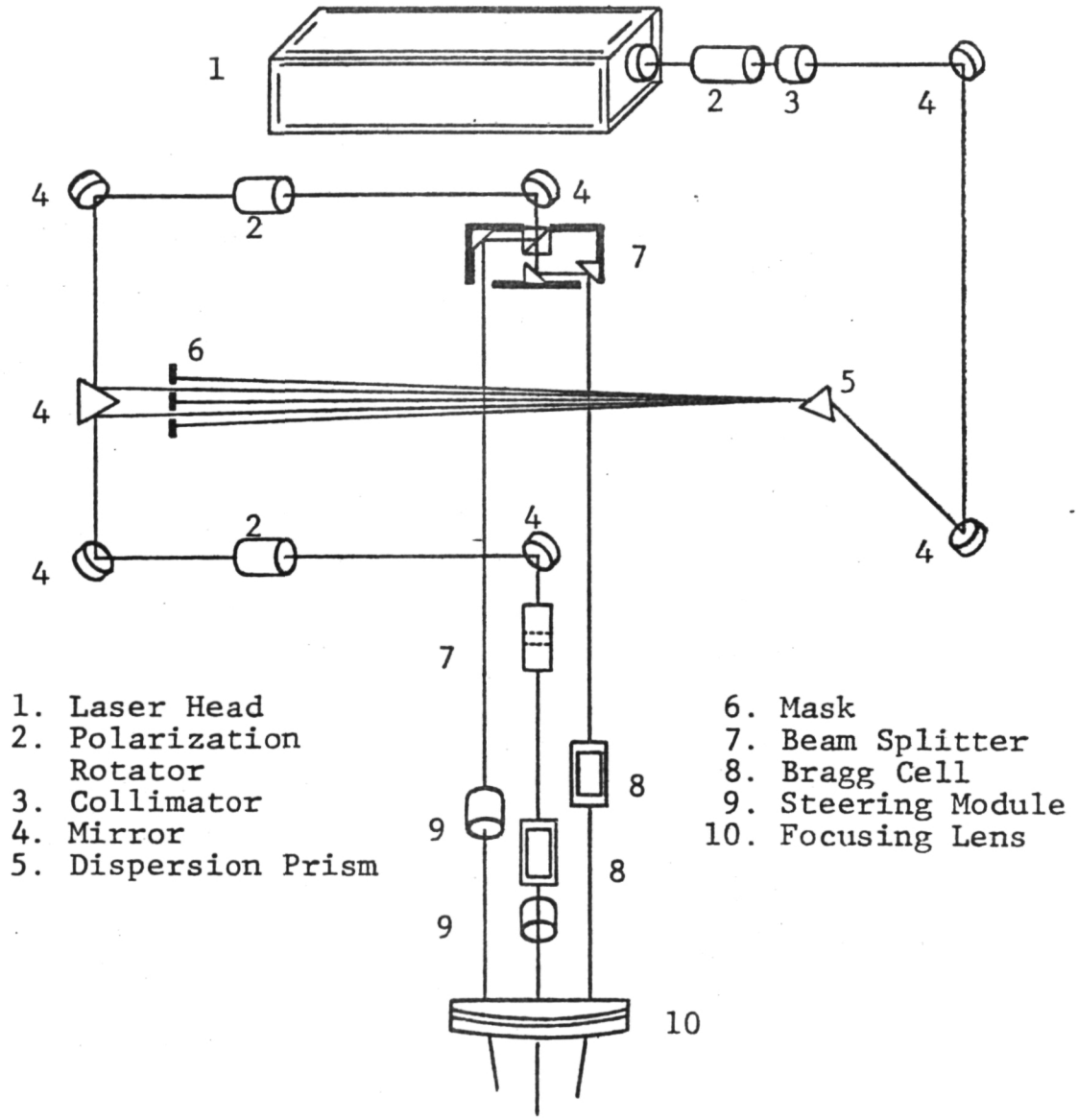

Figure 7. - LDV Transmission Optics Schematic

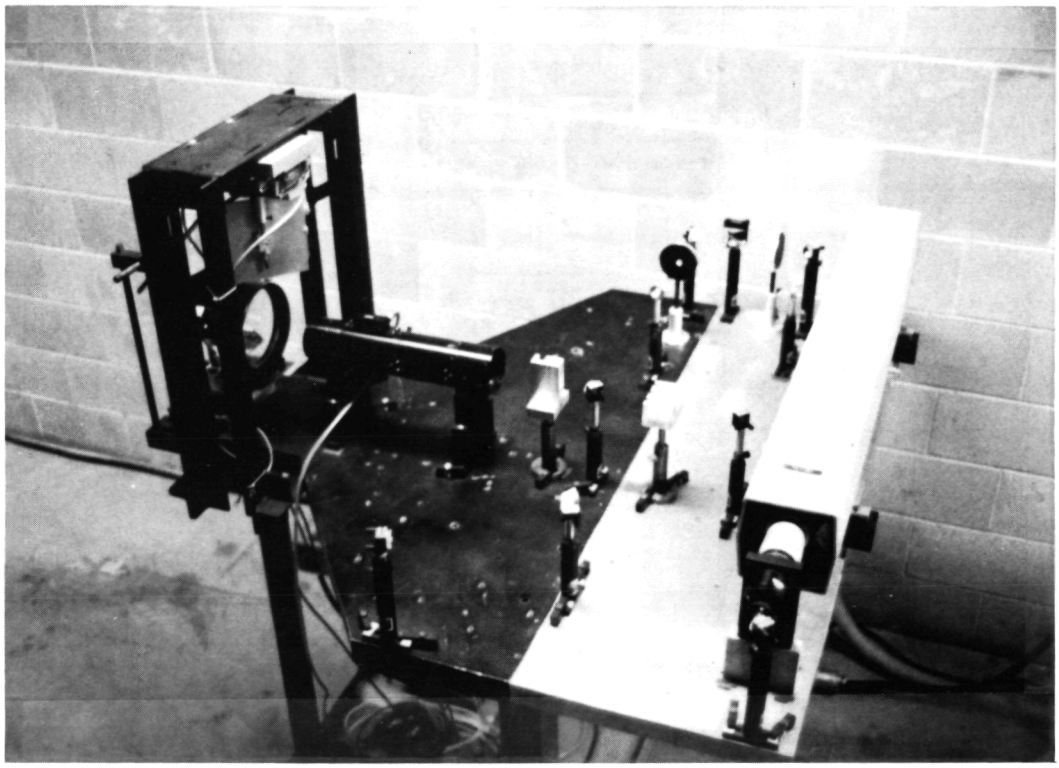

Figure 8. - LDV Transmitting Optics Assembly

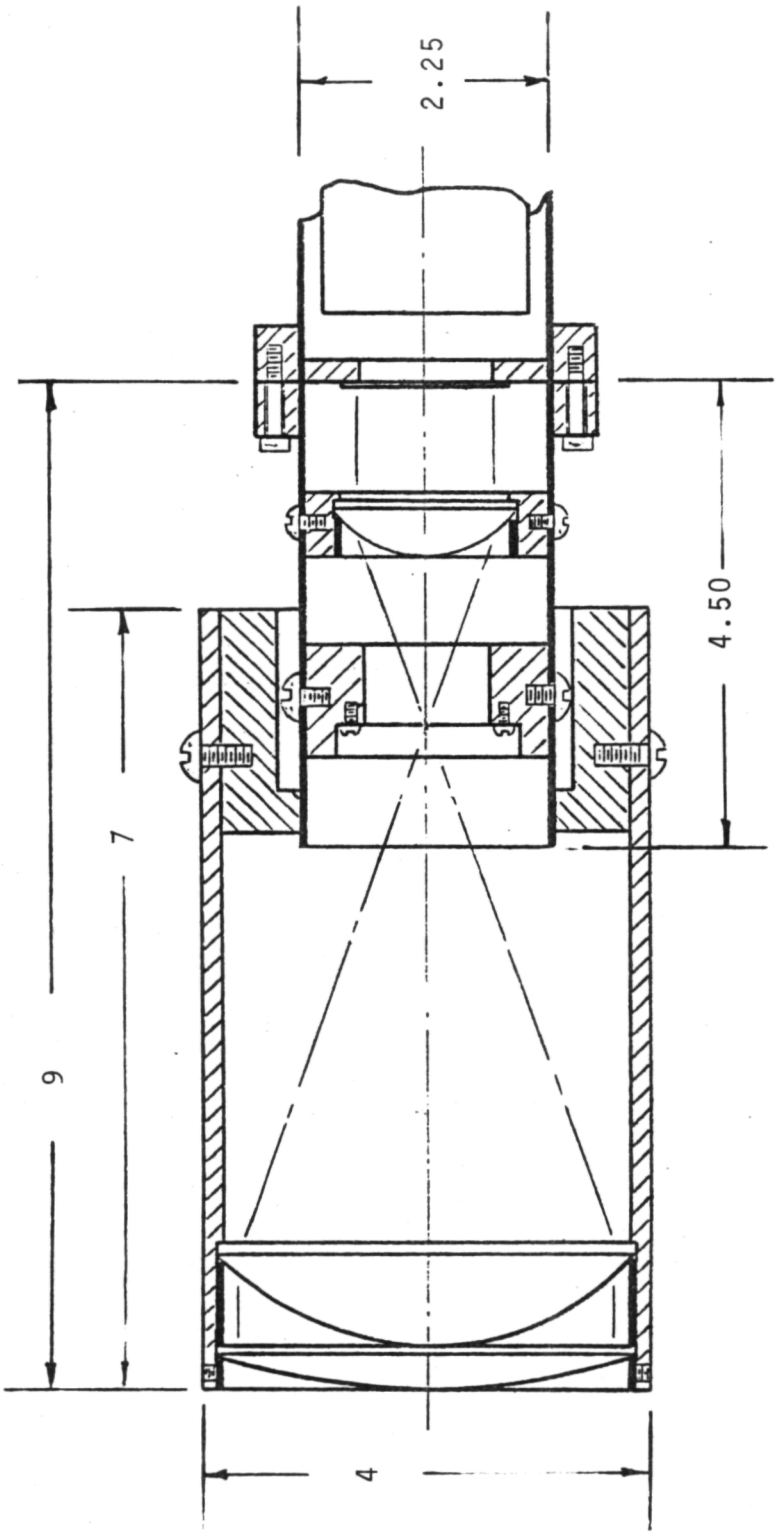

Figure 9. - LDV Receiving Optics Schematic

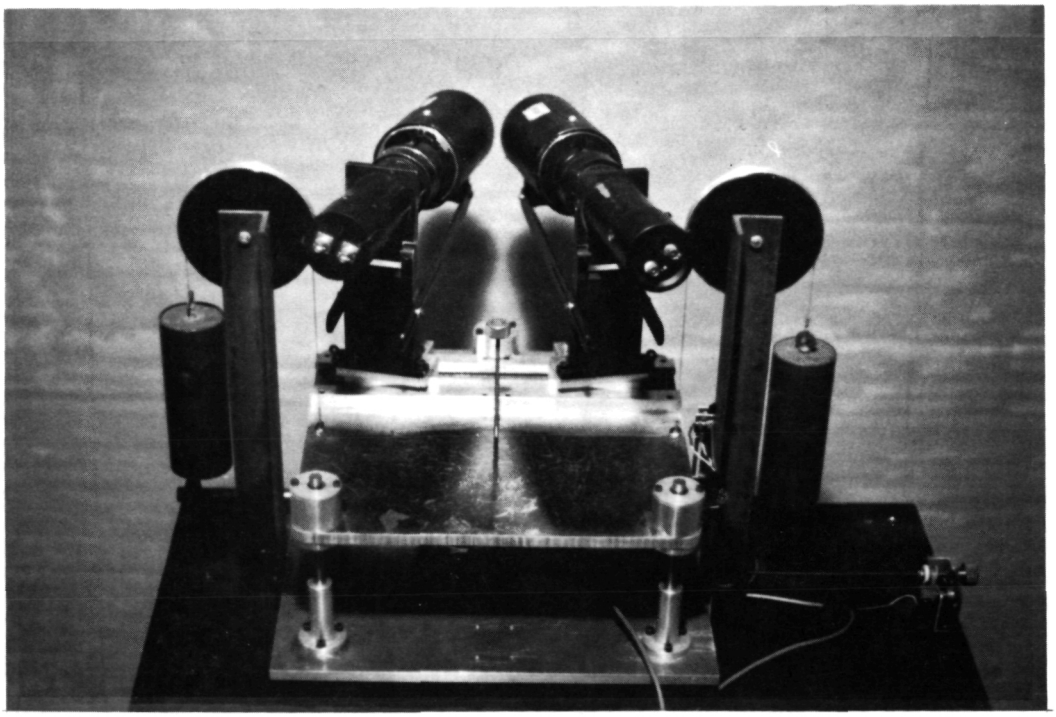

Figure 10. - LDV Receiving Optics Assembly

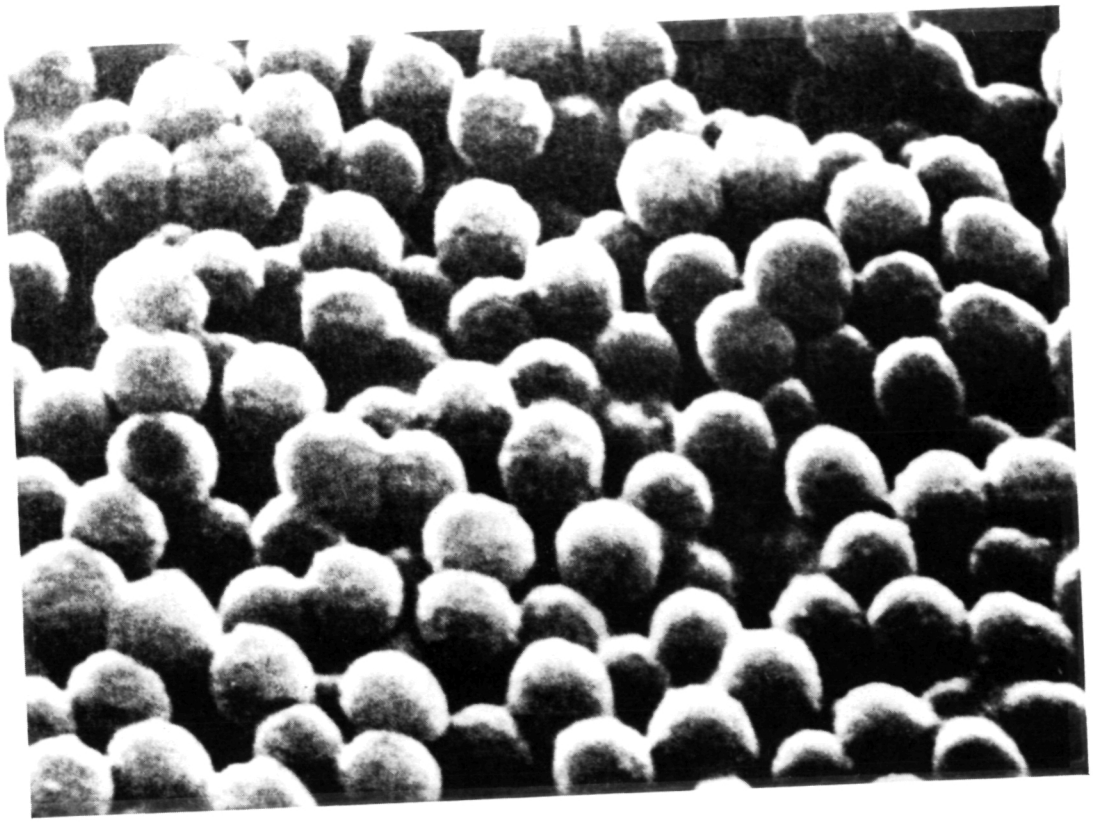

Figure 11. - Polystyrene Latex Seeding Material

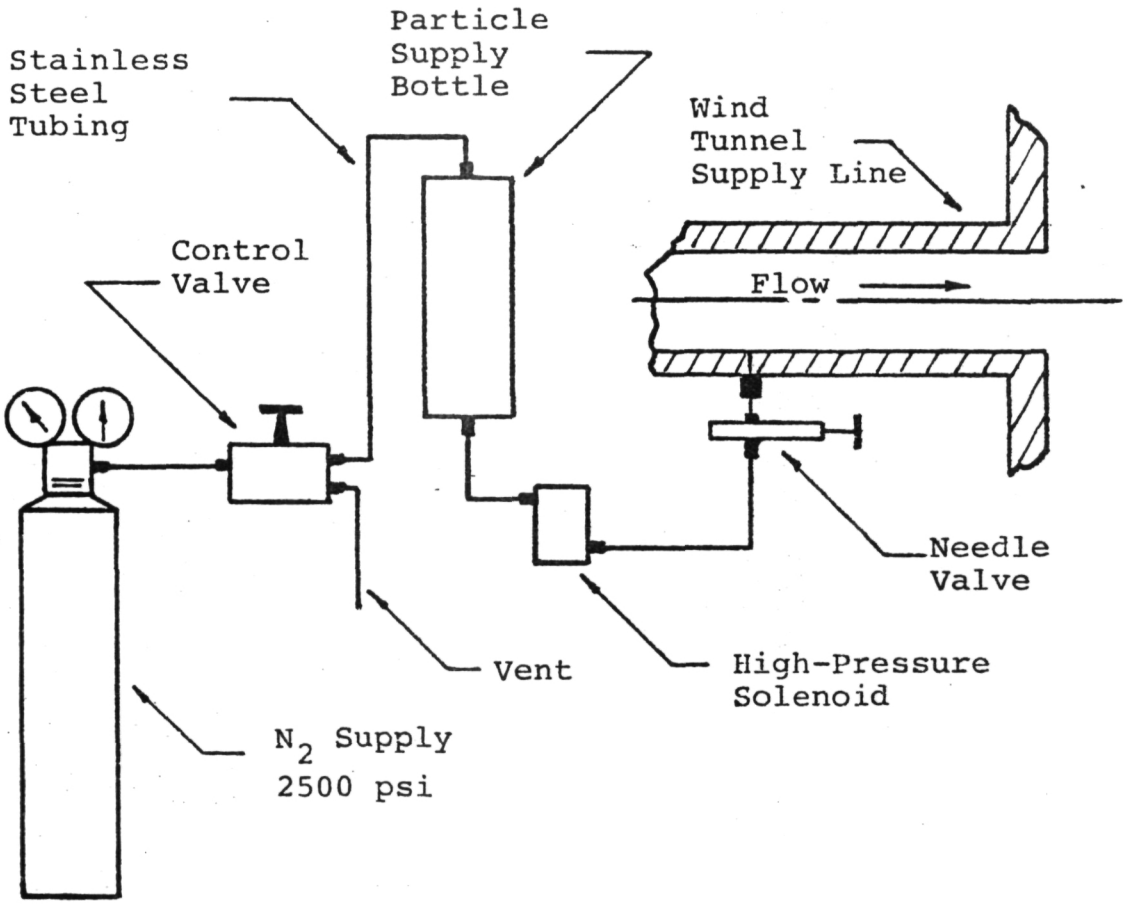

Figure 12. - Particle Injection System Schematic

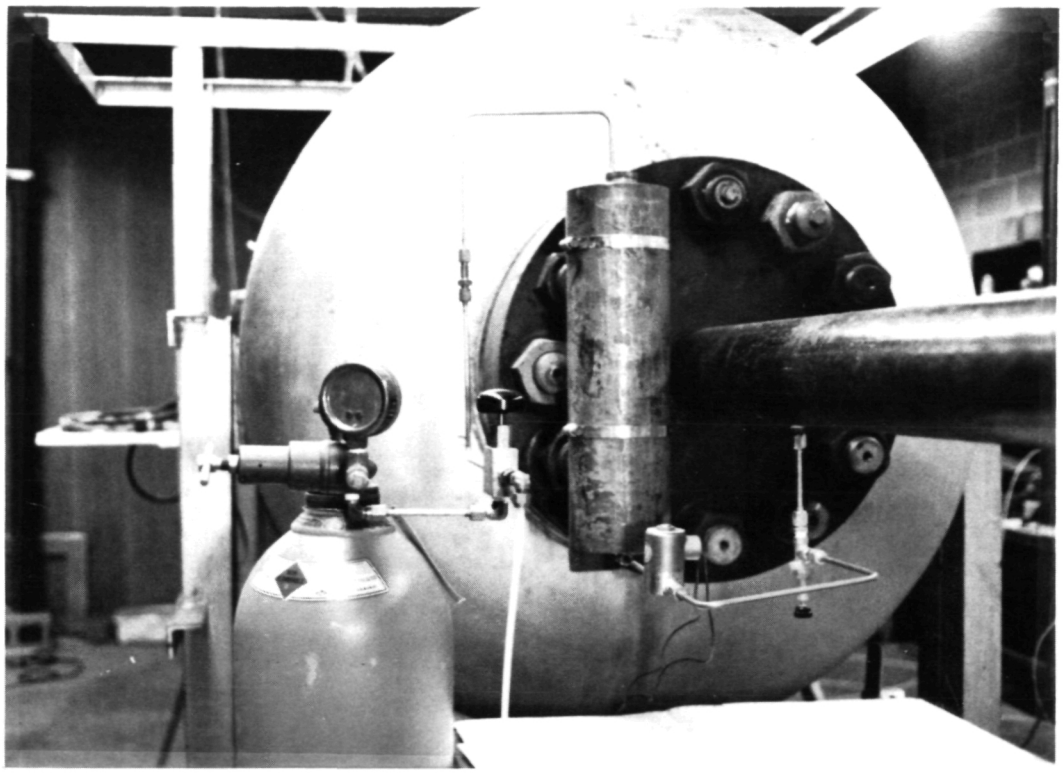

Figure 13. - Particle Injection System Assembly

CONTOUR VALUES (BOTTOM TO TOP)

1	32.90
2	41.81
3	50.71
4	59.61
5	68.52
6	77.42
7	86.32
8	95.23
9	104.13
10	113.03
11	121.93

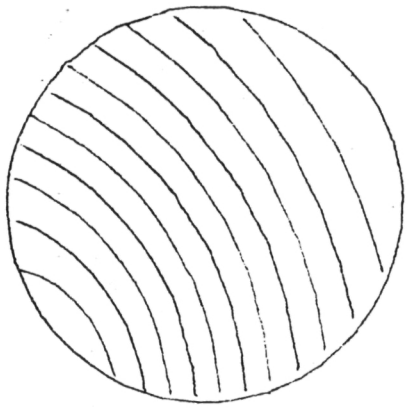

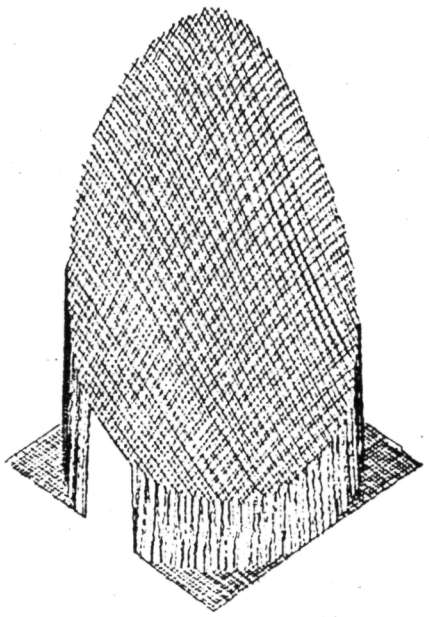

Figure 14. - Signal-To-Noise Ratios Over The Surface of The Collecting Lens

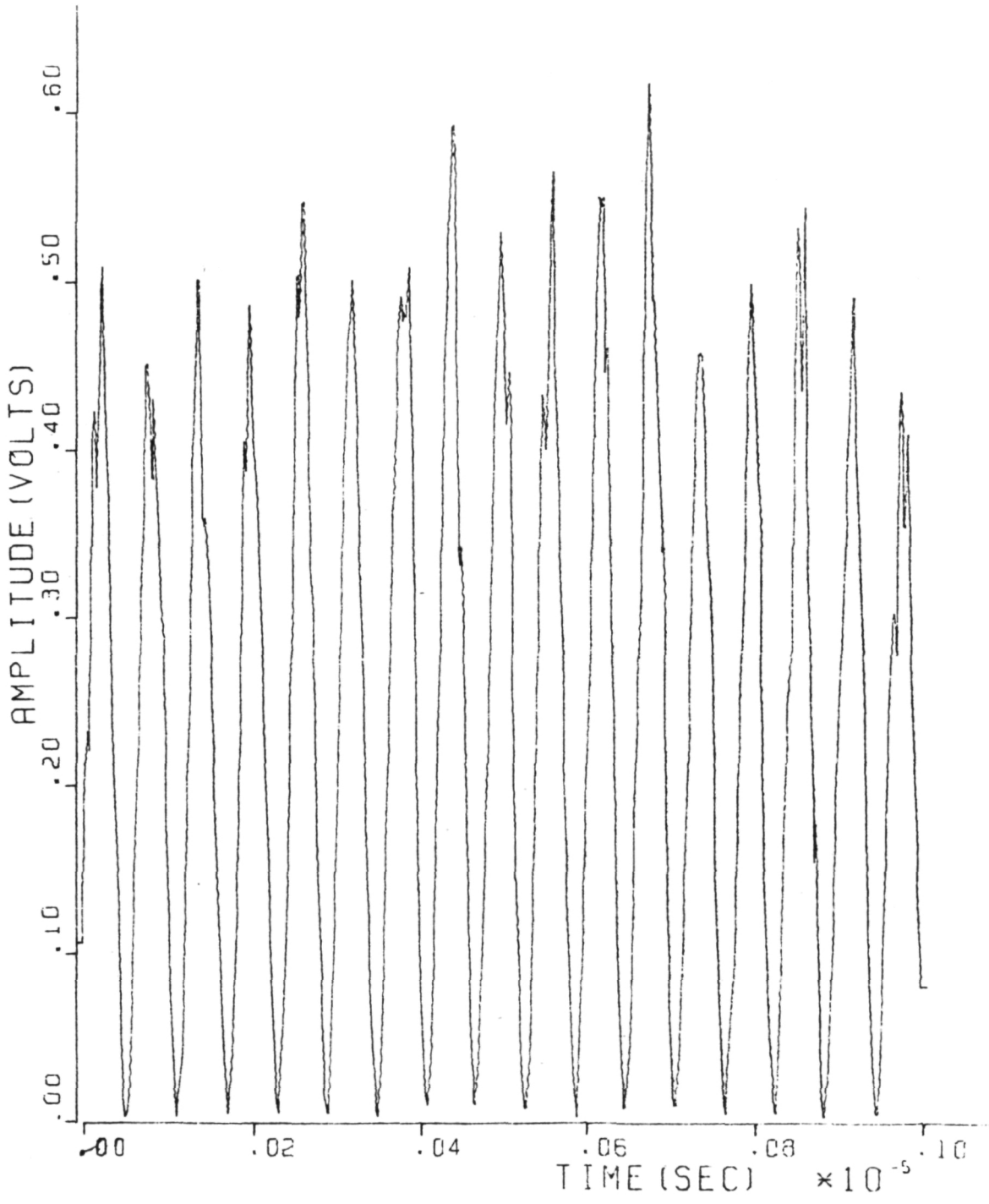

Figure 15. - Predicted Raw Signal For a 0.8 Micron Particle

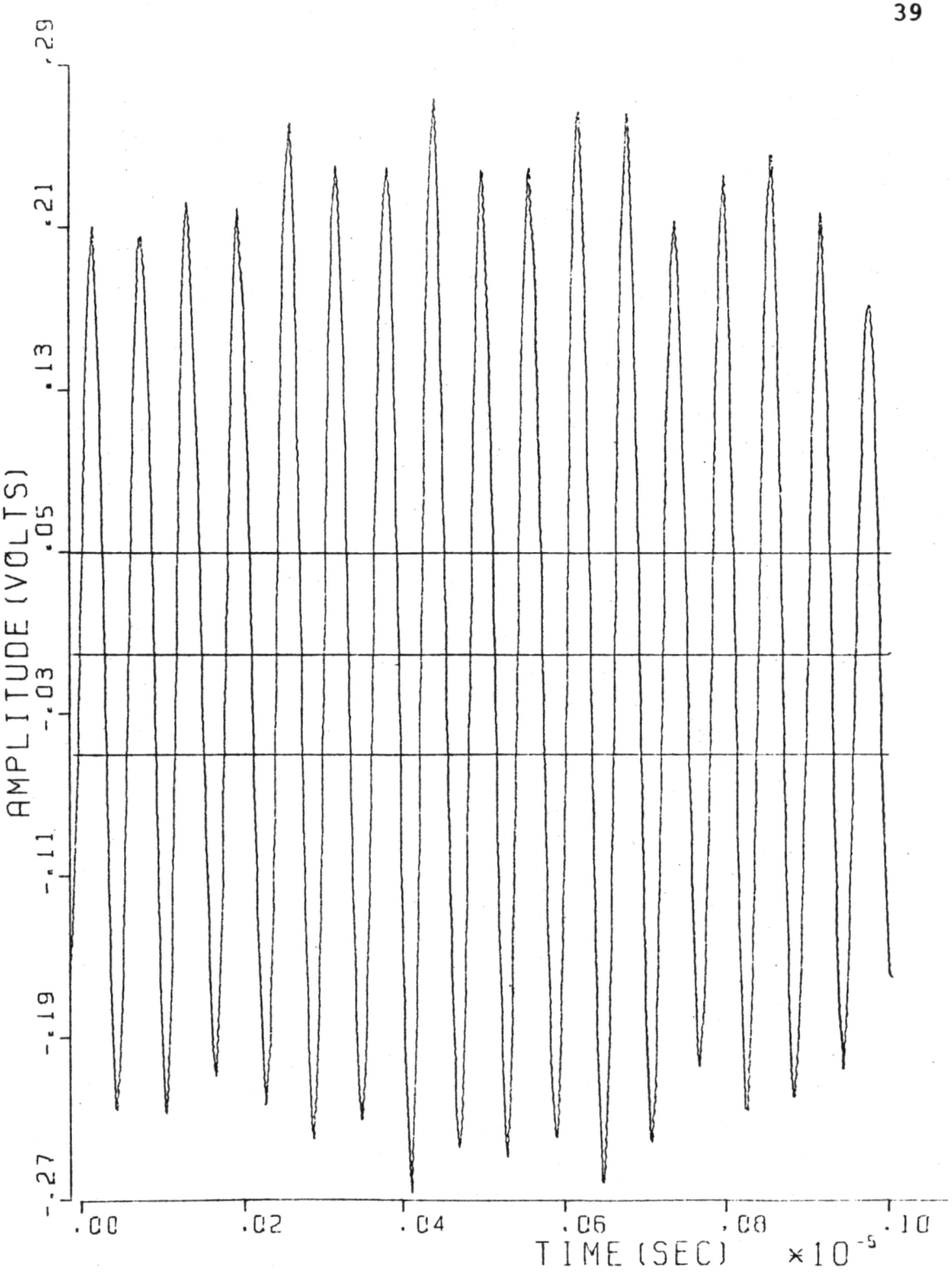

Figure 16. - Predicted Filtered Signal For a 0.8 Micron Particle

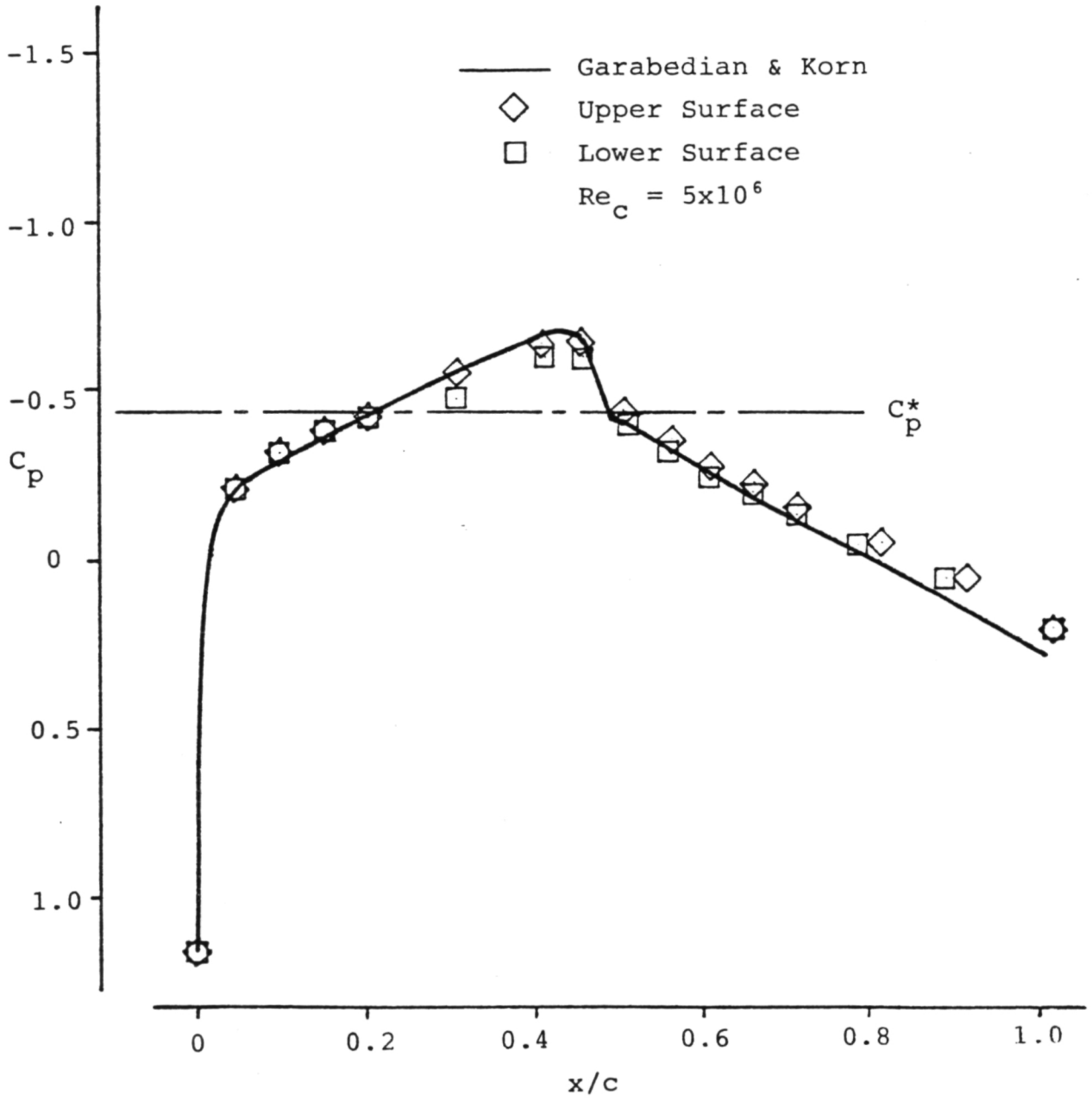

Figure 17. - Surface Pressures at Zero Angle of Attack

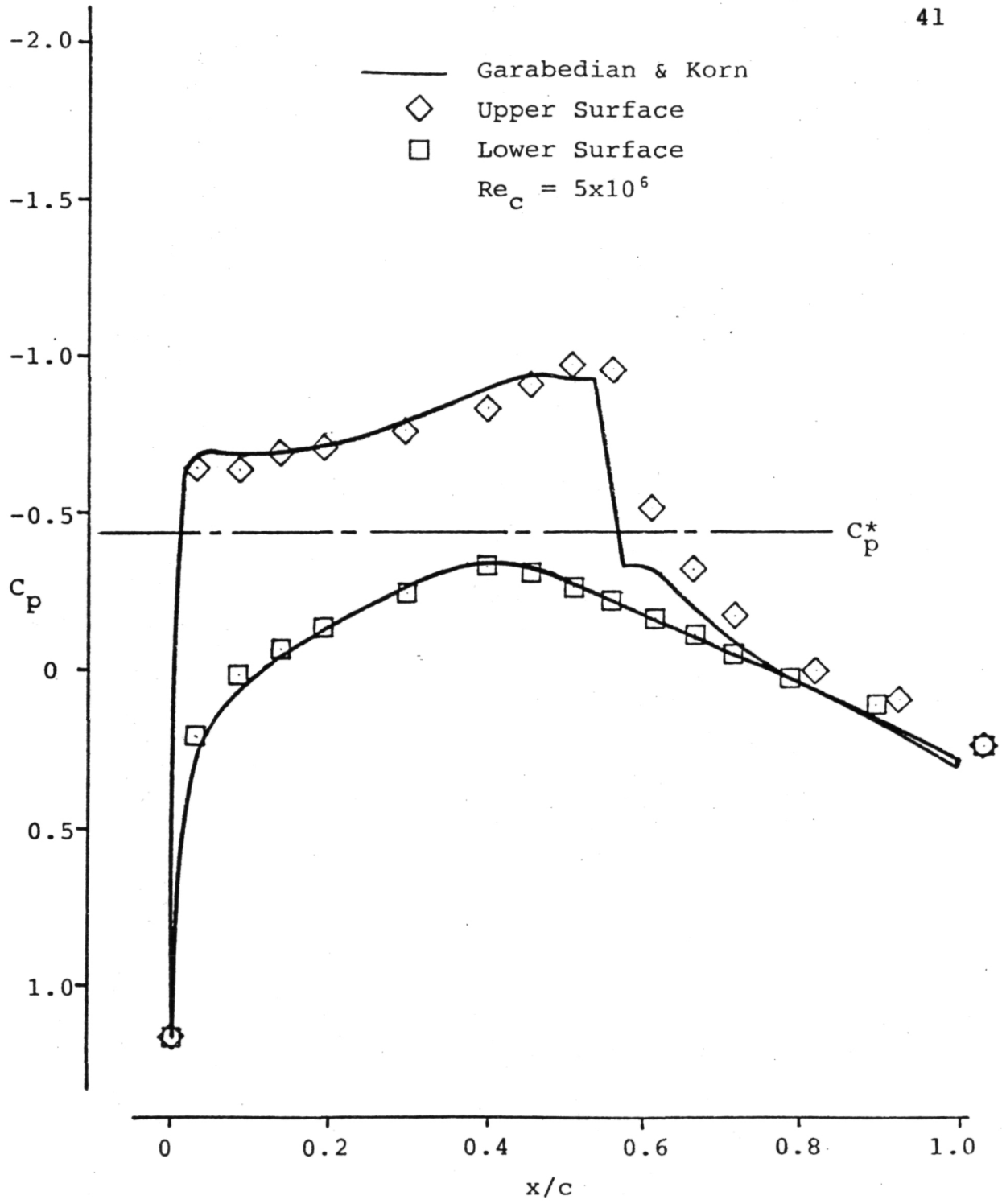

Figure 18. - Surface Pressures at 2 Degrees Angle of Attack

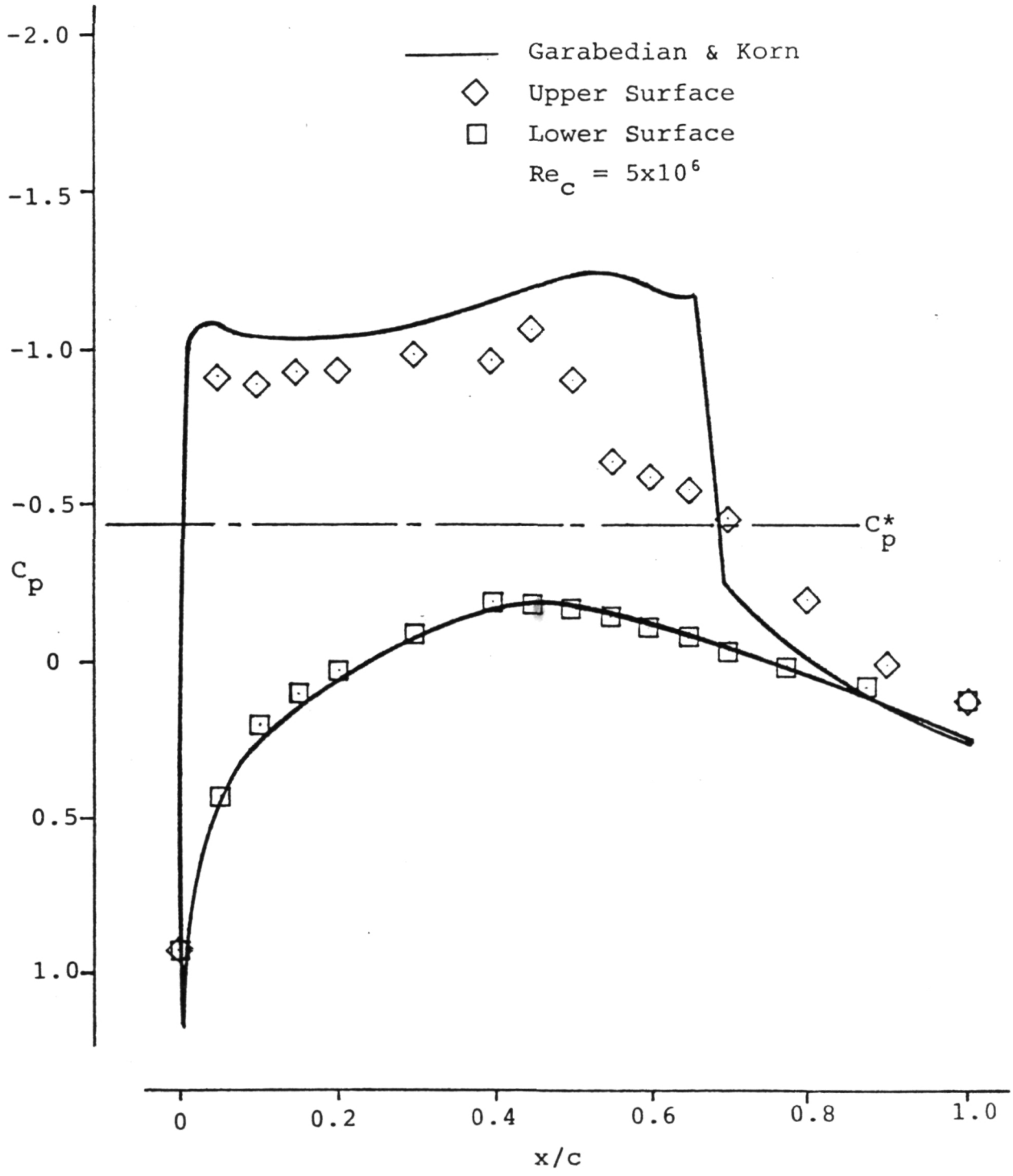

Figure 19. - Surface Pressures at 4 Degrees Angle of Attack

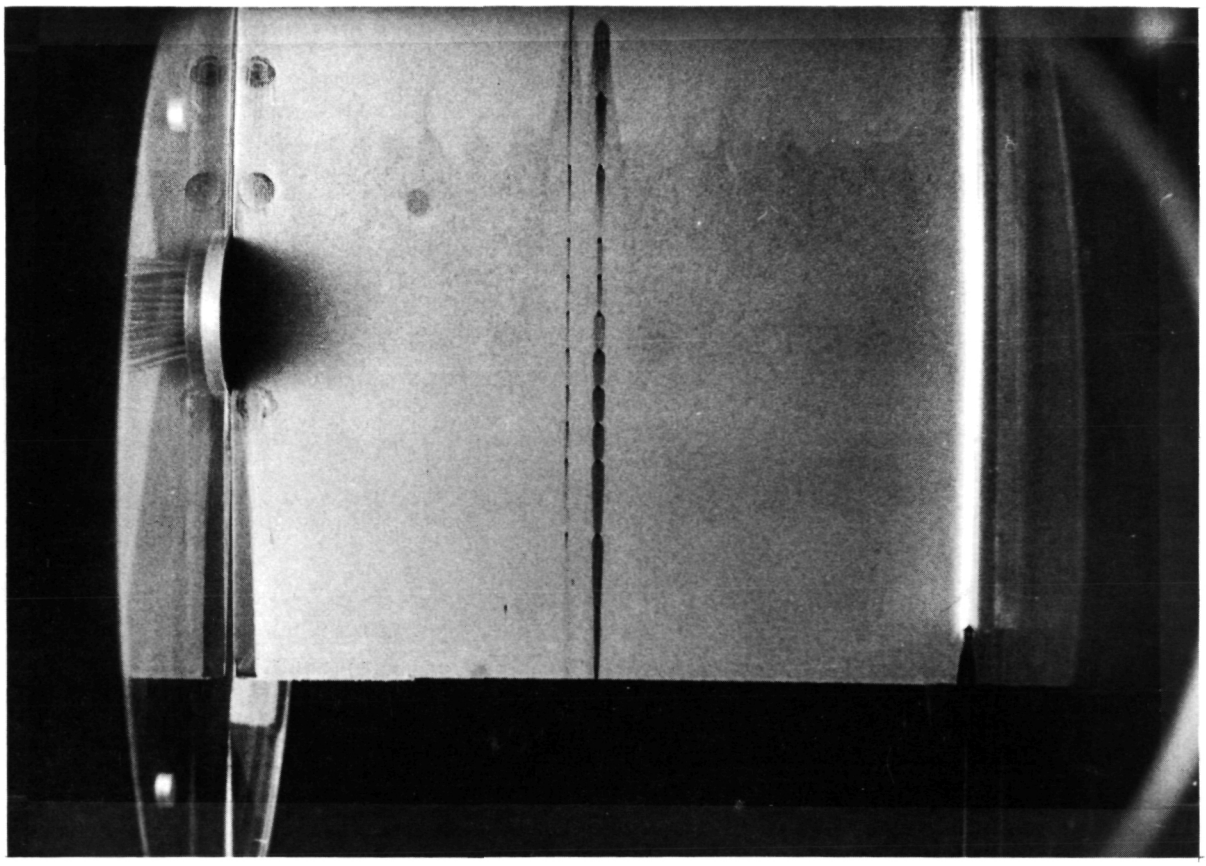

Figure 20. - Oil Flow Visualization at Zero Angle of Attack

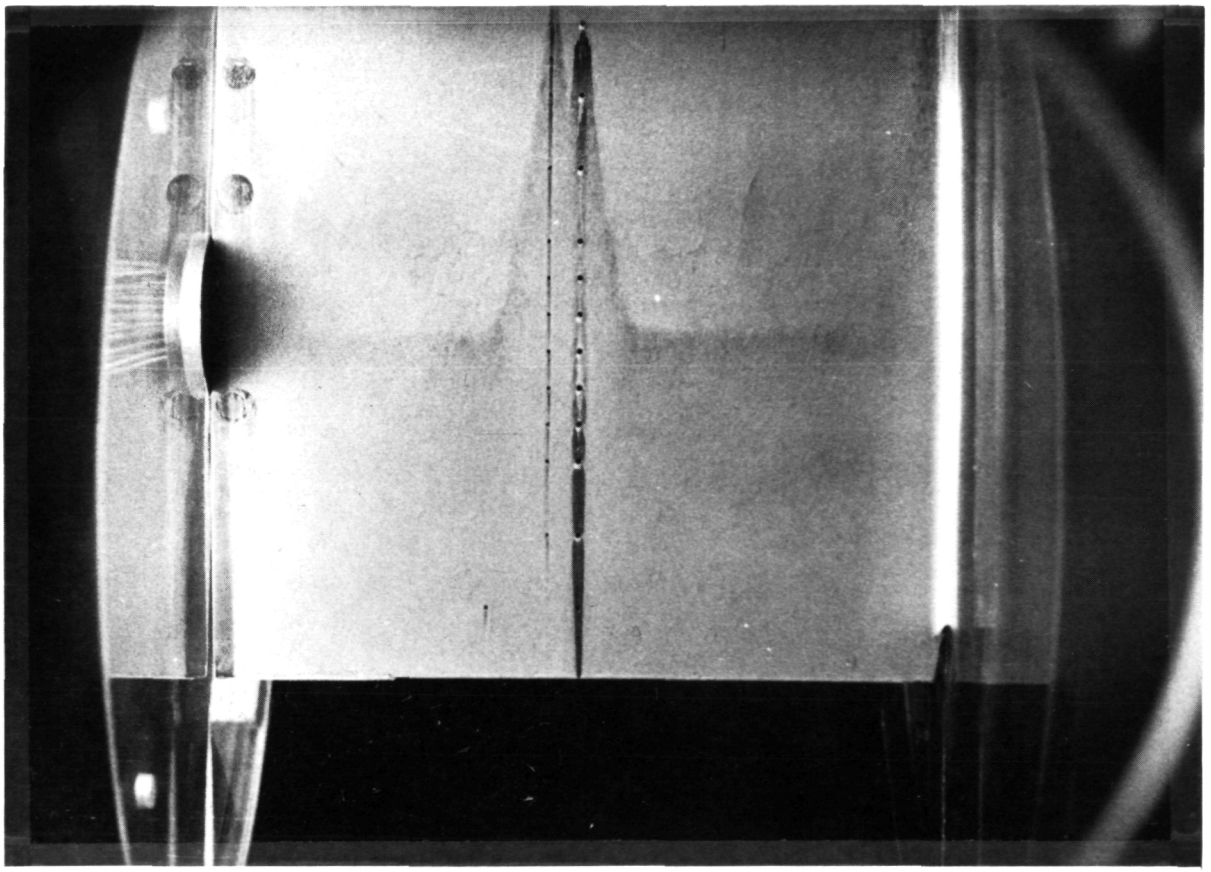

Figure 21. - Oil Flow Visualization at 2 Degrees Angle of Attack

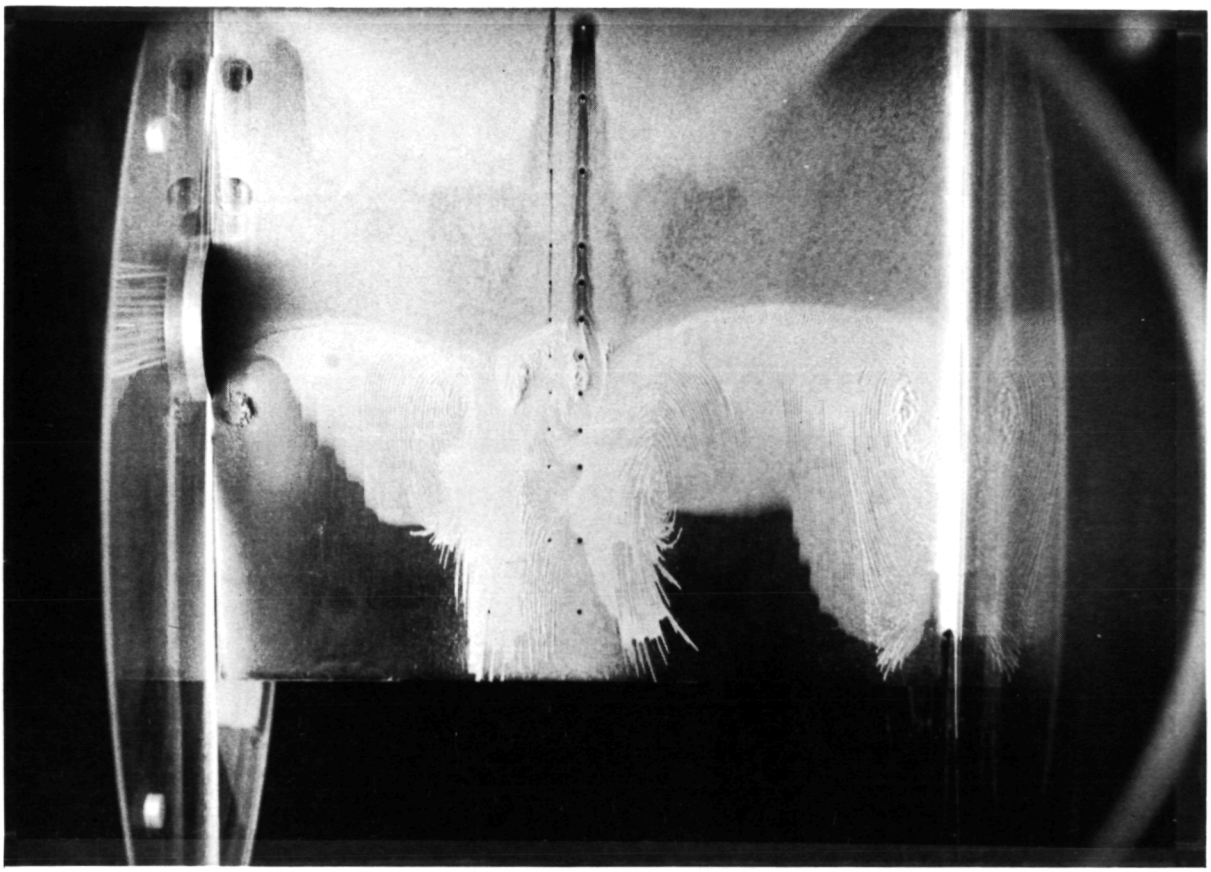

Figure 22. - Oil Flow Visualization at 4 Degrees Angle of Attack

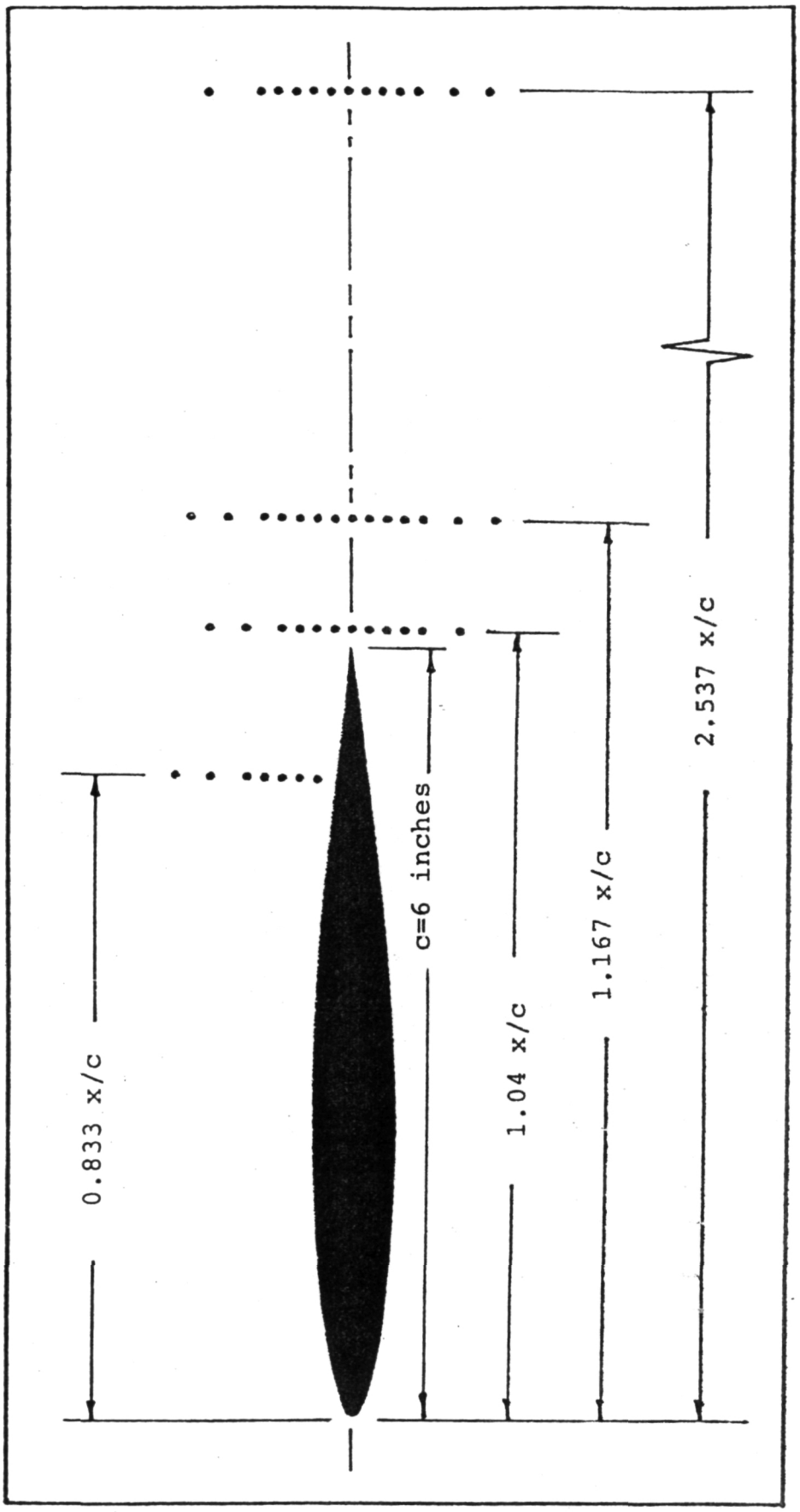

Figure 23. - Data Collection Locations

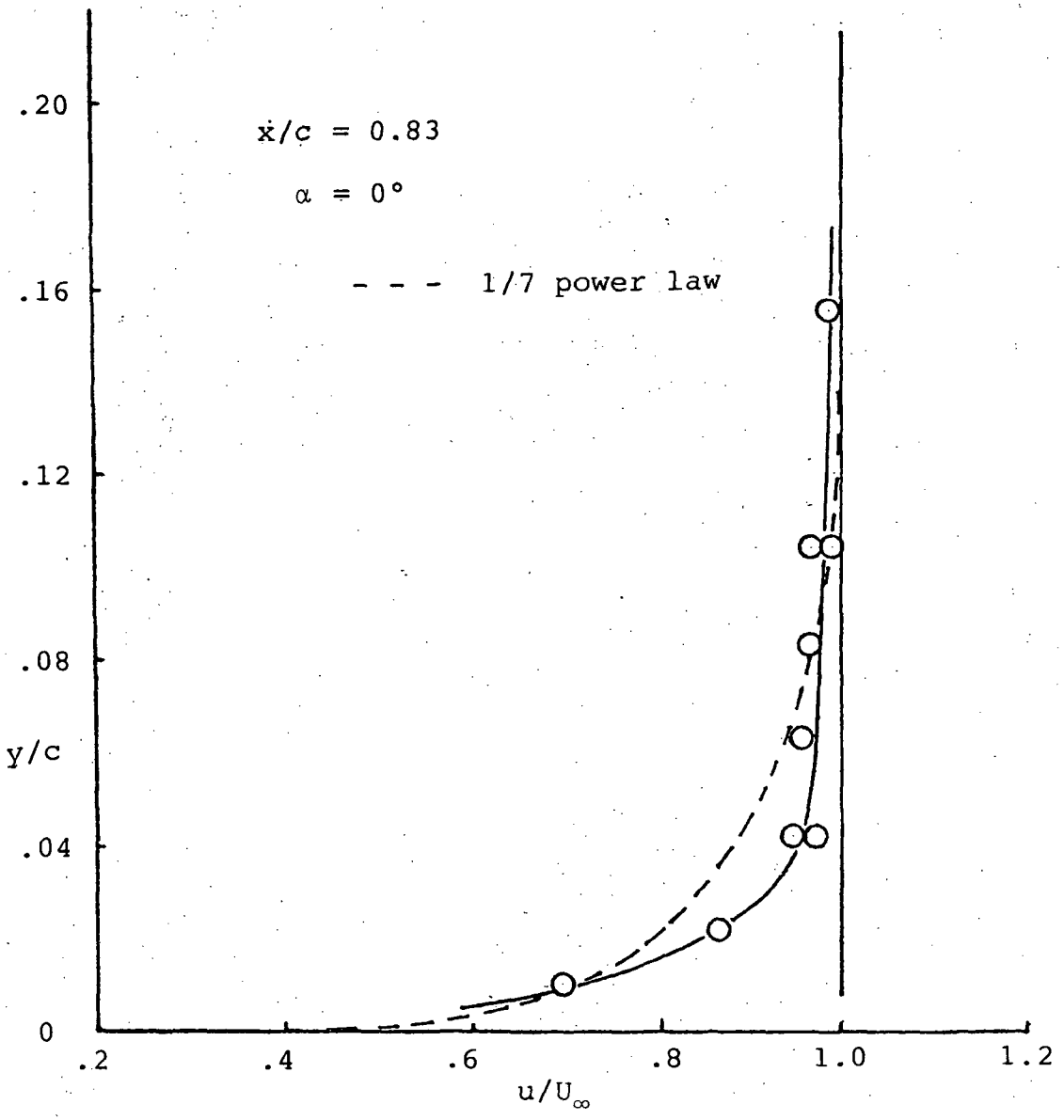

Figure 24. - Mean u Velocity Distribution; x/c = 0.83; Attack Angle = 0

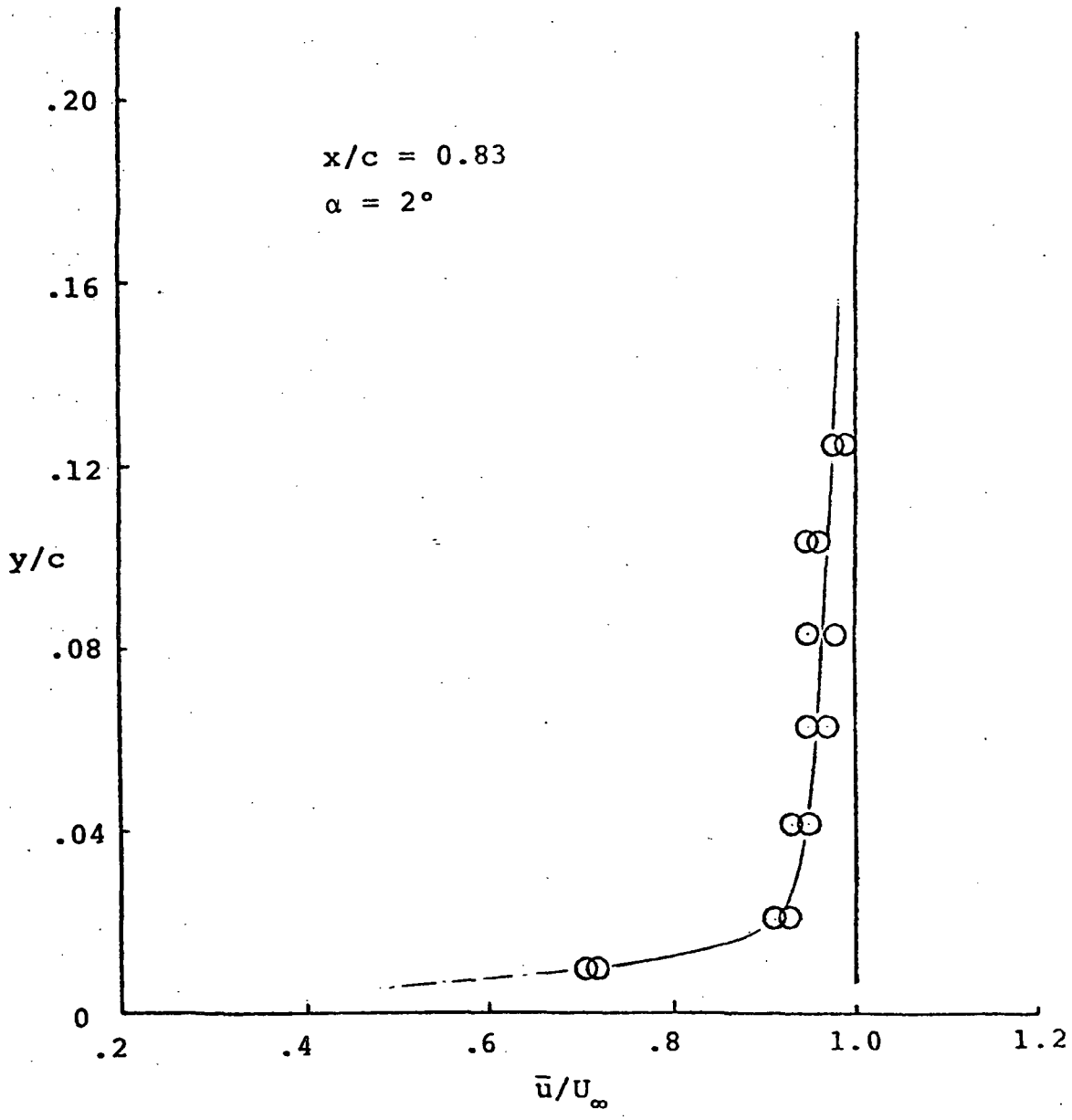

Figure 25. - Mean u Velocity Distribution;
x/c = 0.83; Attack Angle = 2 Degrees

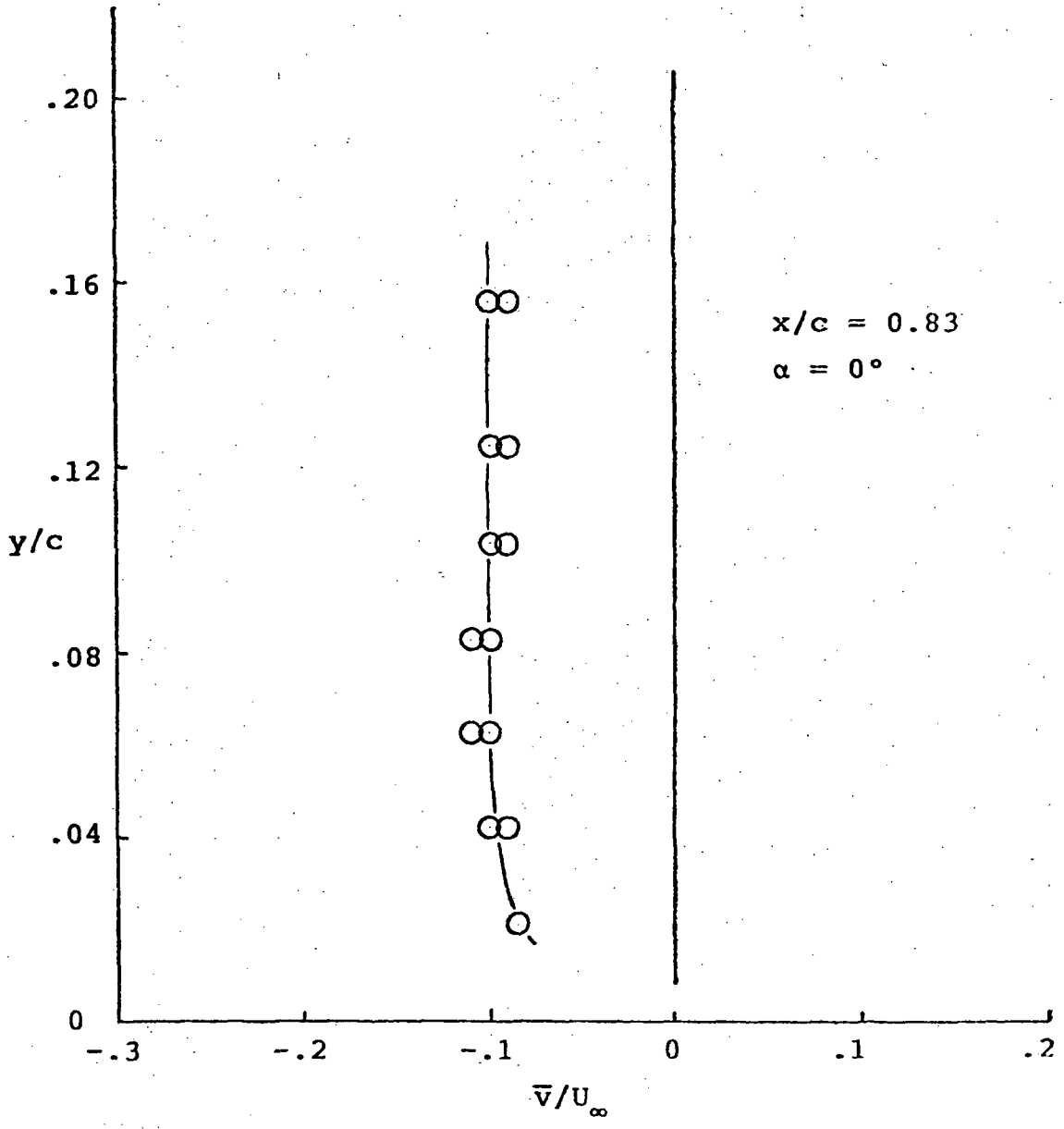

Figure 26. - Mean v Velocity Distribution;
x/c = 0.83; Attack Angle = 0 Degrees

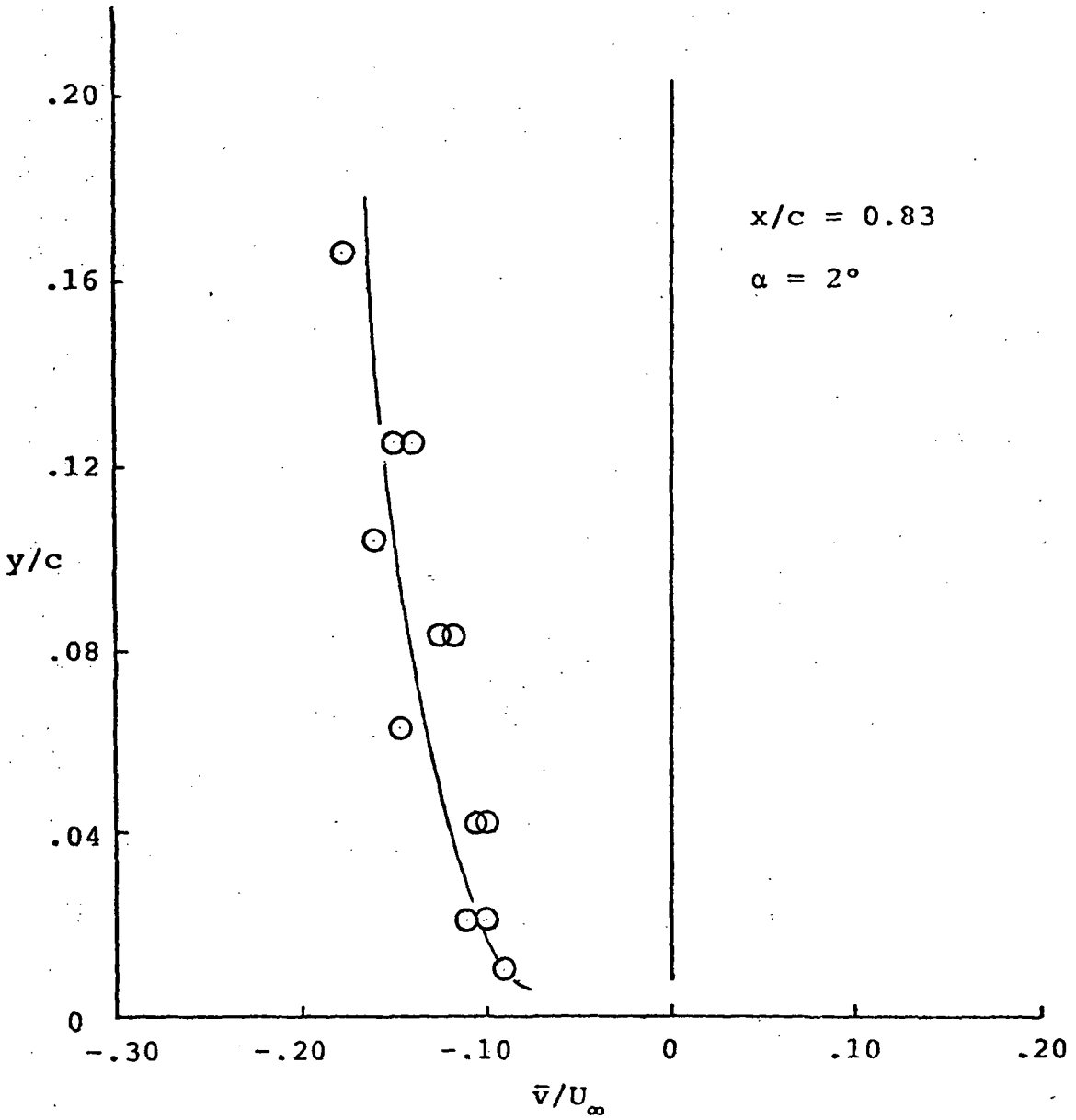

Figure 27. - Mean v Velocity Distribution;
x/c = 0.83; Attack Angle = 2 Degrees

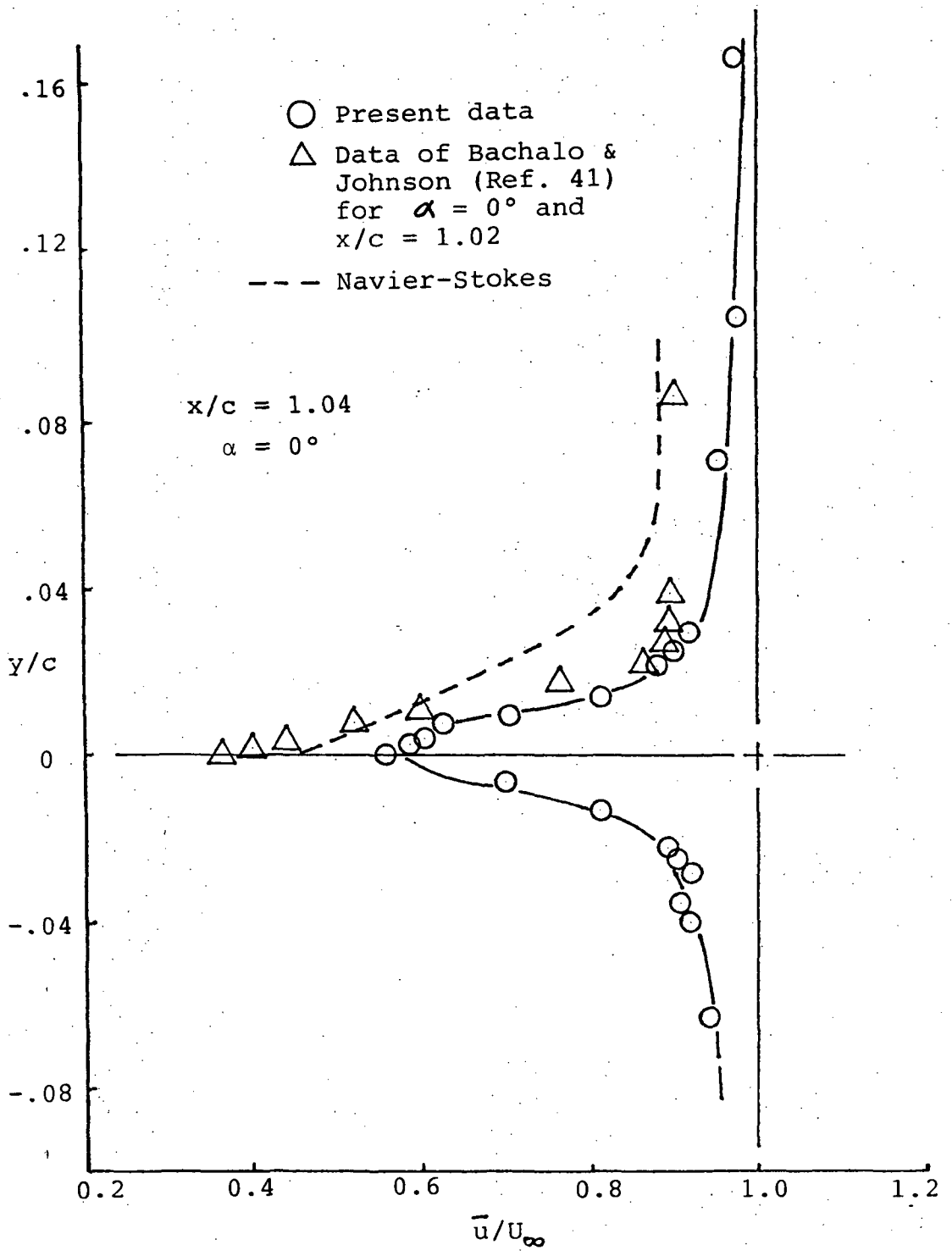

Figure 28. - Mean u Velocity Distributions; x/c = 1.04; Attack Angle = 0 Degrees

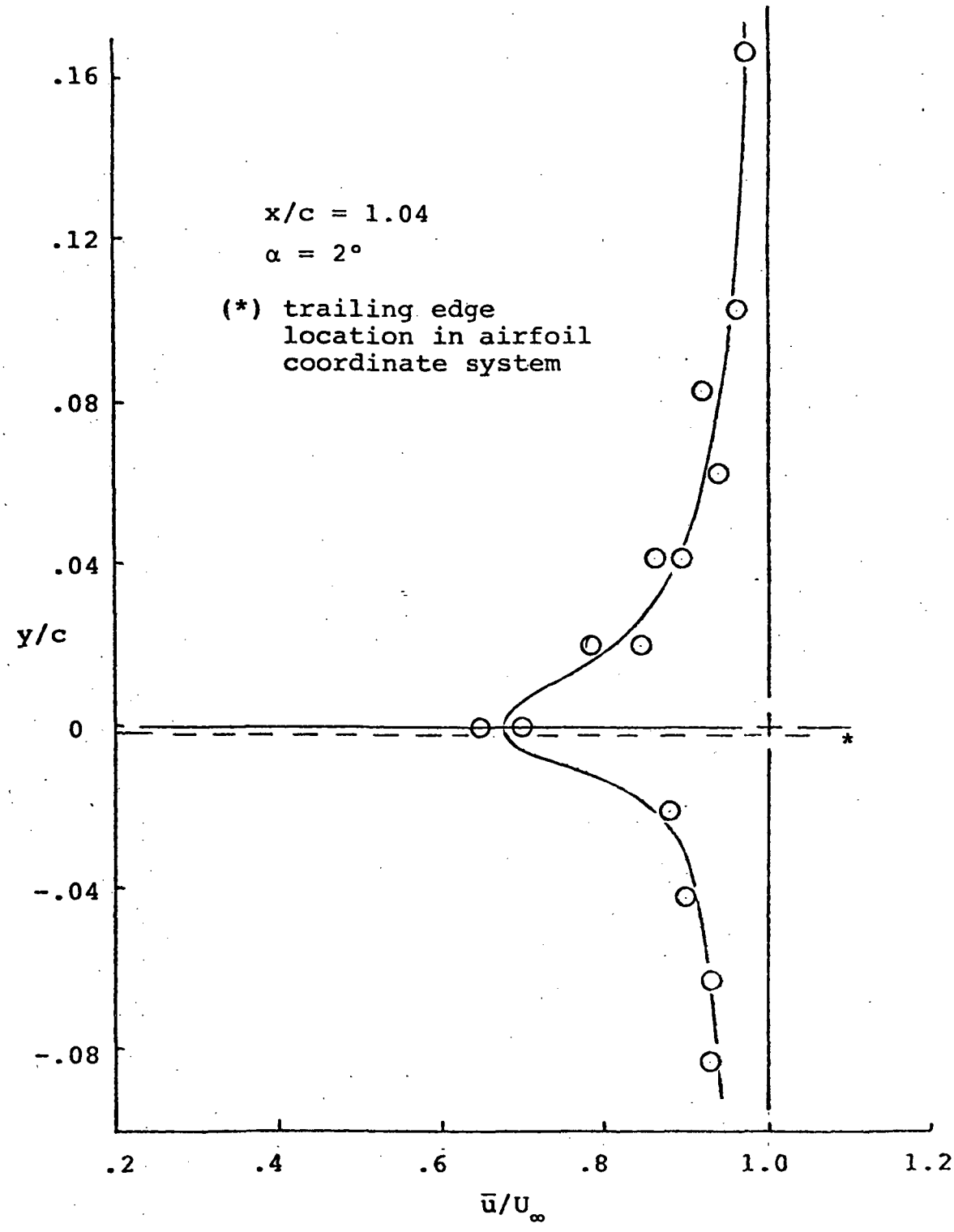

Figure 29. - Mean u Velocity Distributions;
x/c = 1.04; Attack Angle = 2 Degrees

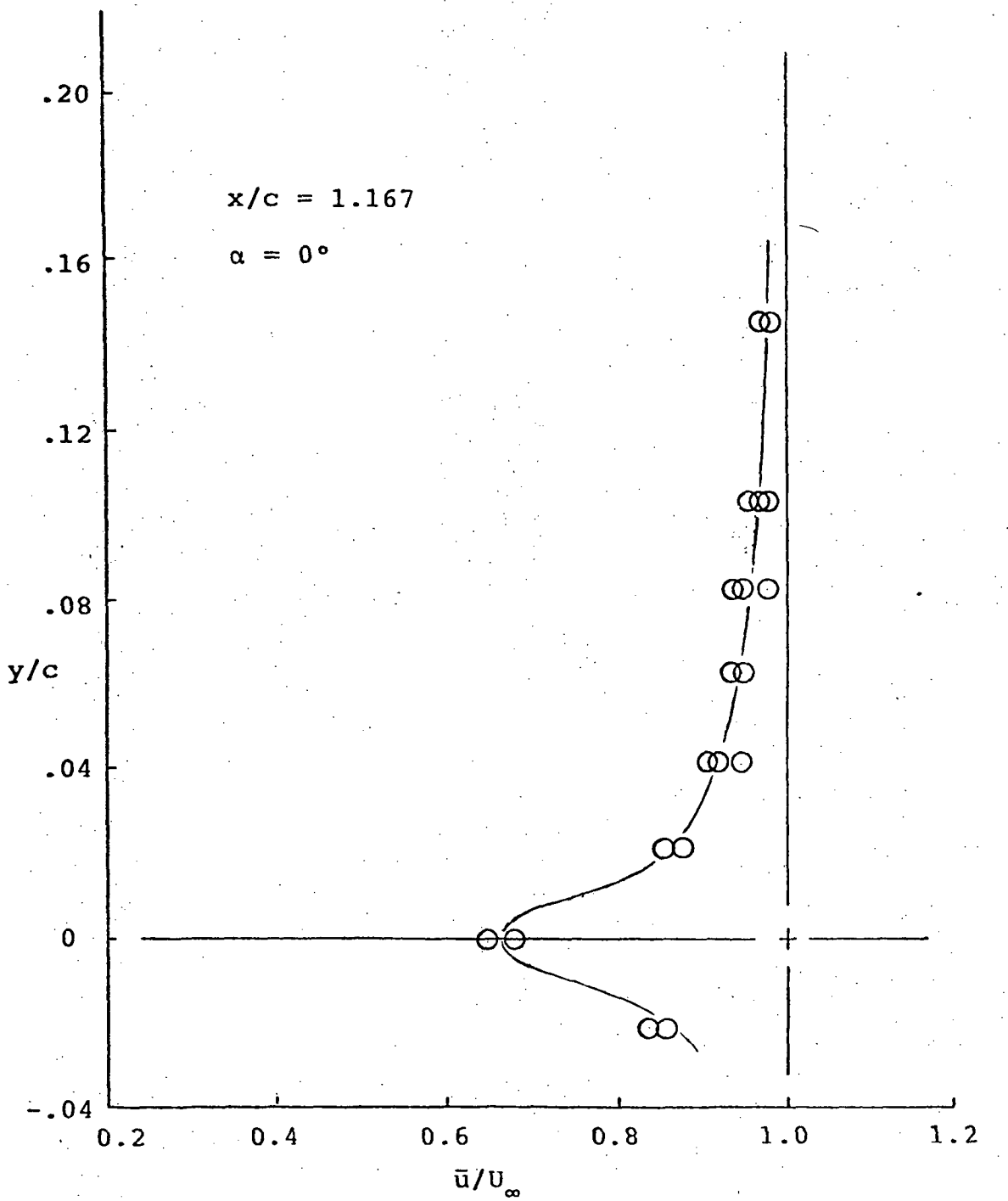

Figure 30. - Mean u Velocity Distributions;
x/c = 1.167; Attack Angle = 0 Degrees

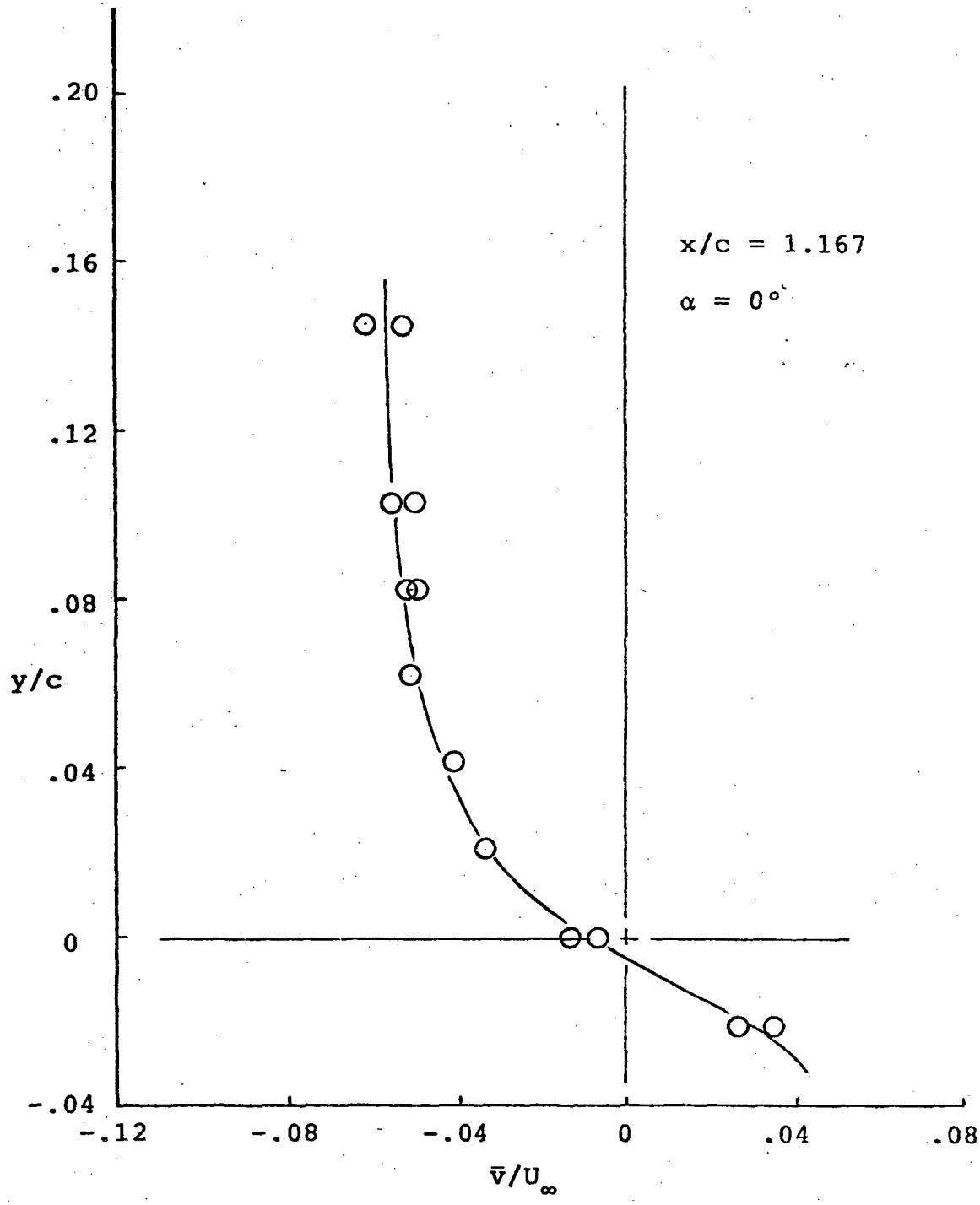

Figure 31. - Mean v Velocity Distributions;
x/c = 1.167; Attack Angle = 0 Degrees

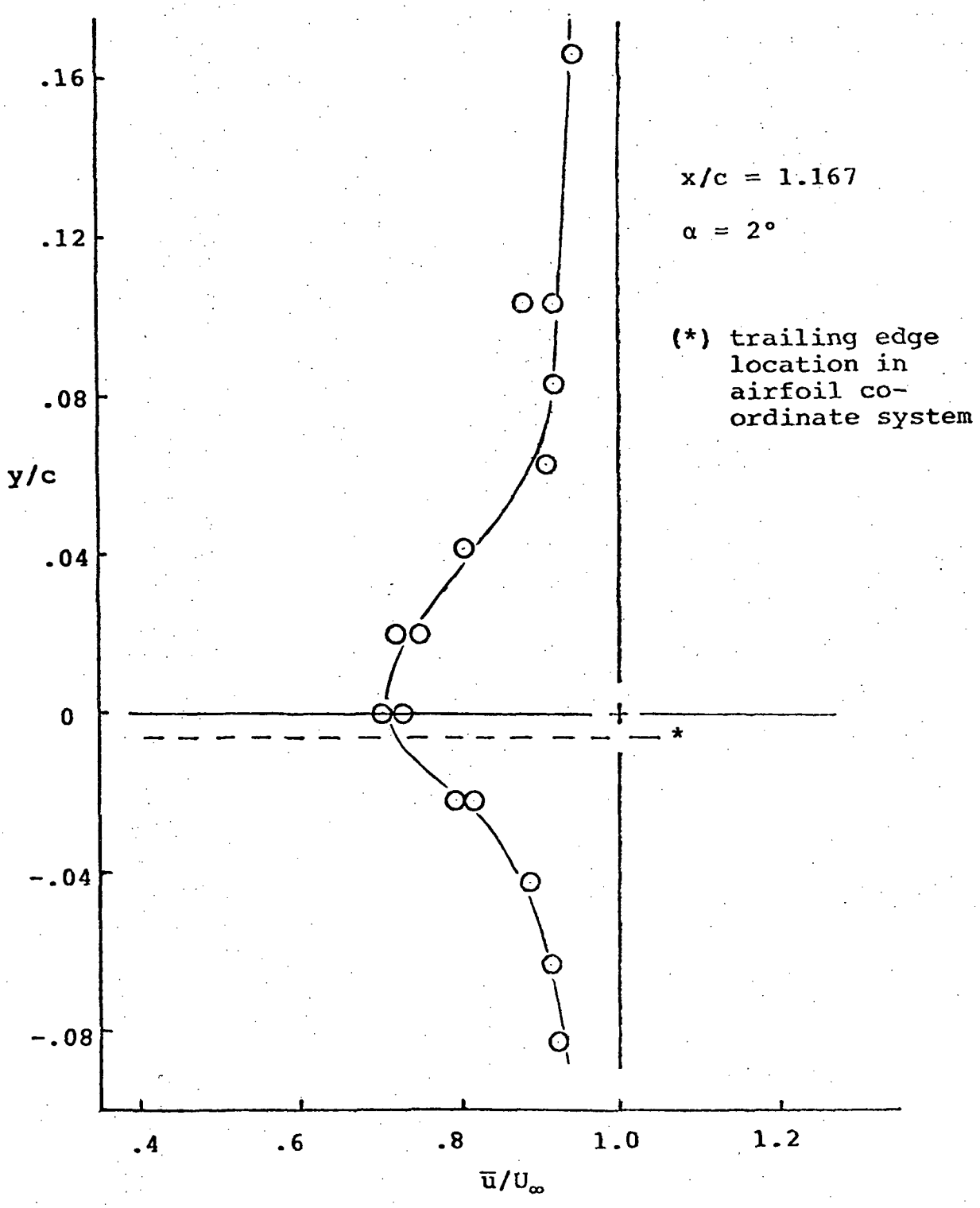

Figure 32. - Mean u Velocity Distributions; x/c = 1.167; Attack Angle = 2 Degrees

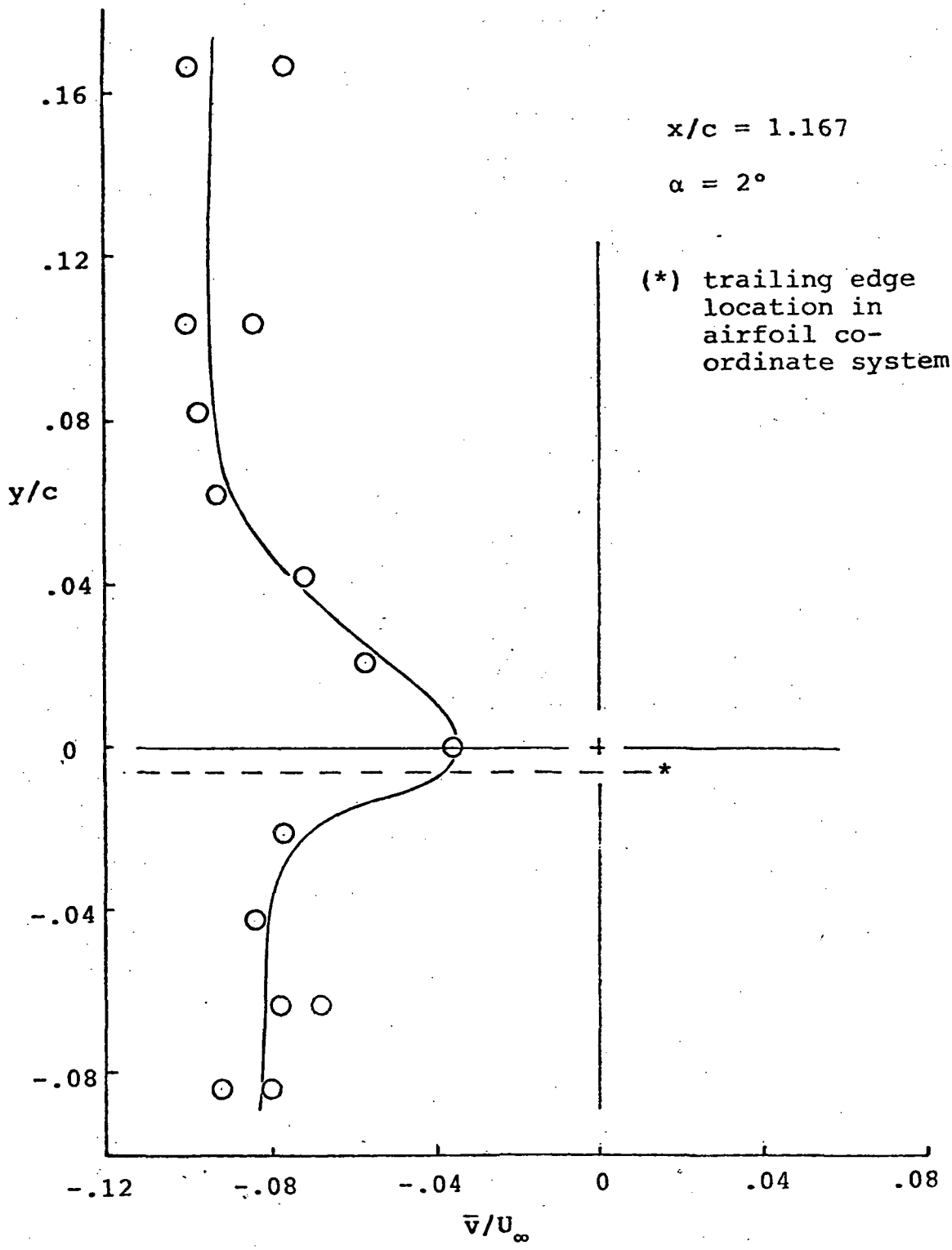

Figure 33. - Mean v Velocity Distributions; x/c = 1.167; Attack Angle = 2 Degrees

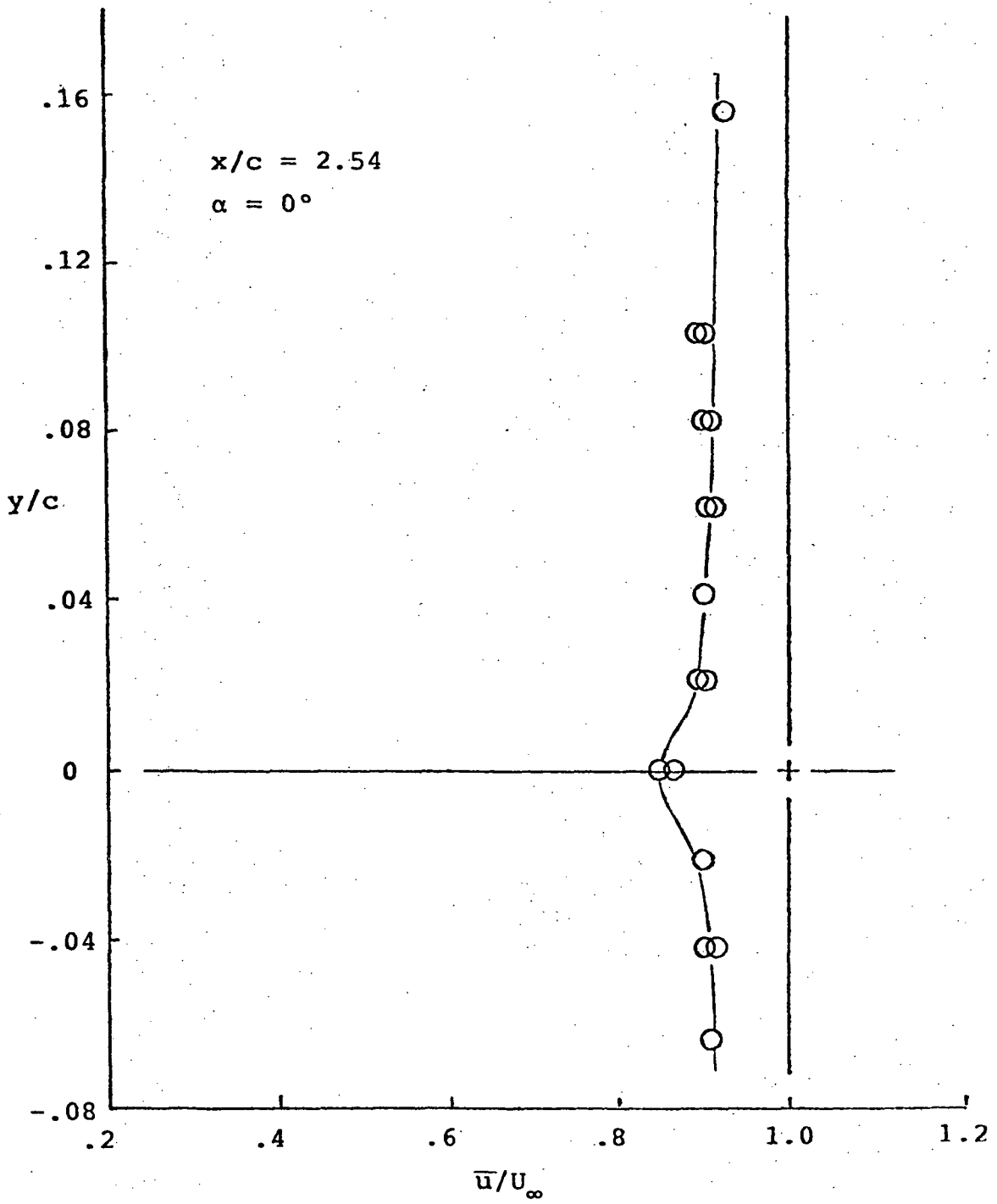

Figure 34. - Mean u Velocity Distributions;
x/c = 2.54; Attack Angle = 0 Degrees

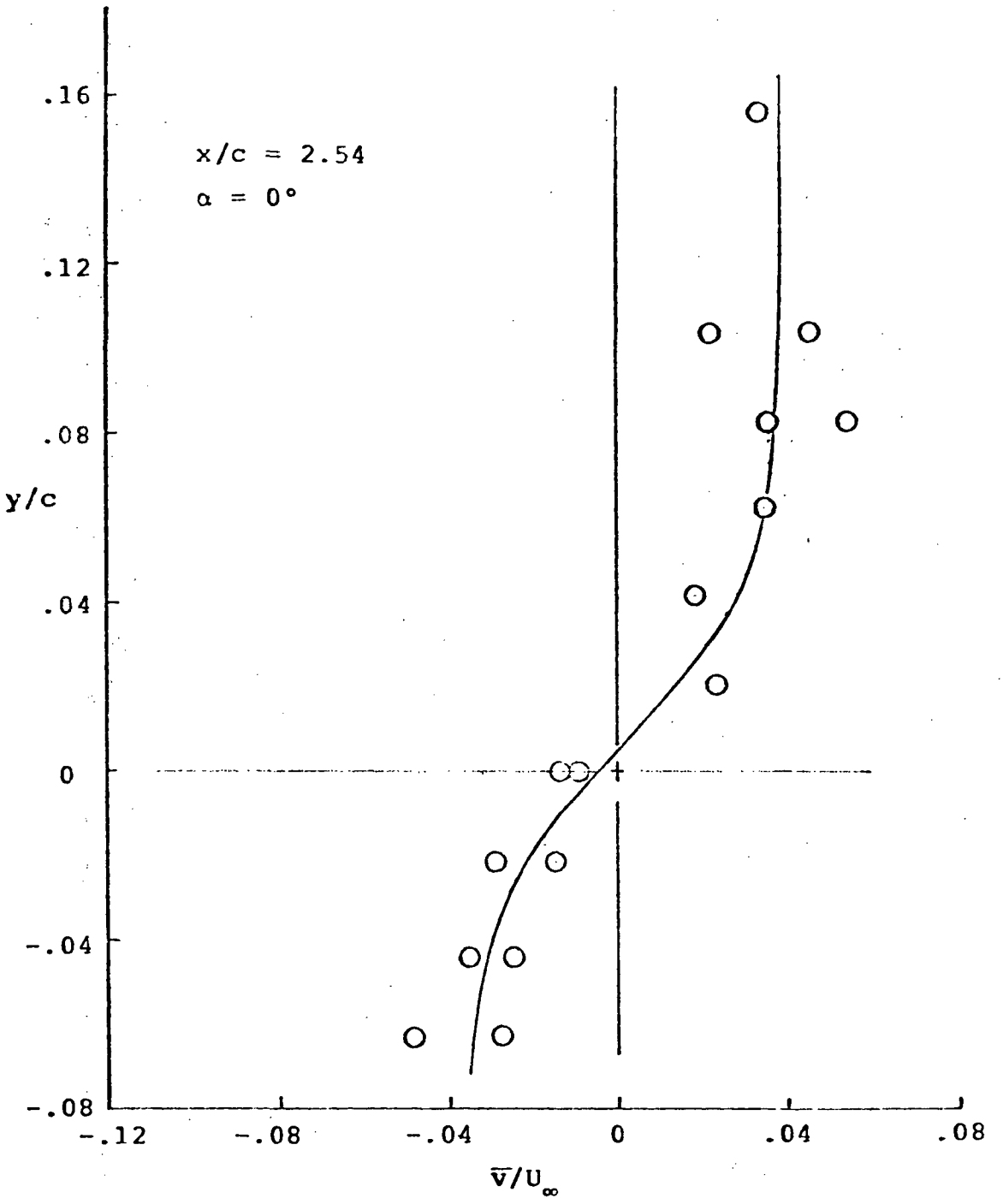

Figure 35. - Mean v Velocity Distributions;
x/c = 2.54; Attack Angle = 0 degrees

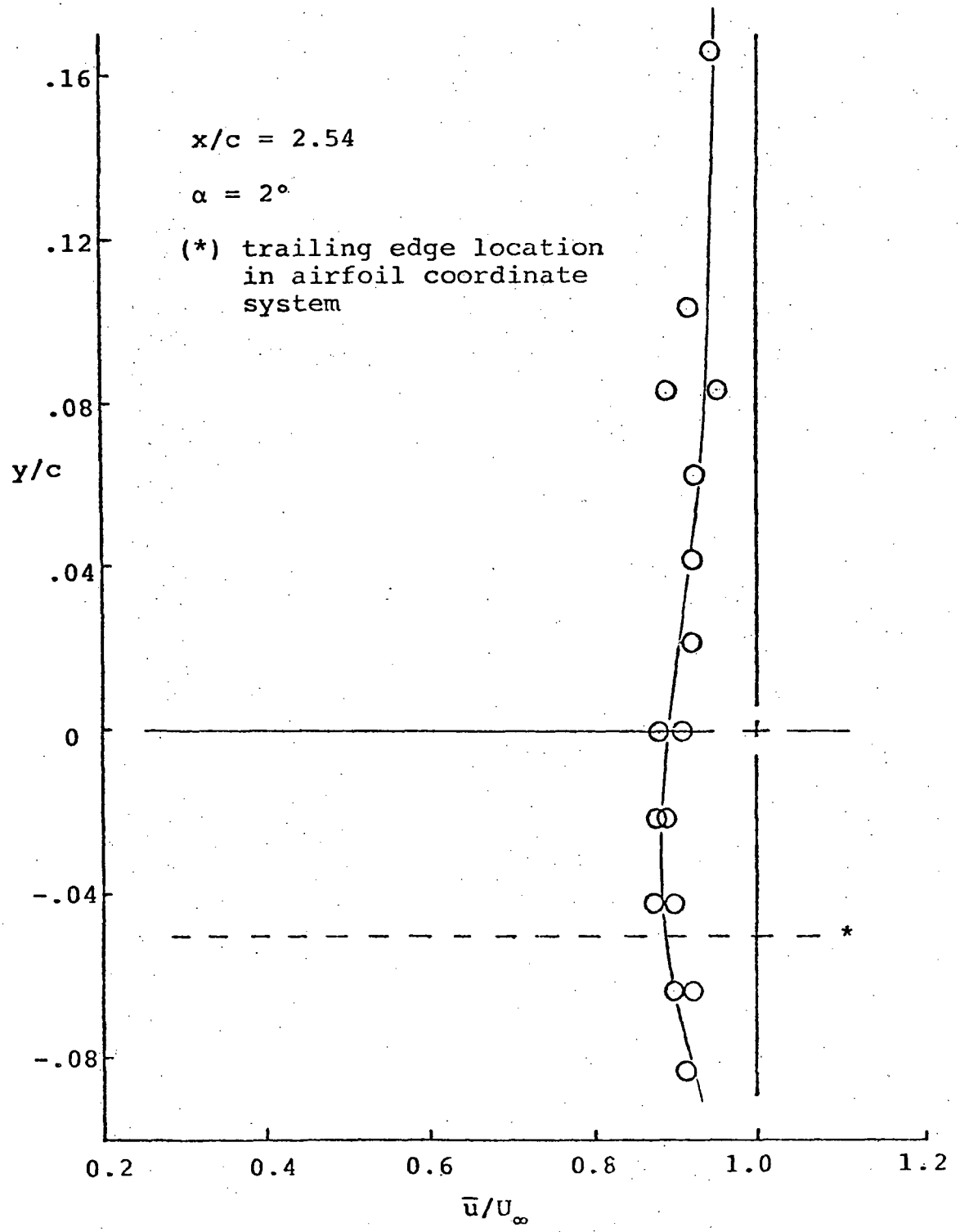

Figure 36. - Mean u Velocity Distributions; x/c = 2.54; Attack Angle = 2 Degrees

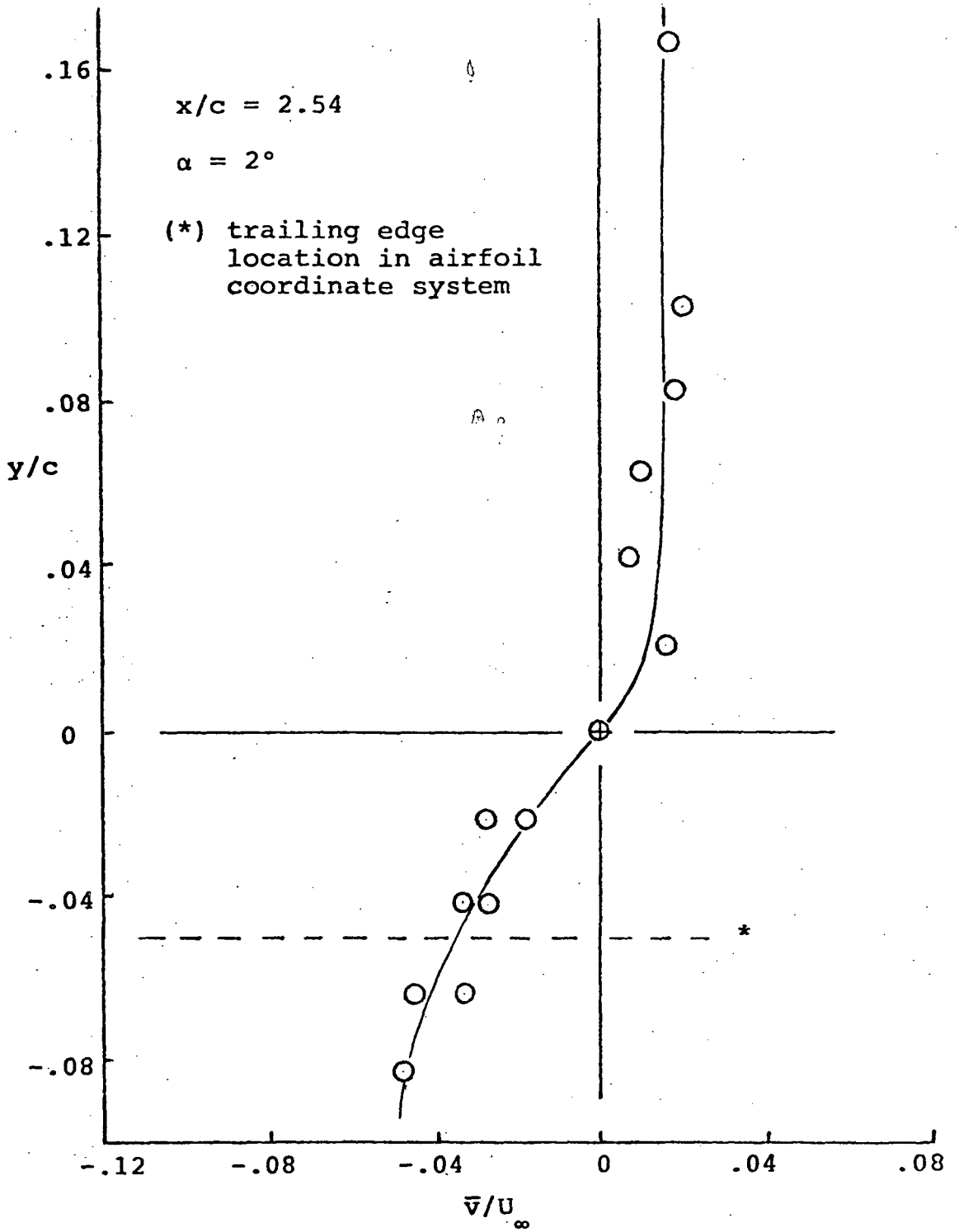

Figure 37. - Mean v Velocity Distributions; x/c = 2.54; Attack Angle = 2 Degrees

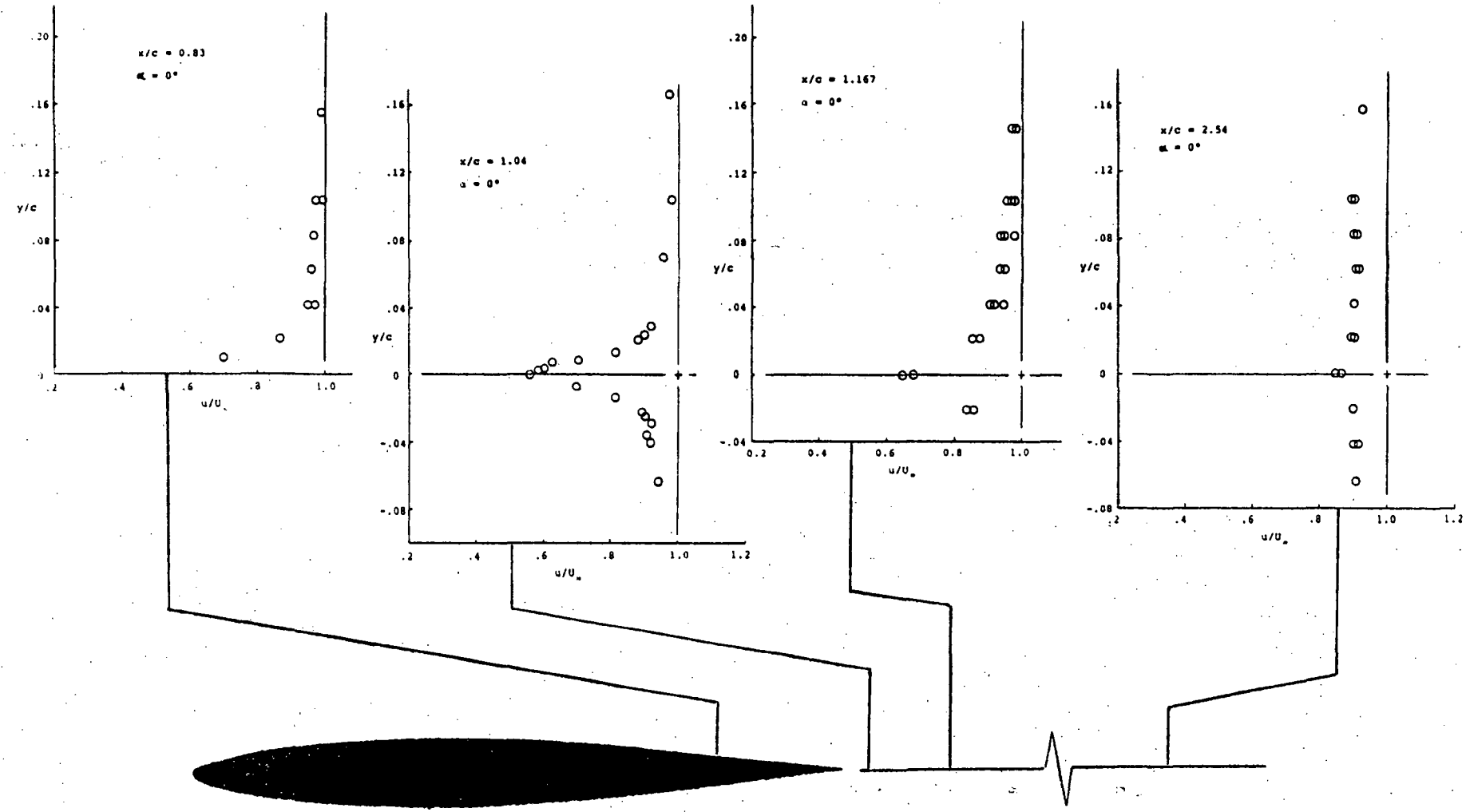

Figure 38. - Development of Mean u Velocity;
Attack Angle = 0 Degrees

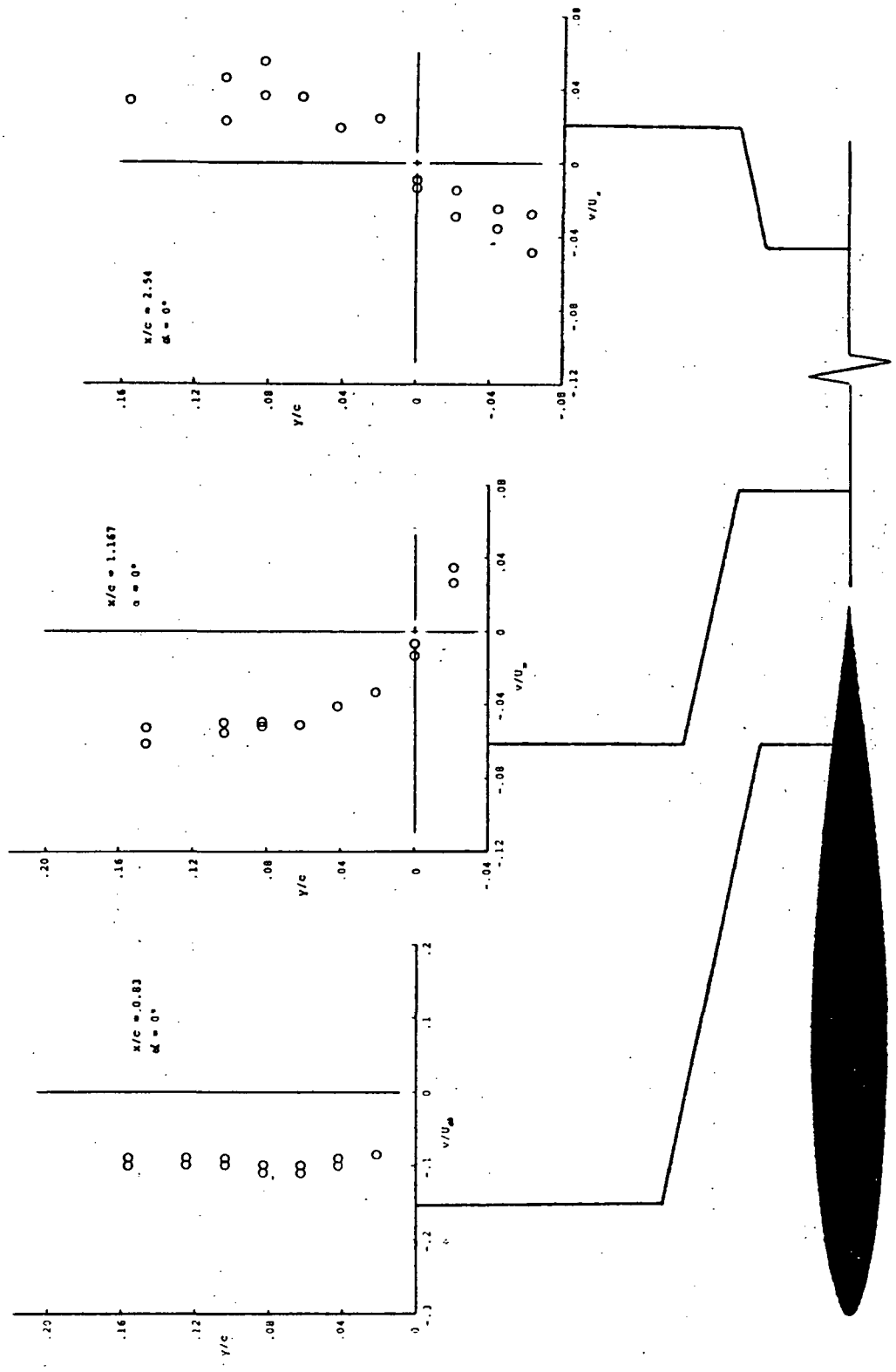

Figure 39. - Development of Mean v Velocity;
Attack Angle = 0 Degrees

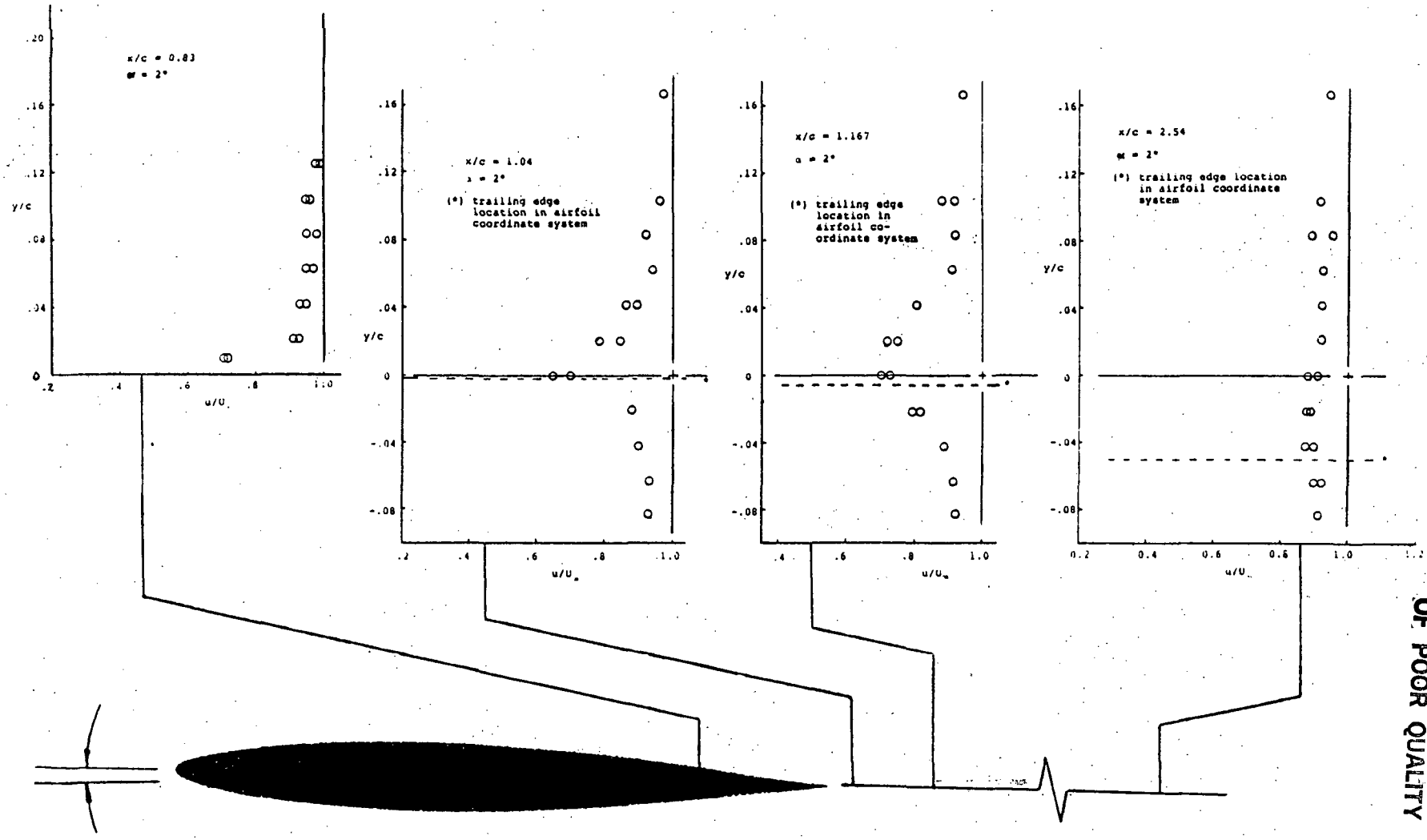

Figure 40. - Development of Mean u Velocity;
Attack Angle = 2 Degrees

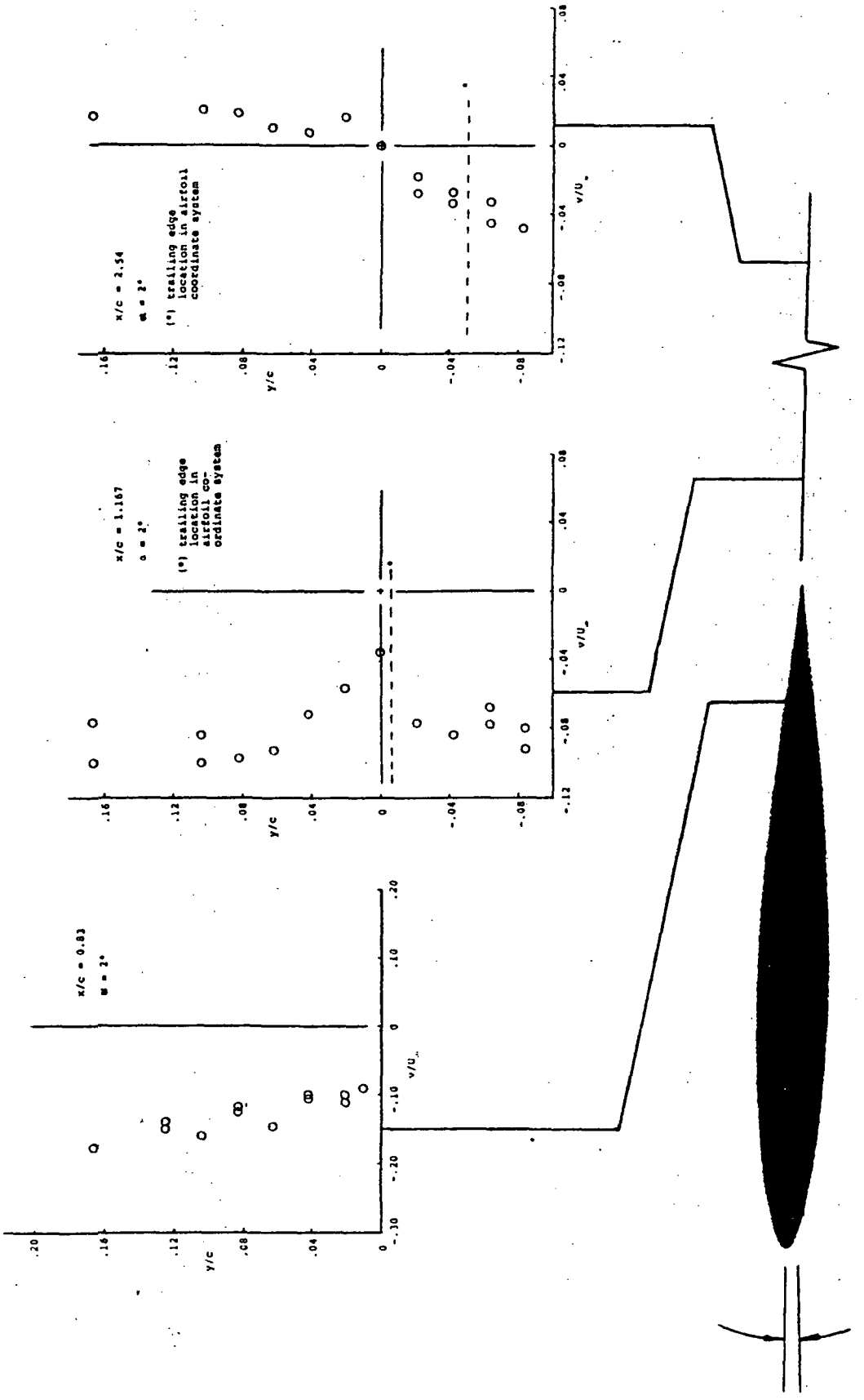

Figure 41. - Development of Mean v Velocity; Attack Angle = 2 Degrees

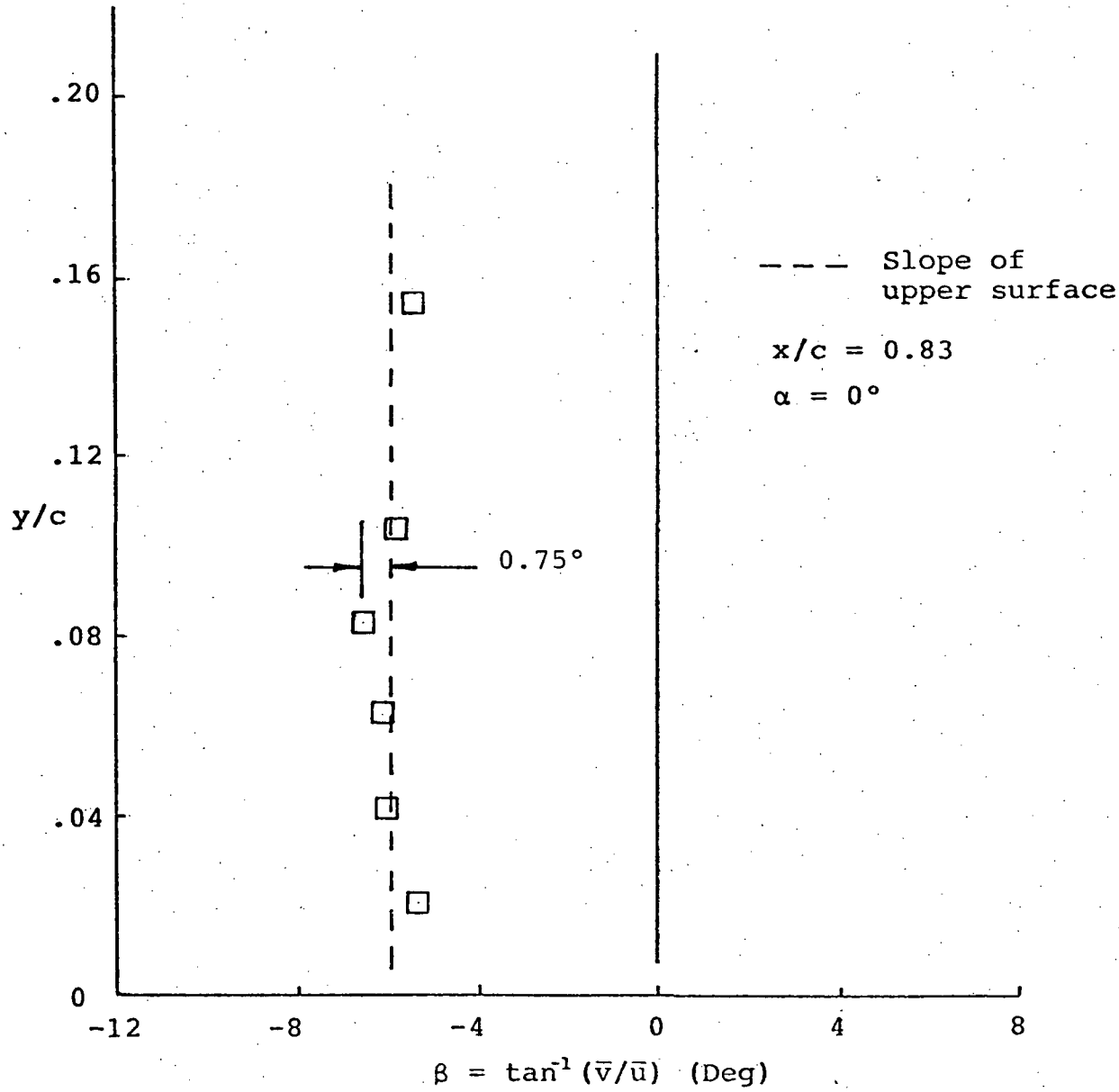

Figure 42. - Local Flow Angle;
x/c = 0.83; Attack Angle = 0 Degrees

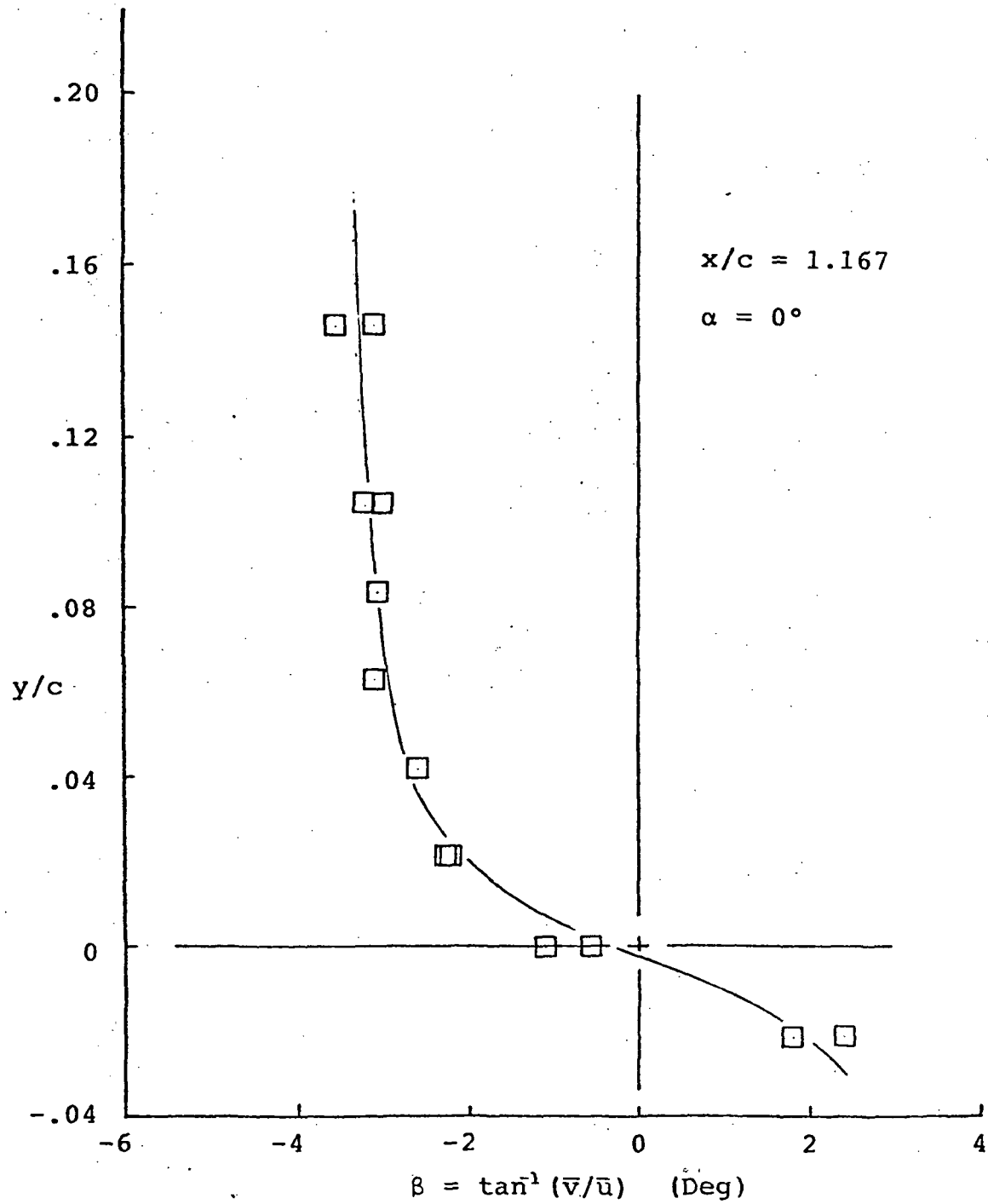

Figure 43. - Local Flow Angle;
x/c = 1.167; Attack Angle = 0 Degrees

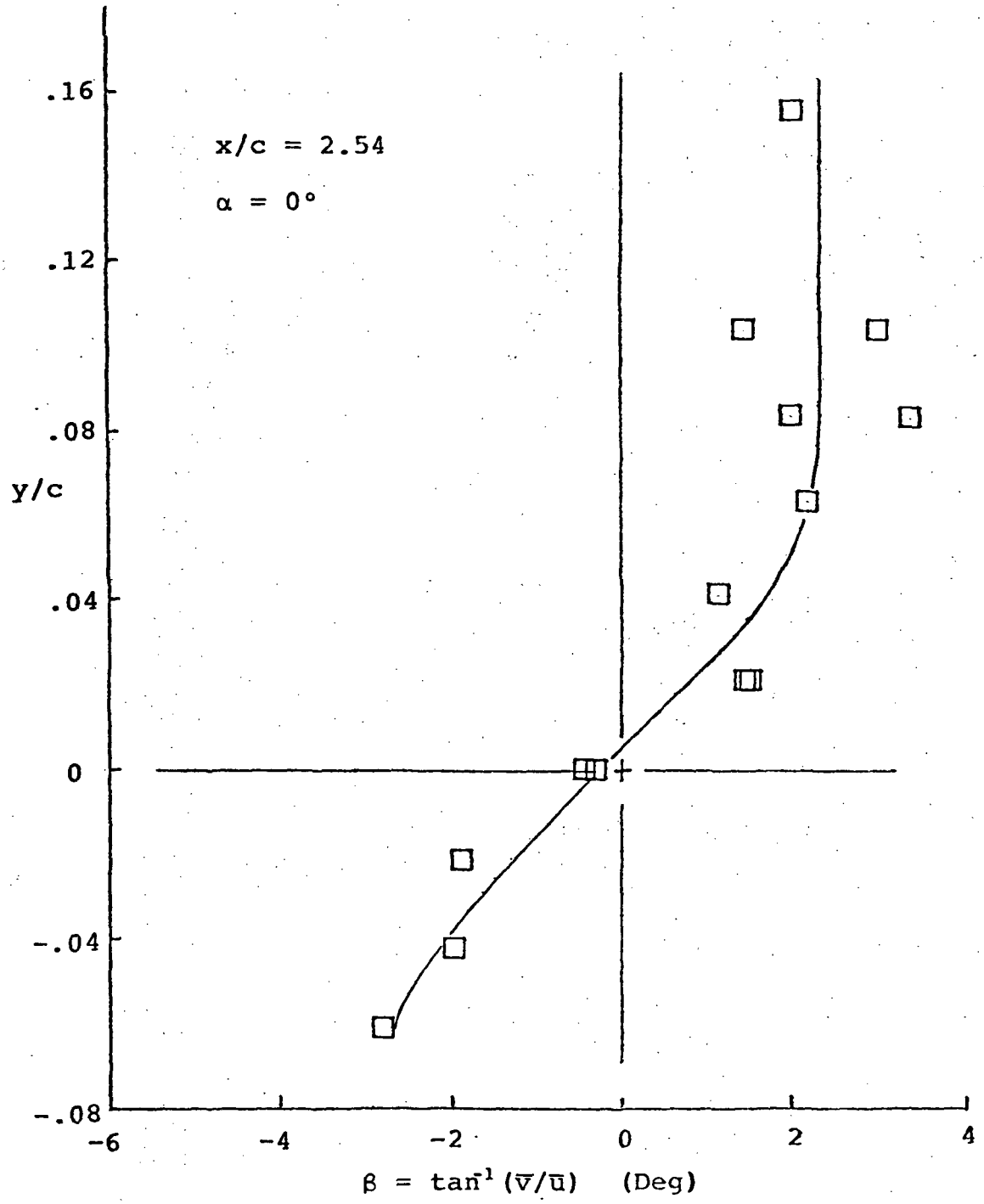

Figure 44. - Local Flow Angle;
x/c = 2.54; Attack Angle = 0 Degrees

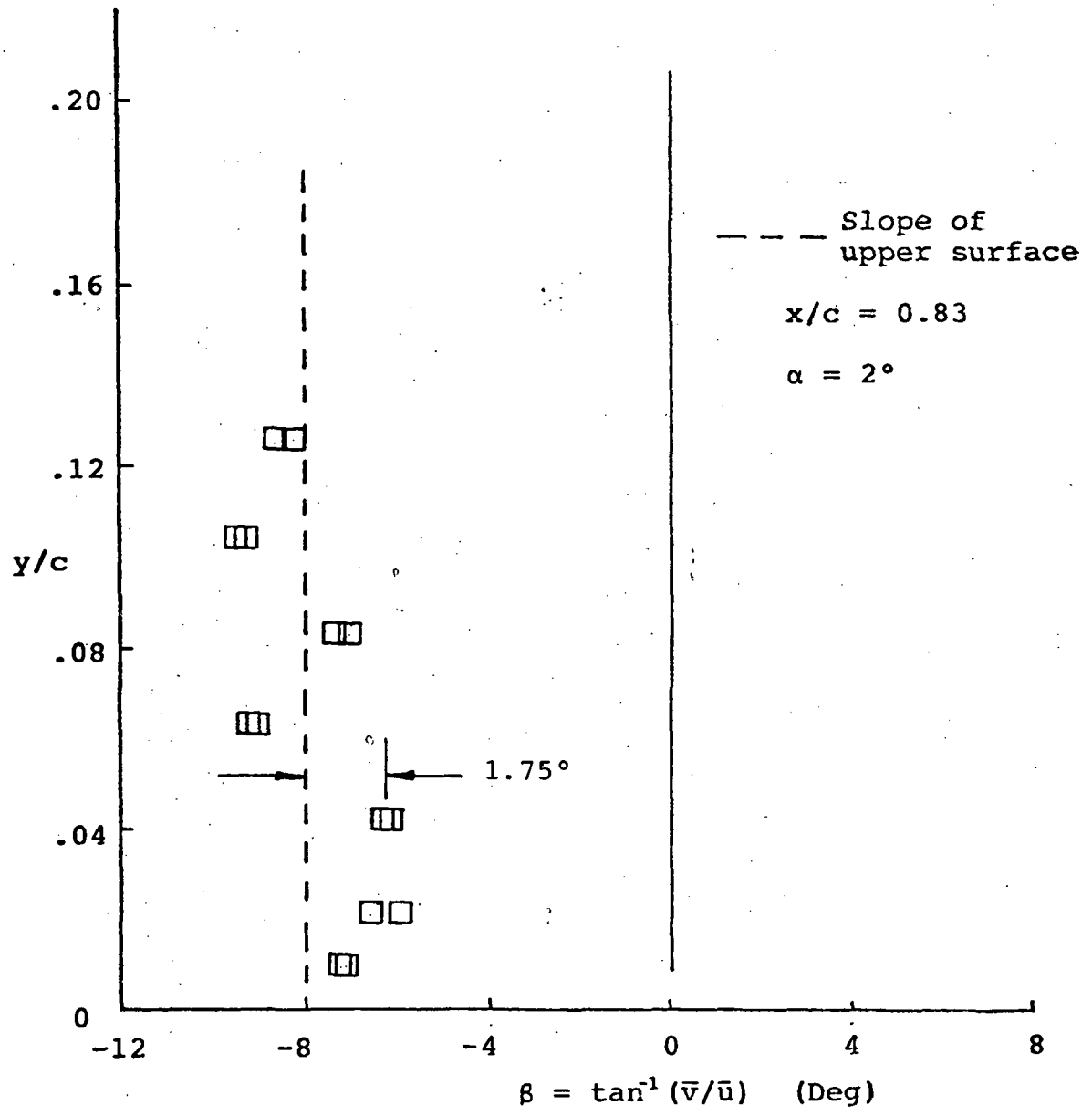

Figure 45. - Local Flow Angle;
x/c = 0.83; Attack Angle = 2 Degrees

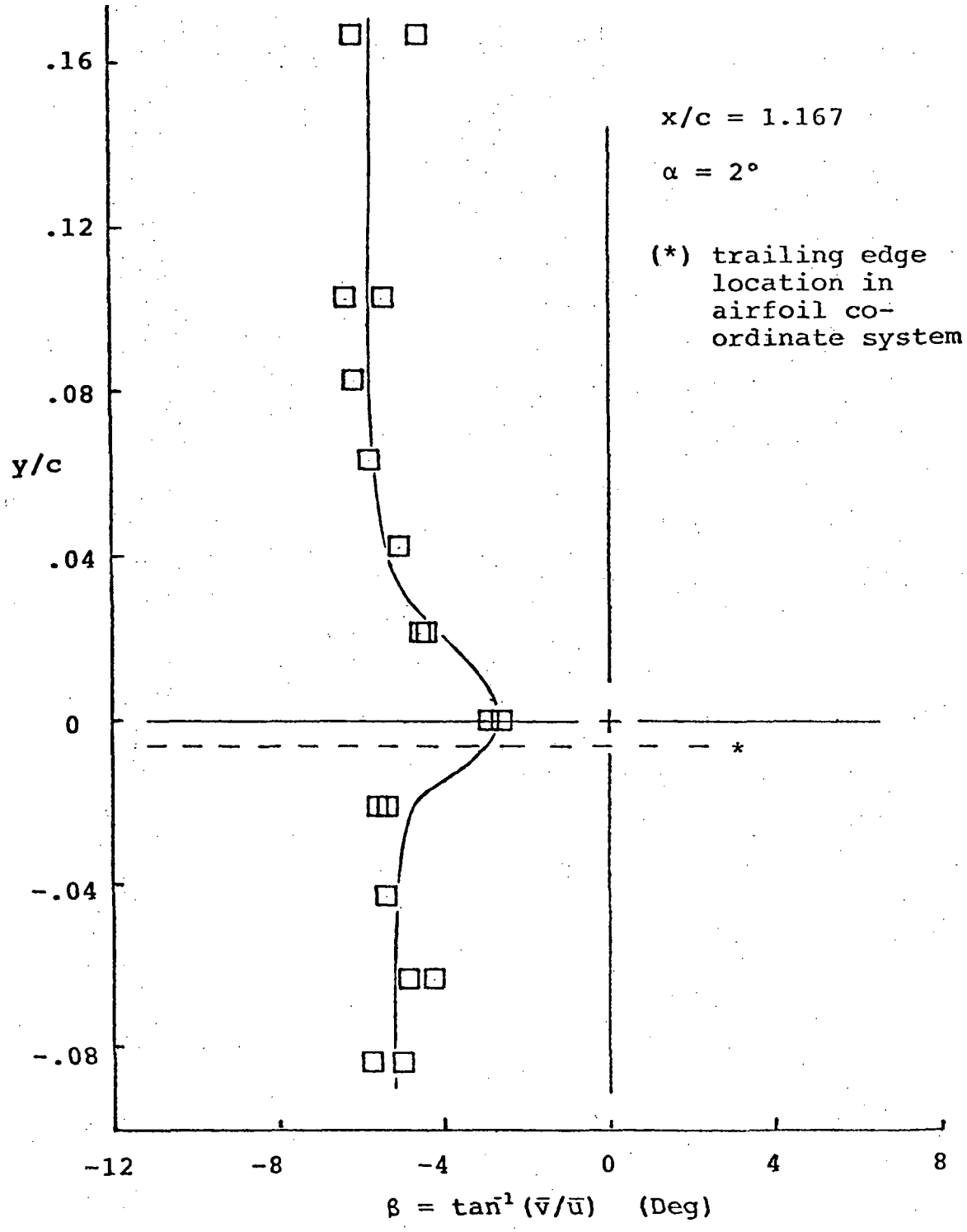

Figure 46. - Local Flow Angle;
x/c = 1.167; Attack Angle = 2 Degrees

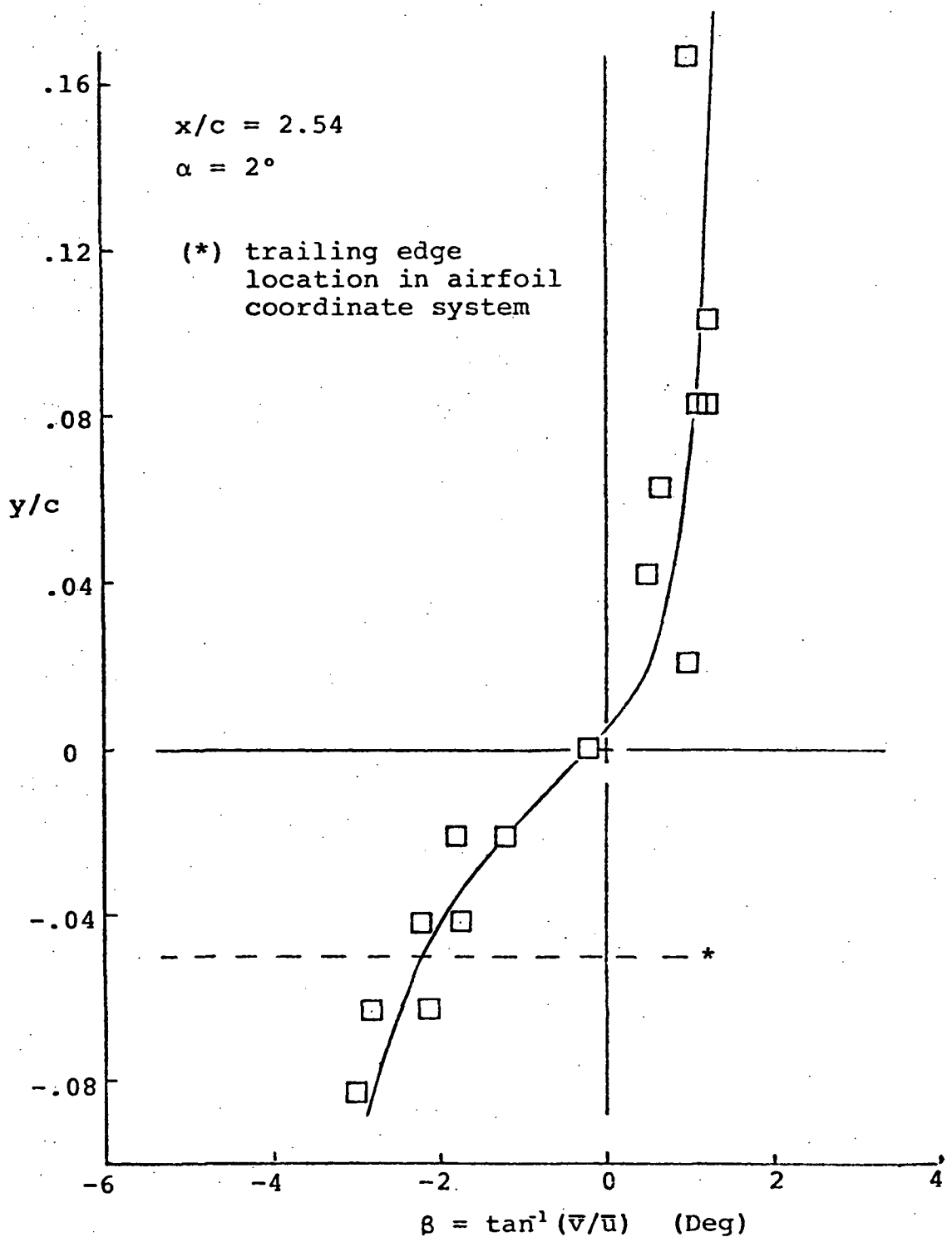

Figure 47. - Local Flow Angle;
x/c = 2.54; Attack Angle = 2 Degrees

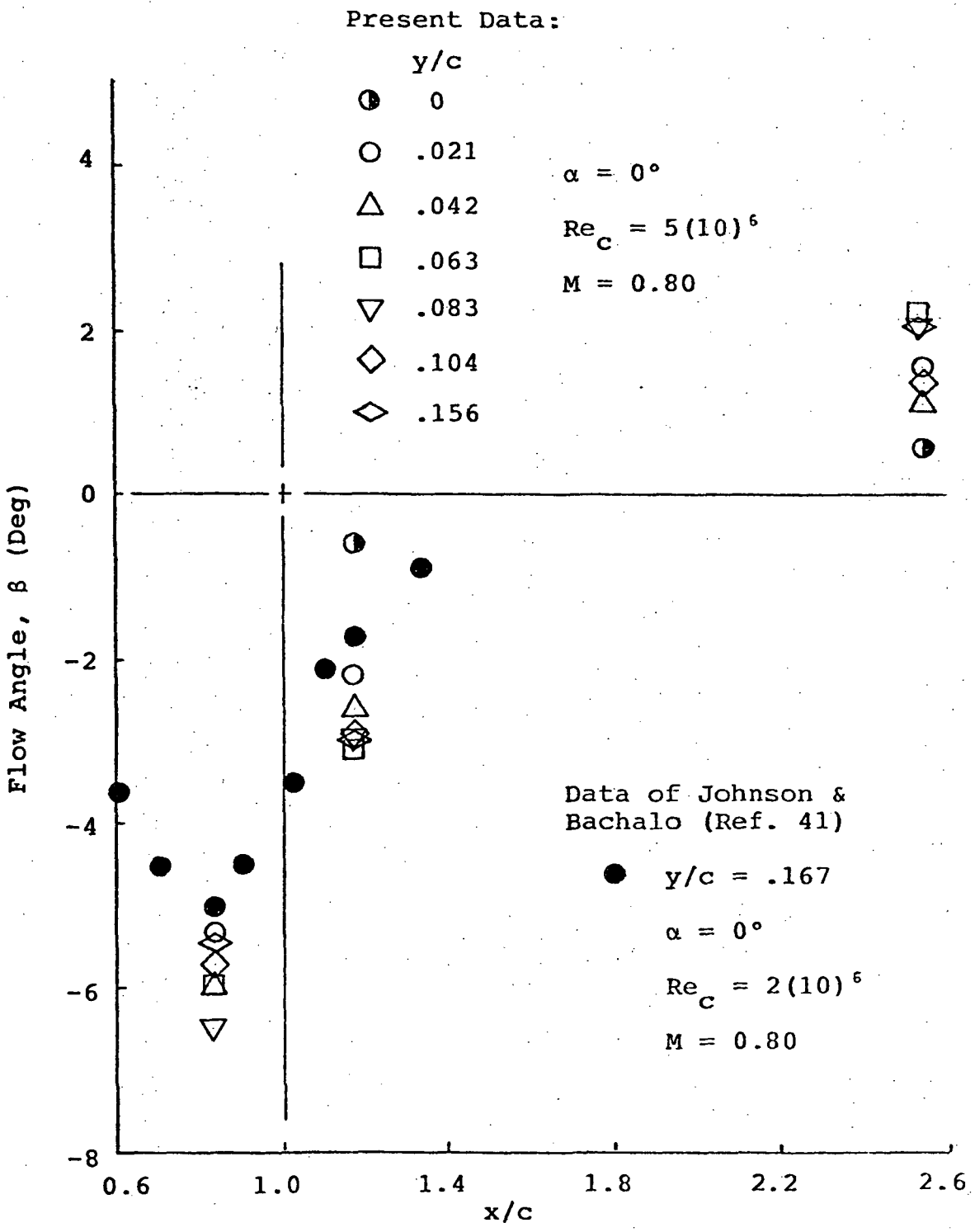

Figure 48. - Local Flow Angle Comparisons; Attack Angle = 0 Degrees

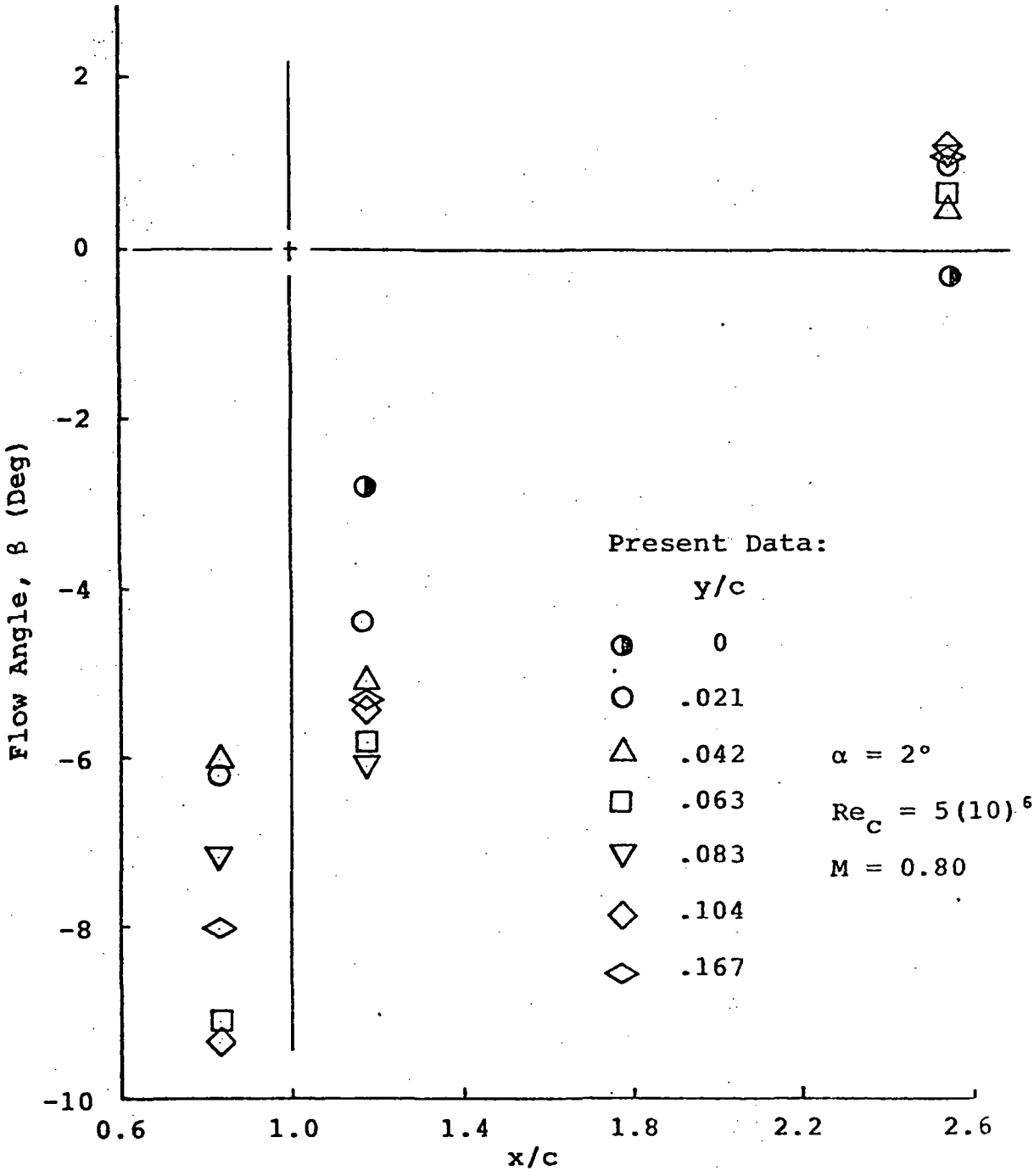

Figure 49. - Local Flow Angle Comparisons;
Attack Angle = 2 Degrees

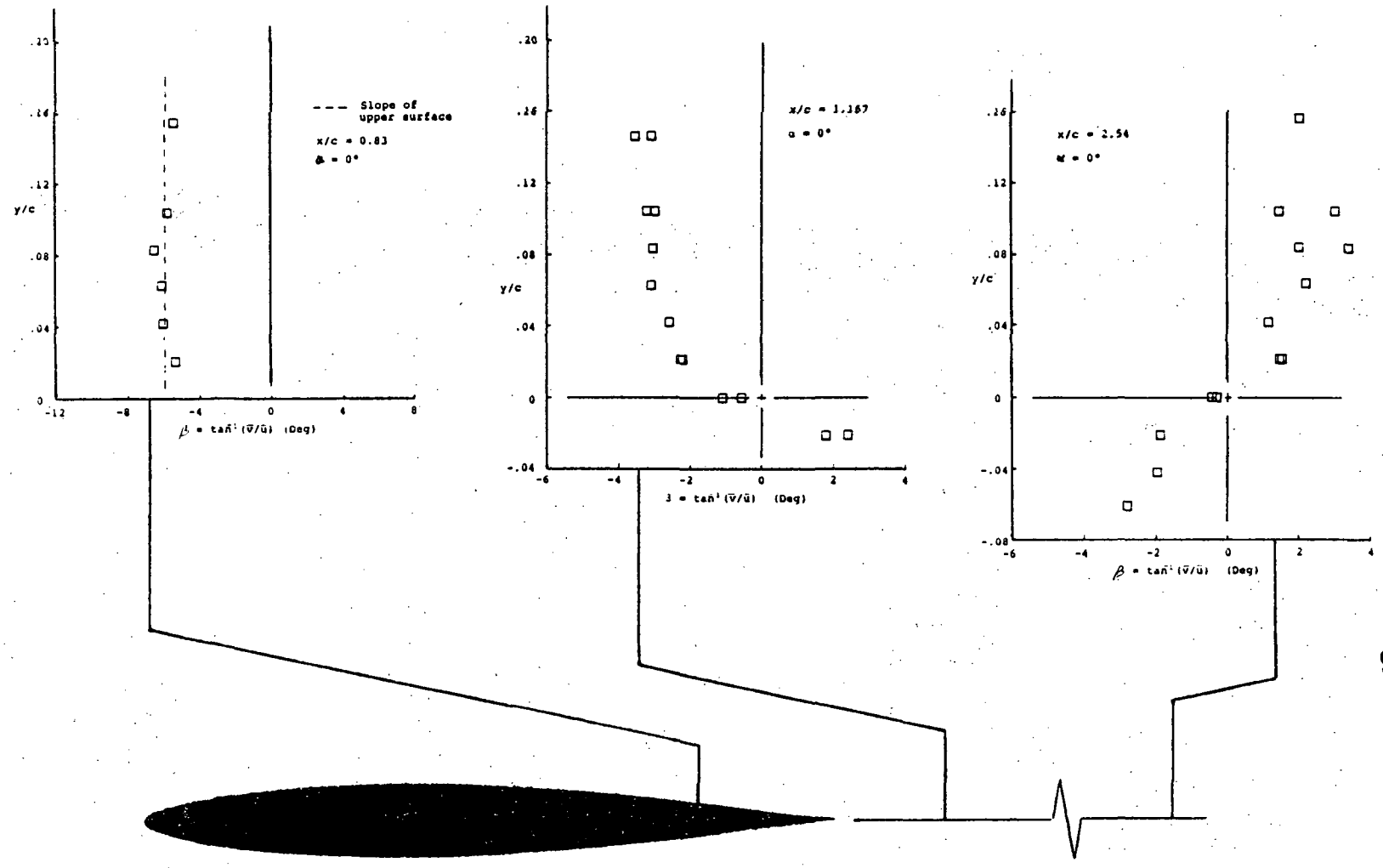

Figure 50. - Development of Local Flow Angle;
Attack Angle = 0 Degrees

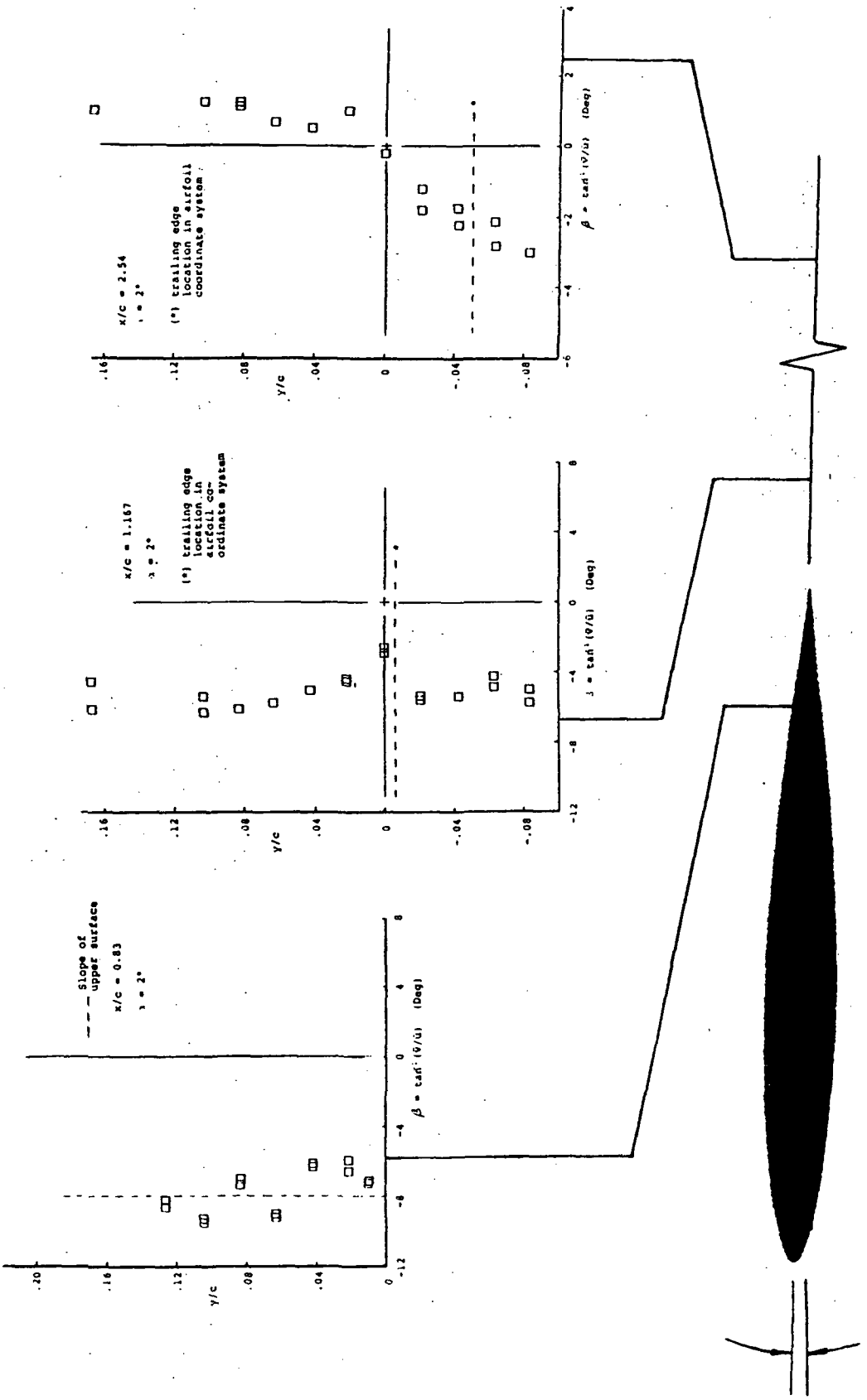

Figure 51. - Development of Local Flow Angle; Attack Angle = 2 Degrees

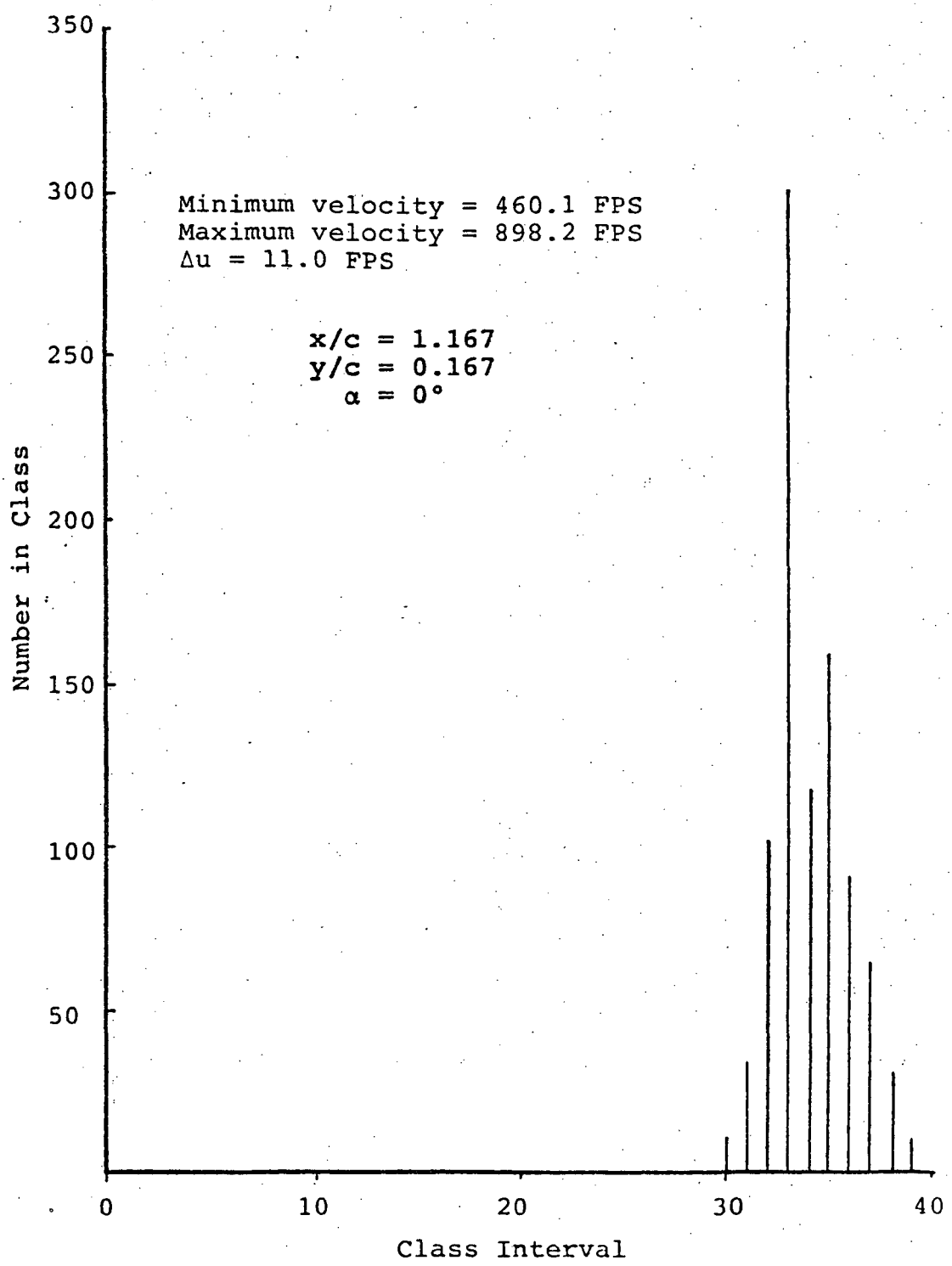

Figure 52. - u Velocity Histogram; x/c = 1.167; y/c = 0; Attack Angle = 0 Degrees

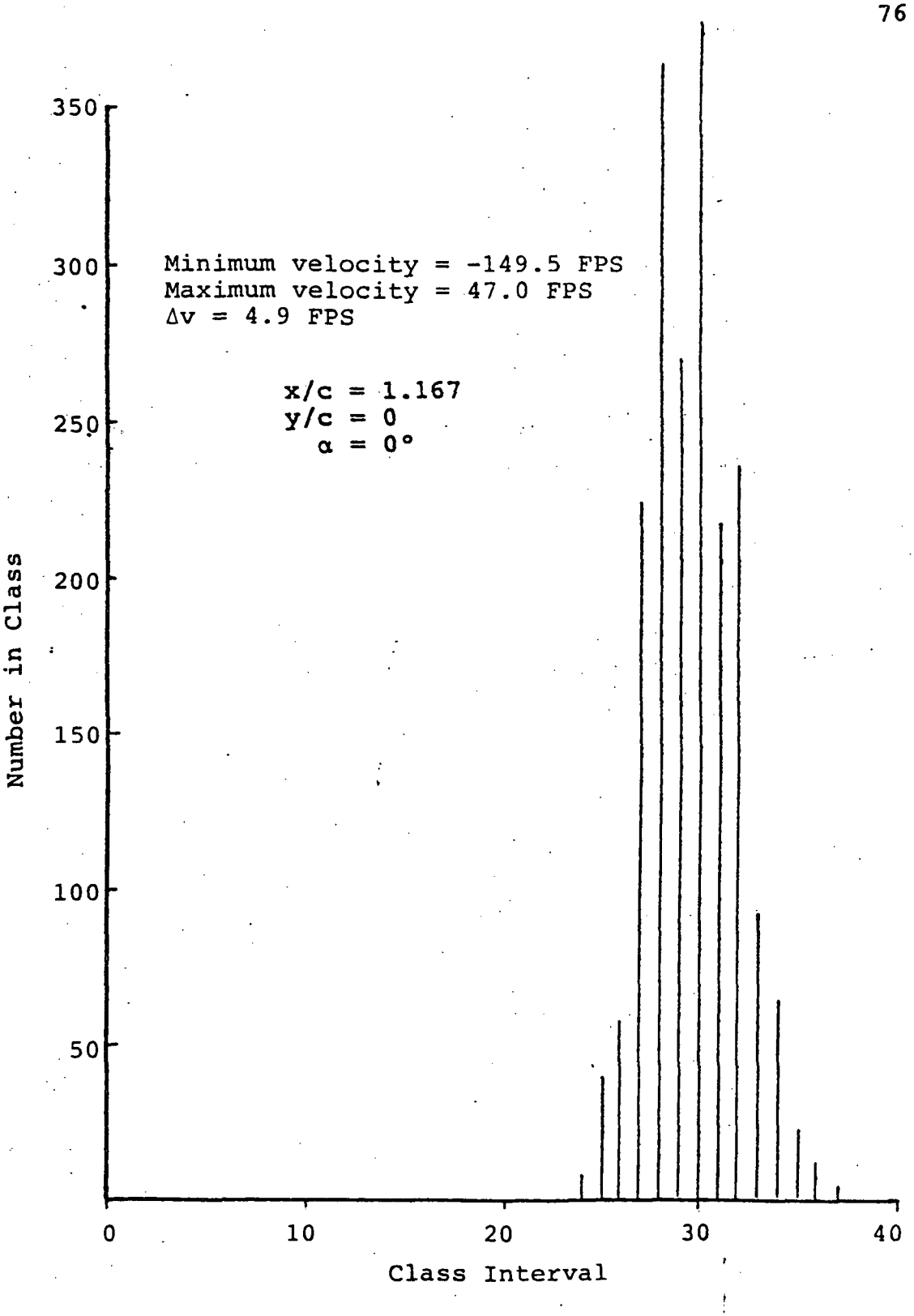

Figure 53. - v Velocity Histogram; x/c = 1.167; y/c = 0; Attack Angle = 0 Degrees

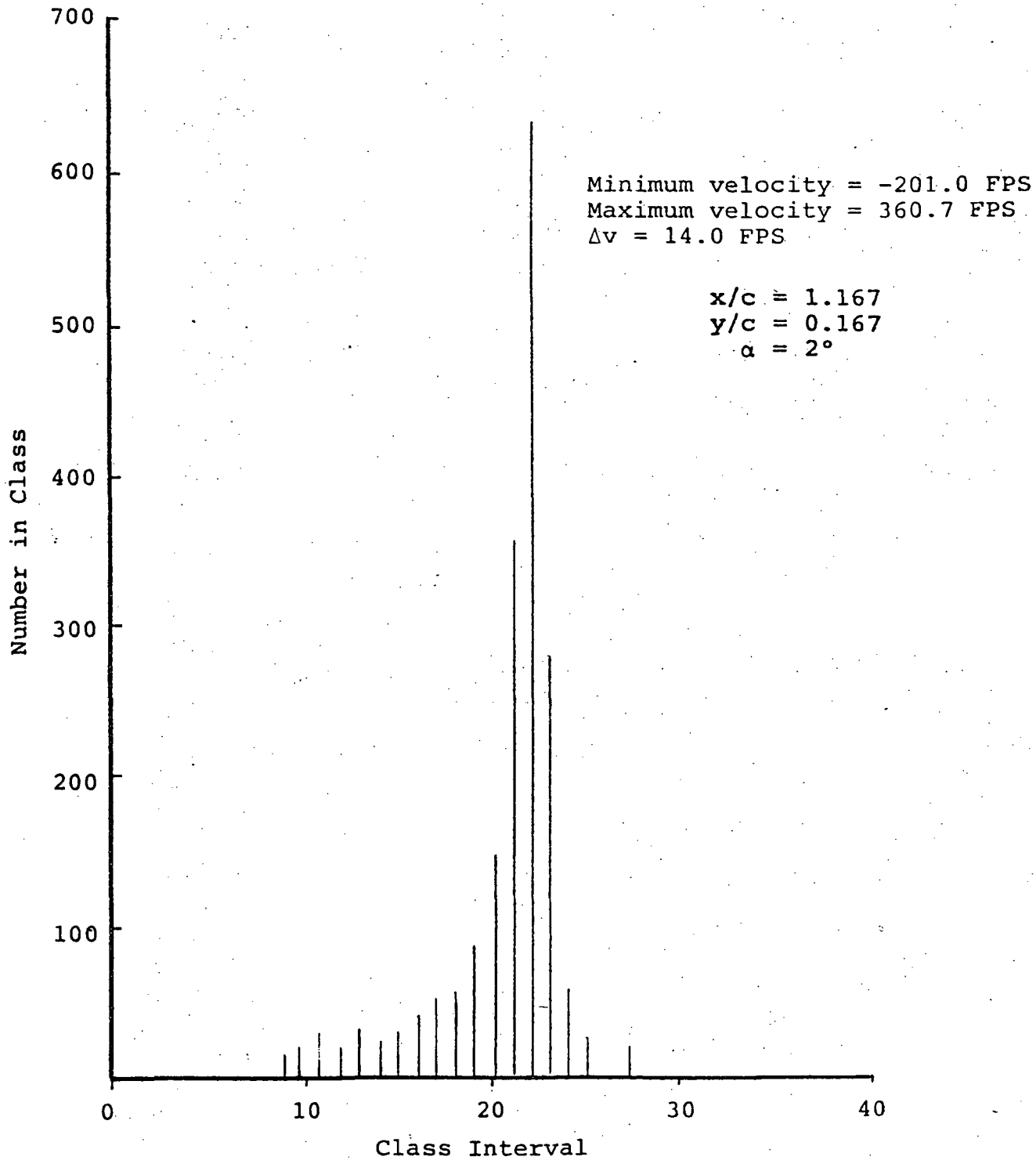

Figure 54. - v Velocity Histogram; x/c = 1.167; y/c = 0; Attack Angle = 2 Degrees

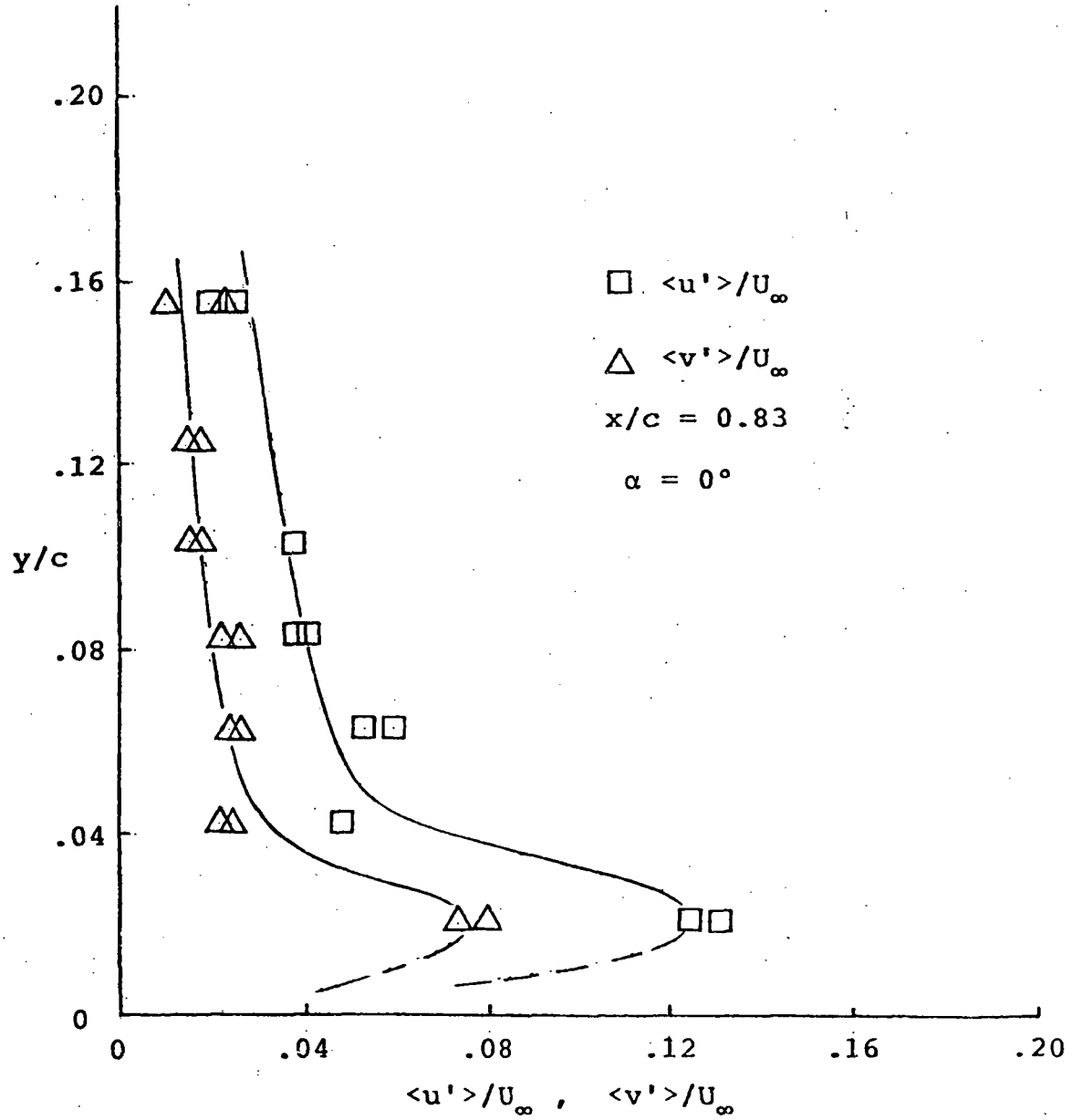

Figure 55. - Turbulence Intensity Distributions; x/c = 0.83; Attack Angle = 0 Degrees

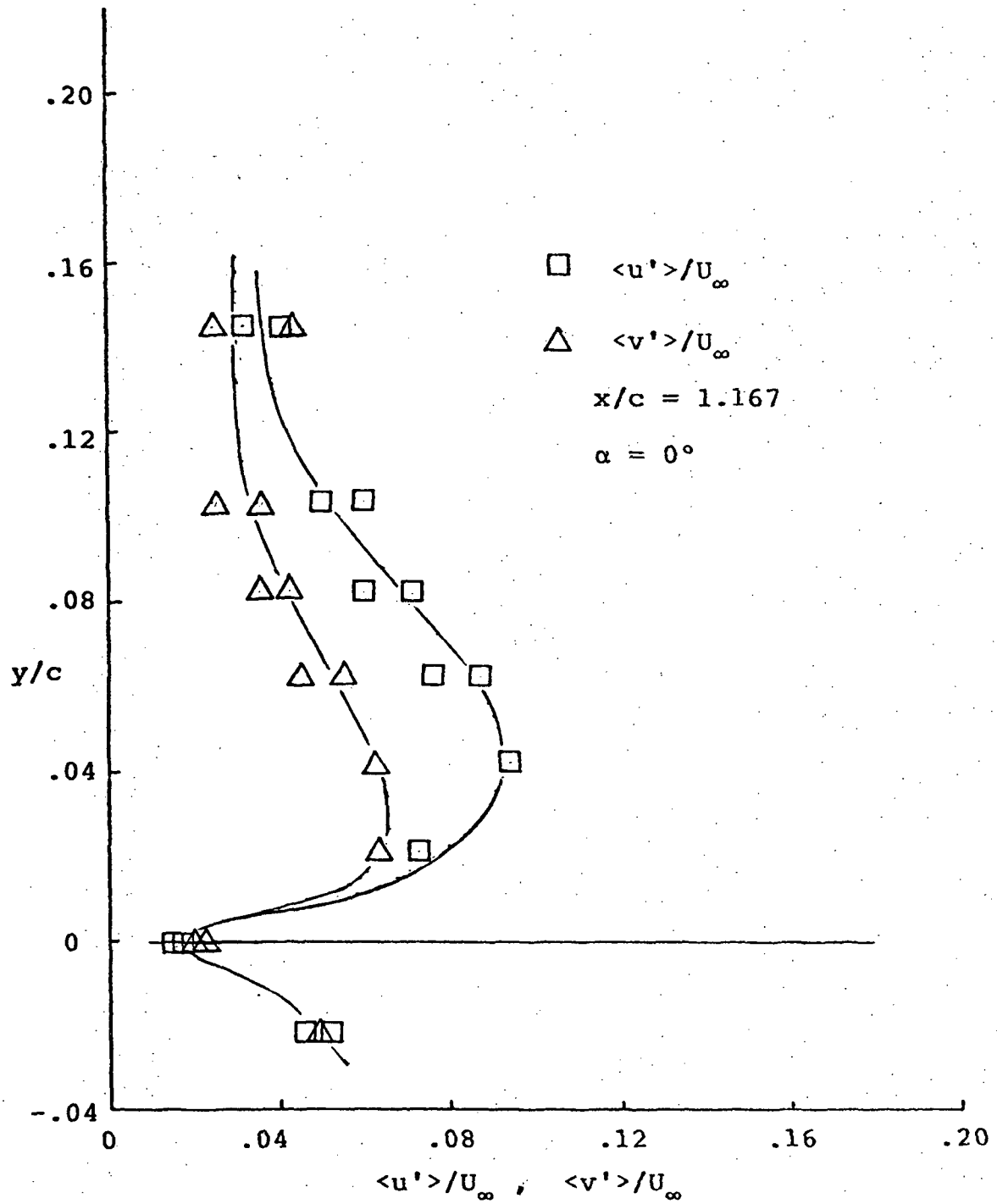

Figure 56. - Turbulence Intensity Distributions;
x/c = 1.167; Attack Angle = 0 Degrees

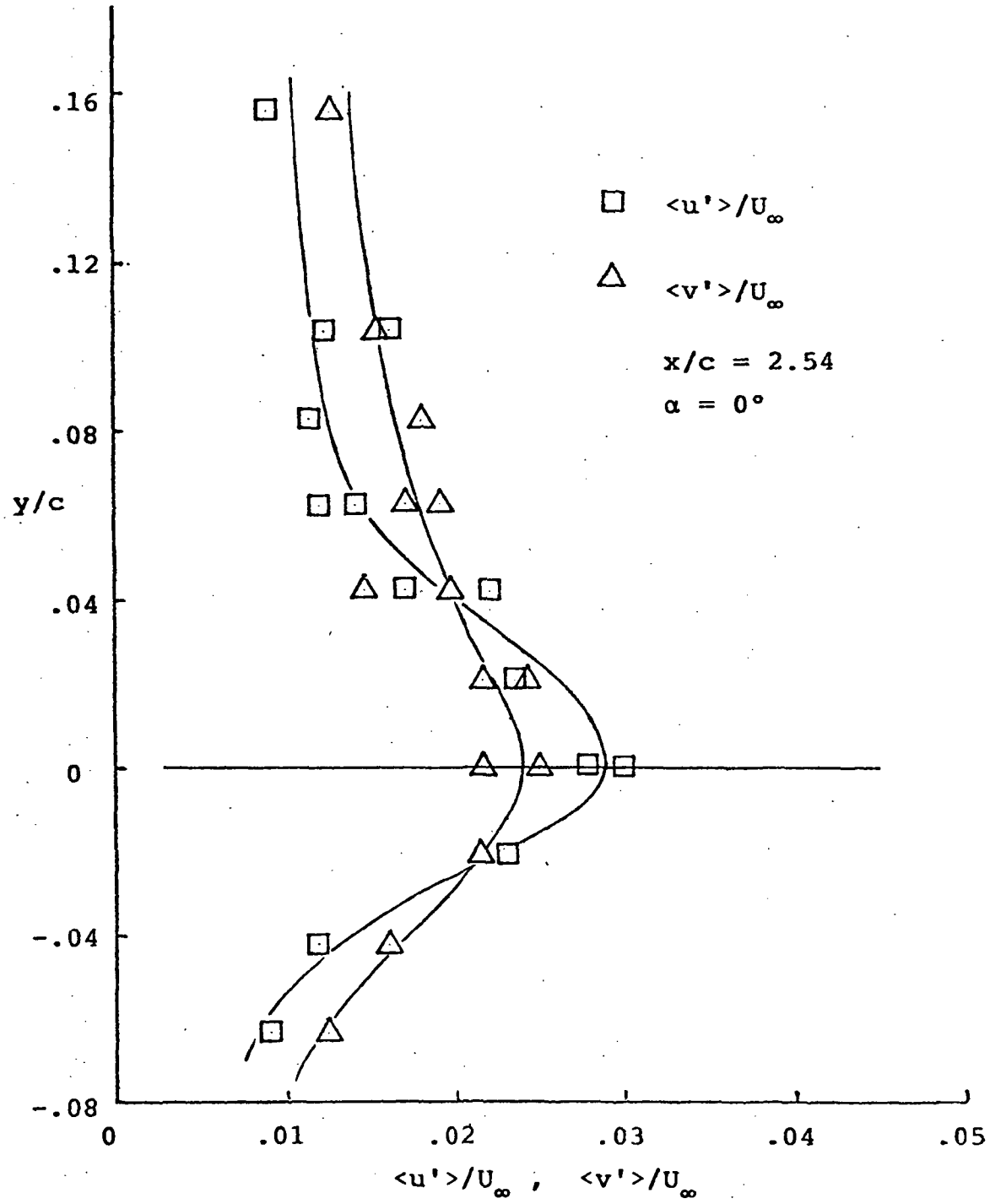

Figure 57. - Turbulence Intensity Distributions; x/c = 2.54; Attack Angle = 0 Degrees

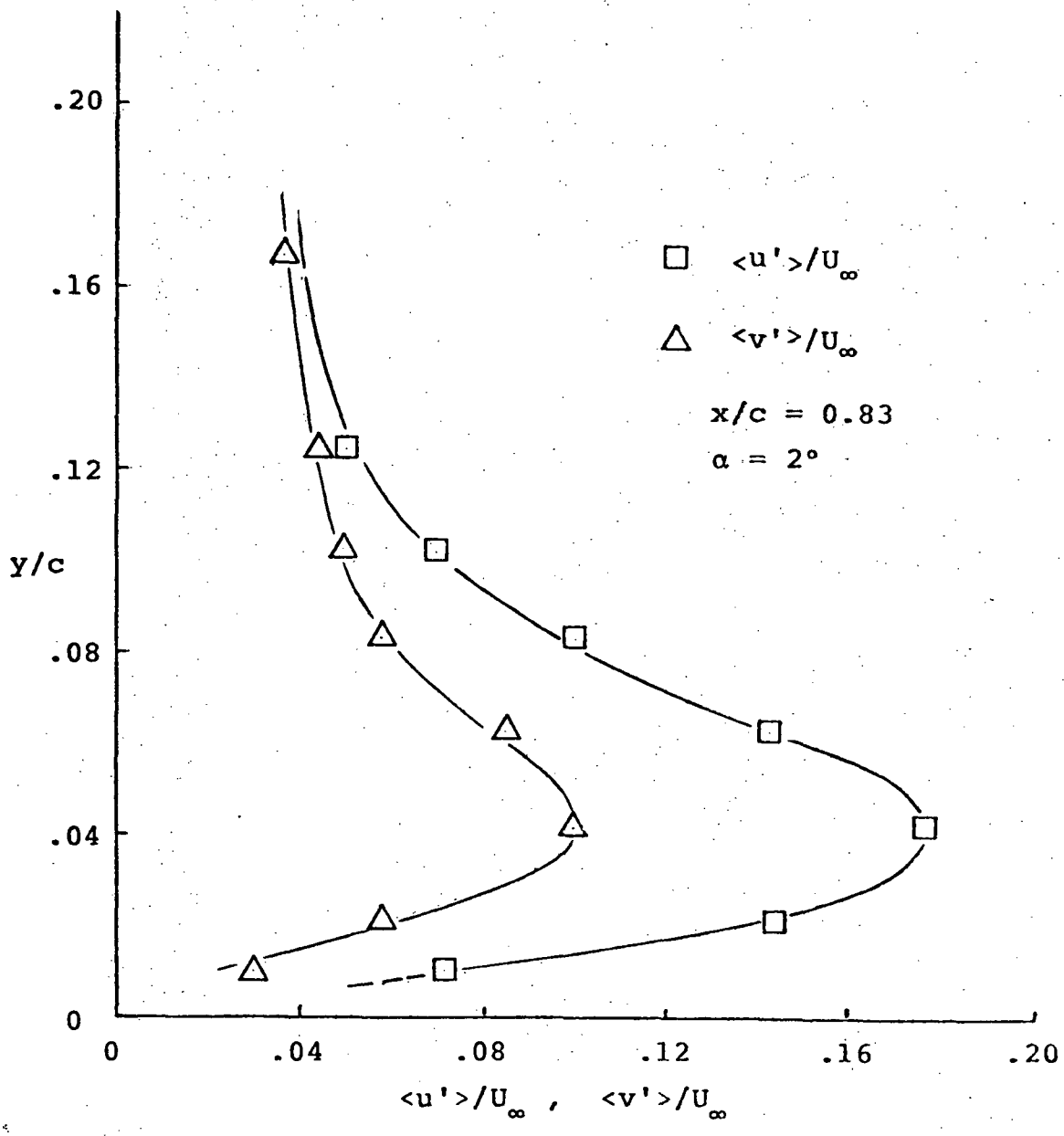

Figure 58. - Turbulent Intensity Distributions;
x/c = 0.83; Attack Angle = 2 Degrees

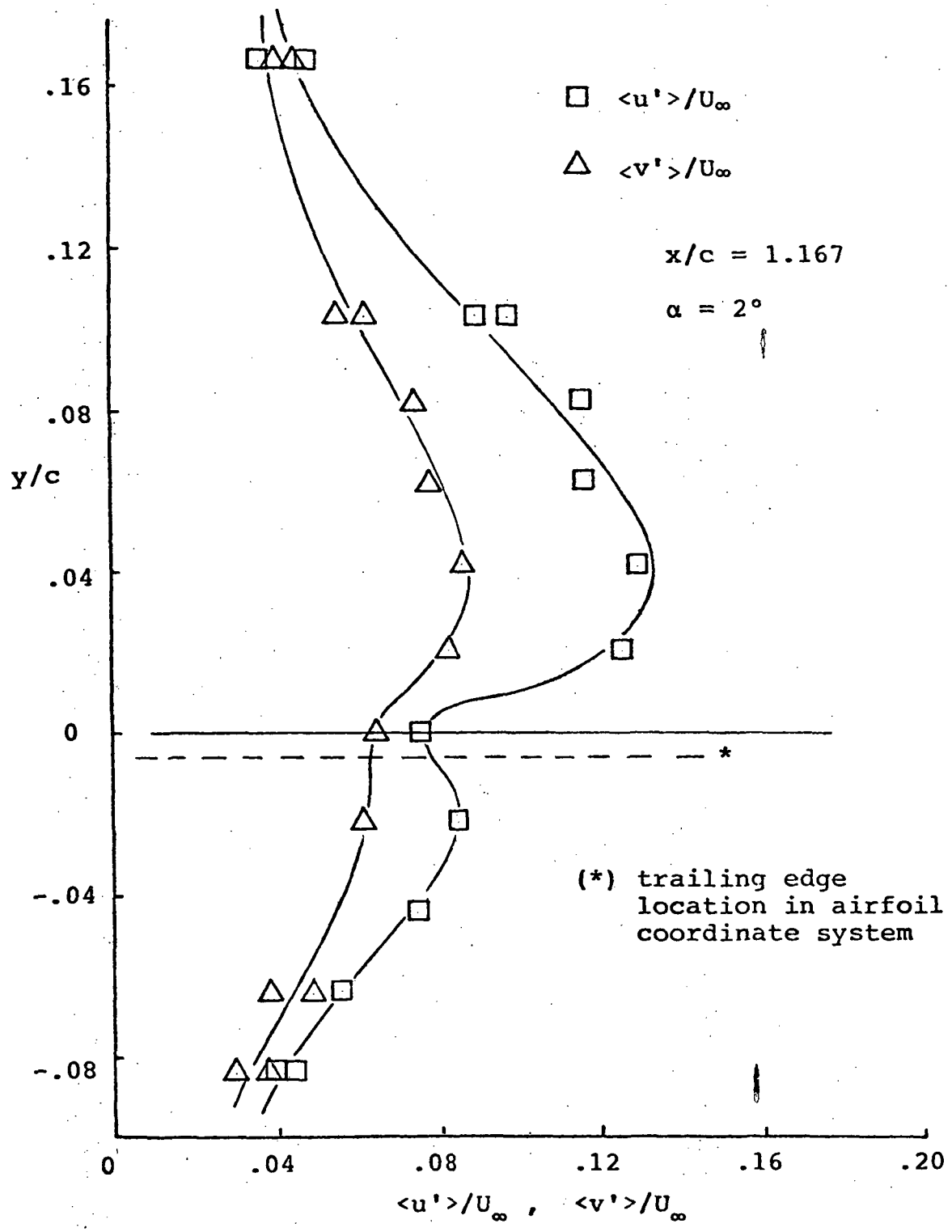

Figure 59. - Turbulent Intensity Distributions; x/c = 1.167; Attack Angle = 2 Degrees

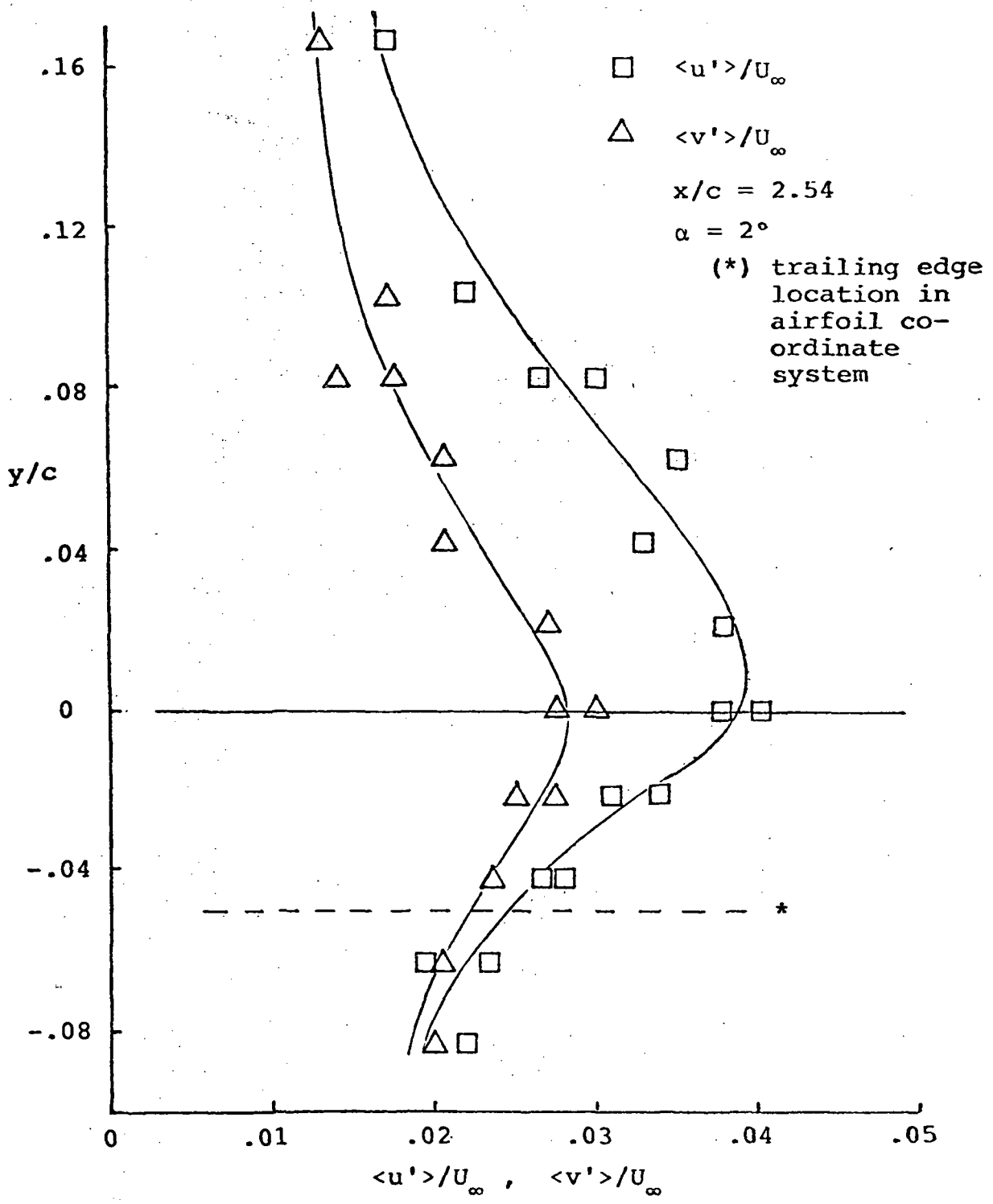

Figure 60. - Turbulent Intensity Distributions; x/c = 2.54; Attack Angle = 2 Degrees

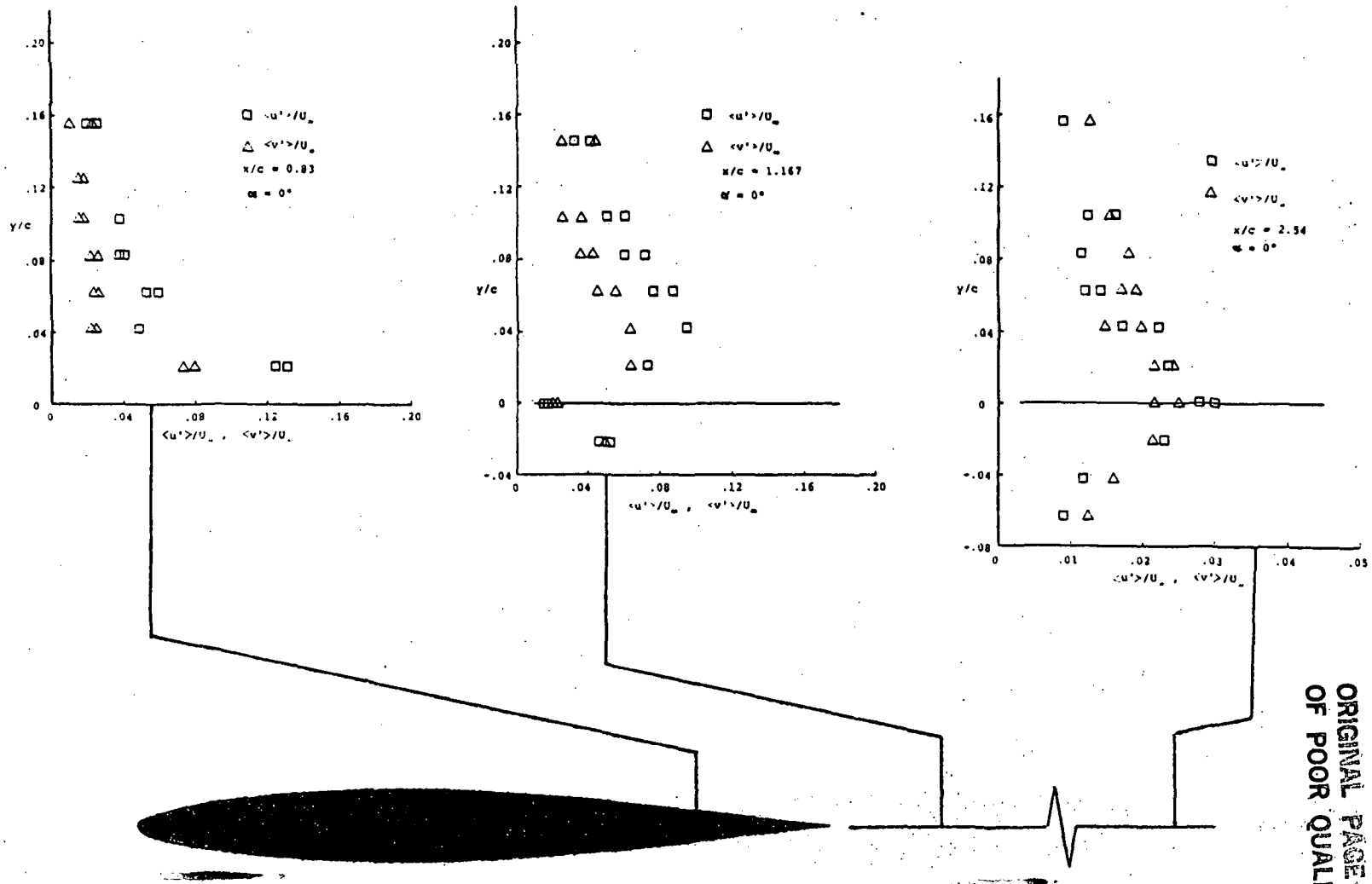

Figure 61. - Development of Turbulent Intensity;
Attack Angle = 0 Degrees

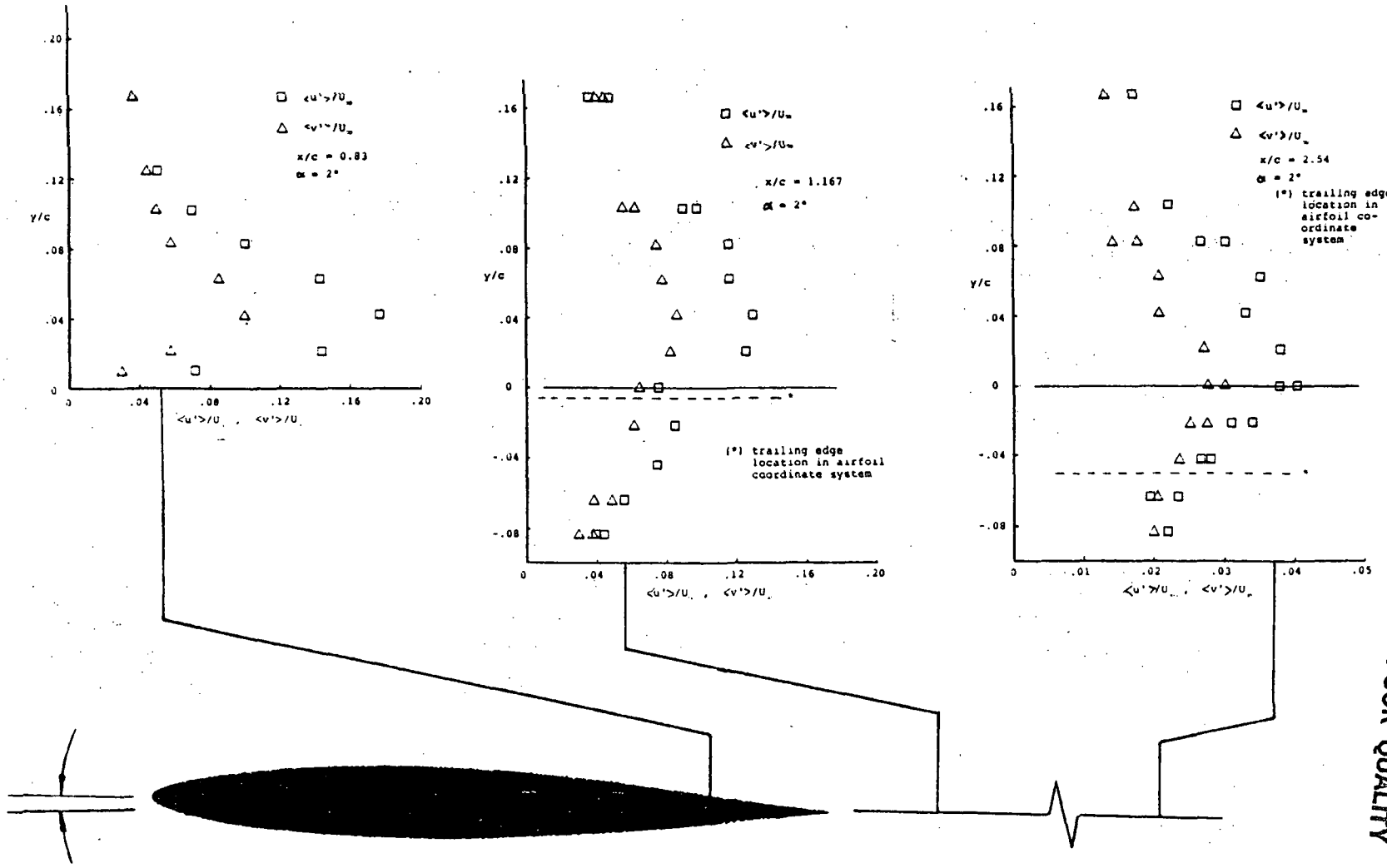

Figure 62. - Development of Turbulent Intensity; Attack Angle = 2 Degrees

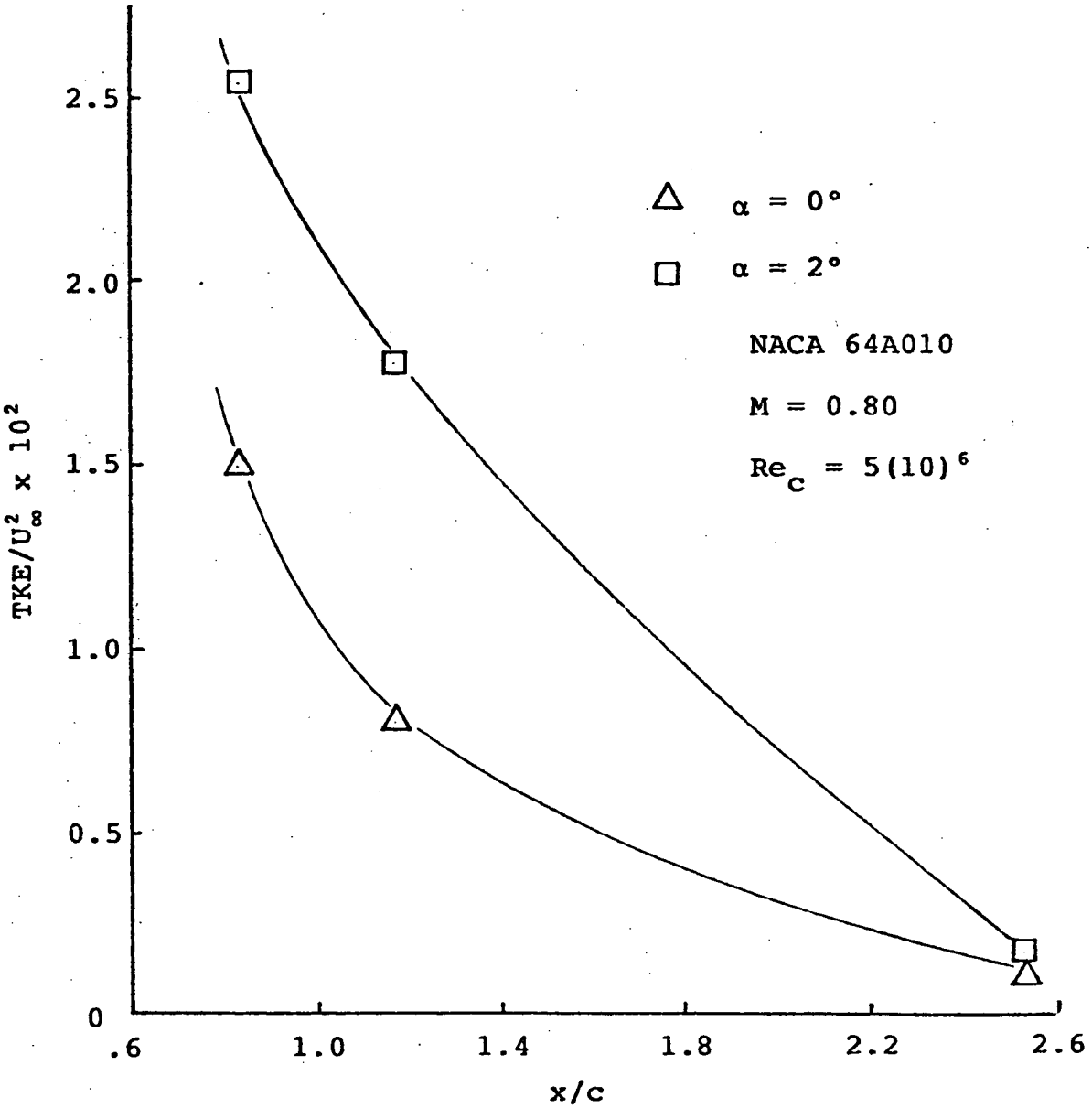

Figure 63 . - Peak Turbulent Kinetic Energy